This is an Accepted manuscript of the article published by Taylor & Francis in Journal of Macromolecular Science, Part A: Pure and Applied Chemistry, 52:9, 659-698, DOI: 10.1080/10601325.2015.1063861

Case Studies with Mathematical Modeling of Free-radical Multi-component Bulk/Solution Polymerizations: Part 1

Woosung Jung, Marzieh Riahinezhad, Thomas A. Duever and Alexander Penlidis*

Institute for Polymer Research (IPR), Department of Chemical Engineering, University of Waterloo, Waterloo, Ontario N2L 3G1, Canada

* Author of correspondence

Abstract

In part 1 of this series of two extensive overviews of multi-component polymerization case studies, we present mathematical modelling results with experimental confirmations. The case studies are from free-radical, bulk and/or solution polymerizations, covering the range from homo- to hexa-polymerization at both regular and elevated temperature levels, i.e., without and with possible depropagation steps. The model eventually tackles complex polymerization features, ranging from conversion-time histories to more esoteric multi-component composition and/or sequence length profiles. Part 2 of the series will describe more complicated situations with depropagation and composition control policies, all relying solely on a unique monomer/polymer database of physico-chemical properties and other characteristics, with no further parameter adjustment. These database items will be cited in tables in part 2 of the series.

Keywords: bulk polymerization, solution polymerization, free-radical polymerization, mathematical modelling, copolymerization, terpolymerization

1 Introduction

In multi-component free-radical polymerization, more than two monomers participate in chain growth leading to 'combined' properties of the individual *homo*-polymers; the polymerization is basically comprised of competitive reactions between different radical/monomer species. As the number of monomer species increases, the number of possible reactions also significantly increases and therefore the polymerization mechanism becomes complicated. Notwithstanding this, both the mathematical modeling and the study of multi-component recipes have attracted considerable industrial and academic interest for several decades due to the added economic benefits of enhanced polymer properties and expanded applications via various combinations of monomers.

This paper starts with an overview on model development and continues with various testing case studies for multi-component polymerizations. There has been a continuous effort in our group for about three decades towards the development, testing and refining of a bulk/solution multi-component polymerization model/database (1-4). It has been shown that the simulation package can act as a very flexible and useful tool that could guide academic and industrial research and development for *homo*-, *co*-, and *ter*-polymerizations.

The objectives of the more recent expansion of the mathematical modeling phase were to extend and test further a mechanistic reactor model for multi-component (up to six monomers) bulk/solution polymerizations under batch/semi-batch reactor configurations with many useful features. A lot of effort was put on searching the literature for physical/kinetic parameters, modeling approaches and experimental data. The six-monomers of interest include styrene (Sty), *n*-butyl acrylate (BA), butyl methacrylate (BMA), hydroxyethyl acrylate (HEA), hydroxybutyl acrylate (HBA), and acrylic acid (AA), along with different permutations. In order to develop a flexible, comprehensive, and user-friendly model, the accompanying model database was also expanded in parallel. This important (and rather unique) database includes physico-chemical/kinetic characteristics/coefficients for the individual monomers and other reaction ingredients,

such as solvents, initiators, and chain transfer agents, and also characteristics of the possible copolymer pairs or terpolymer and (other higher) multicomponent combinations (e.g., values such as reactivity ratios, glass transition temperature characteristics, etc.). These database items (more details on the database items will be cited in part 2 of the series) are fixed and do not change from simulation case to simulation case, thus covering a very wide range of operating conditions, recipes and modes of operation, and hence making the model predictions more credible, thus increasing one's confidence in the model predictive capabilities and future uses for recipe design, reactor operation optimization and anticipation of process modification trends.

Through an extensive literature search for polymerization models and kinetic information, the simulation model was developed into a generalized and comprehensive one which covers the range from *homo*- to *hexa*-polymerization at both regular and elevated temperature levels, in order to explain various polymerization kinetic characteristics (including depropagation and backbiting reaction features), and therefore, to provide quick and reliable predictions of productivity (reaction rate) and quality (molecular weight, polymer composition, sequence length, branching, etc.) of multi-component polymers over a wide range of reaction conditions. Model testing was conducted with experimental data in order to verify the model's reliability. Due to limited experimental data for higher level multi-component polymerizations (with a number of monomers higher than two), the simulation model could be tested with *homo*- up to *tetra*-polymerization cases, which formed the case studies of the paper. The model prediction plots throughout the paper were generated relying solely on a unique database of individual monomers/ingredients and no parameters were adjusted further or selectively in order to obtain agreement with experimental data. In addition, the model was further utilized for investigation of scenarios for control of polymer composition, which is one of the most important factors closely related to mechanical/chemical properties of multi-component polymer products. All these extensive model testing case studies increased the range of the model's applicability as well as the user's confidence in the model's reliability for the description of various polymerization recipes and operating modes.

2 Experimental

2.1 Preamble

This paper contains extensive mathematical modelling results and experimental data. The experimental data come from many sources and they represent a mix of research laboratory and pilot-plant data. As such, actual experimental details can be found under the 'Results and Discussion' section, when different data sources (and their corresponding literature references) and data behaviour are discussed and compared to model predictions. Due to this extensive mathematical modelling, and before we start the discussion of the obtained results, a brief background on multi-component polymerizations along with their mathematical modelling is in order.

2.2 Brief Background on Multi-component Polymerization

2.2.1 Literature Review

Numerous modeling studies and experimental work on *homo*- and multi-component polymerization have taken place over the last 30 years or so, and citing them all here is beyond the scope of this paper. For detailed reviews on multi-component polymerization, see (5). Gao and Penlidis (2) reviewed sources of literature with useful experimental data for several monomer systems in their extensive paper, along with a summary of modeling efforts. They also showed model predictions over a very wide range of monomer systems and conditions, using a comprehensive database of physico-chemical monomer characteristics (WATPOLY). Confirmations and additional extensions were given in (3-4) and (6-7). Using the simulation package, Fujisawa and Penlidis (8) considered modeling work regarding three classes of *co*-polymer composition control strategies in a semi-batch reactor, and discussed the influence of these policies on polymerization rate, composition, molecular weight, branching, etc. Based on the above efforts, the extended version of the multi-component model has been developed including various simulation features and options which will be discussed later in this paper (sequence length distribution, depropagation, and more complex polymerization scenarios).

Depropagation has been known since McCormick (9) discovered experimentally that alpha-methyl styrene (AMS) does not polymerize above 61℃ and verified the relation between thermodynamic equilibrium concentration and ceiling temperature. Lowry (10) assumed three cases in which one of the two monomers undergoes reversible propagation and suggested the corresponding *co*-polymer composition equations. Later on, several efforts to develop a more general equation took place. Wittmer (11), for instance, added some correction factors which compensated for radical effects with different terminal sequence distributions, into the Mayo-Lewis equation (12).

The depropagation model for *co*-polymer composition by Krüger *et al*. (13) was considered more general and stable with better convergence properties than earlier ones, and this was discussed by Palmer *et al*. (14-15) with examples from AMS/methyl methacrylate (MMA) bulk and solution (toluene) batch *co*-polymerizations at 60 to 140℃. They estimated equilibrium constants and *cross*-depropagation ratios as well as reactivity ratios, and obtained experimental data regarding conversion, composition, and molecular weights through the full conversion range. Using these data, Cheong and Penlidis (16) showed reasonable model predictions, and Leamen *et al*. (17-18) reinvestigated this monomer system for more refined parameters and further expanded the studies to AMS/butyl acrylate (BA)/MMA *ter*-polymerization.

All depropagating models mentioned above were based on terminal model kinetics. On the other hand, combinations of depropagating effects with the penultimate model were considered in butyl methacrylate (BMA)/BA *co*-polymerization (19-20), Sty/BMA *co*-polymerization (21), and Sty/dodecyl methacrylate (DMA) *co*-polymerization (22).

Another important aspect included in modeling efforts is intramolecular chain transfer (backbiting), short chain branching, and fragmentation (scission) during BA polymerization. Rantow *et al*. (23) conducted batch reactor modeling with depropagation using the implicit penultimate unit effect model, and good fitting results were obtained by Li *et al*. (20).

2.2.2 Multi-component Polymerization Kinetics

Multi-component radical polymerization follows the regular free-radical polymerization steps: initiation, propagation, termination, chain transfer to small molecules such as monomer, solvent, chain transfer agent (CTA) etc., transfer to polymer, and terminal/internal double bond polymerization. Additional reaction steps at elevated temperatures, such as depropagation and thermal initiation, are also considered when appropriate. BA monomer's secondary reaction steps regarding tertiary radicals related to short chain branching along with other model features and additional case studies are going to be discussed in a later section.

Initiation

$$I \xrightarrow{k_d} 2R_{in}^{\bullet} \tag{1}$$

$$R_{in}^{\bullet} + M_i \xrightarrow{k_{p,0i}} R_{1,i}^{\bullet} \tag{2}$$

The initiation step involves two reactions. First, commercially important azo or peroxide initiators usually yield a pair of primary radicals by thermal homolytic cleavage. Not all primary radicals can participate in further reactions. After initiator decomposition, the radicals are trapped in the reaction mixture due to the cage effect. Within the cage, some radicals may recombine, react with each other or with monomer, or diffuse out to initiate polymerization. Upon exiting, some radicals lose their reactivity and become stable. This is described by the initiator efficiency (usually in the range of 0.3 to 0.75), which is essentially the fraction of radicals that successfully lead to growing chains.

Thermal Initiation

$$nM_i \xrightarrow{k_{th}} mR_{1,i}^{\bullet} + \text{byproducts} \tag{3}$$

Styrenics can undergo initiation without necessarily the presence of an added chemical initiator. This initiation rate is negligible compared to the contribution via chemical initiator decomposition, however, it becomes significant at elevated temperatures (higher than 120℃). This purely (auto)thermal or self-initiation follows a Diels-Alder mechanism (24).

Propagation

$$R^{\bullet}_{r,i} + M_j \xrightarrow{k_{pij}} R^{\bullet}_{r+1,j} \quad (4)$$

Radicals grow by addition of successive monomer species (typically, hundreds or thousands). It should be noted that the higher reactivity a monomer species has, the more it can incorporate into a polymer chain. This is an important feature of multi-component polymerization that allows the synthesis of an almost unlimited number of different products by variations in the nature and relative amounts of the monomer species in the feed.

According to the terminal model based on a first order Markov process, the reactivity of a propagating radical depends only on the monomer unit at the growing radical end and is independent of chain composition. The propagation step is important in a multi-component polymerization because the composition and arrangements eventually encountered in a polymer molecule are mostly dependent on reactivity differences between radical species *i* and monomer species *j*.

Depropagation

$$R^{\bullet}_{r+1,ij} \xrightarrow{\bar{k}_{pij}} R^{\bullet}_{r,i} + M_j \quad (5)$$

At elevated temperatures chains may reversibly undergo depropagation leading to chain length decrease. In the multi-component case, depropagation affects not only the rate of polymerization but also polymer composition, sequence length distribution and molecular weights. There are several models that can be used to predict composition of a reversible *co*-polymer system. Among them, Krüger's probabilistic approach (13, 18), extended to the multi-component case, is more powerful and robust than other models (e.g., Lowry (10) and Wittmer (11)), and will be discussed in more detail later.

Termination

$$R^{\bullet}_{r,i} + R^{\bullet}_{s,j} \xrightarrow{k_{tc}} P_{r+s} \text{ (combination/coupling)} \quad (6)$$

$$R^{\bullet}_{r,i} + R^{\bullet}_{s,j} \xrightarrow{k_{td}} P_r + P_s \text{ (disproportionation)} \quad (7)$$

Chain growth stops and dead polymer molecules are obtained from the reaction of two radicals, either by combination or disproportionation. In termination by combination

(coupling), two radicals make one dead polymer. In disproportionation, a hydrogen atom in the *beta* position of one of the radical centers is transferred to another radical and a terminal double bond is formed.

Chain Transfer to Small Molecules (monomer, solvent and CTA)

$$R_{r,i}^{\bullet} + T \xrightarrow{k_{fmT}} P_r + T^{\bullet} \tag{8}$$

Radical transfer is a chain-breaking reaction. Radical activity can transfer from a growing chain to any existing or added substance, such as monomer, solvent, and chain transfer agent (CTA) following a similar mechanism. This (side) reaction effectively stops the growth of the original radical chain. As a result, a polymer's chain length and hence its molecular weight will be decreased.

Chain Transfer to Impurity (retarder/inhibitor)

$$R_{r,i}^{\bullet} + Z \xrightarrow{k_{fZi}} P_r - Z^{\bullet} \text{ (unreactive)} \tag{9}$$

Impurity can be any compound which not only reduces chain length, but also suppresses the polymerization rate. It converts radicals to unreactive or less reactive species, and the polymerization stops completely (inhibitor) or slows down (retarder) until the impurities are consumed.

Chain Transfer to Polymer (Long Chain Branching, LCB)

$$R_{r,i}^{\bullet} + P_{s,j} \xrightarrow{k_{fpij}} P_{r,i} + R_{s,j}^{\bullet} \tag{10}$$

As conversion increases, transfer to polymer becomes significant. This results in the abstraction of a hydrogen atom from the dead polymer by the growing radical and a new radical site forms somewhere on the polymer backbone instead. Monomer can now add to this 'internal' radical centre, and a branched polymer is produced (tri-functional branching). Transfer to polymer broadens the molecular weight distribution (increase of polydispersity) and increases the weight average molecular weight considerably, but does not influence the number average molecular weight. Unlike other rate constants, measuring the transfer to polymer rate constant is inherently difficult. Because of this, there are relatively few reliable parameter values/sources available in the literature.

Terminal Double Bond Polymerization (LCB)

$$R^{\bullet}_{r,i} + P_{s,j} \xrightarrow{k^{*}_{pij}} R^{\bullet}_{r+s} \tag{11}$$

This is another mechanism for forming long chain branching (LCB). Terminal double bonds on a dead polymer molecule are obtained by either termination via disproportionation or especially transfer to monomer reactions. Once the concentration of these terminal double bonds becomes competitive, a radical can also attack the terminal double bond and one large branched macroradical is created. Eventually, this increases both the number and weight average molecular weights and broadens the molecular weight distribution considerably.

Internal Double Bond Polymerization (Crosslinking)

$$R^{\bullet}_{r,i} + P_{s,j} \xrightarrow{k^{**}_{pij}} R^{\bullet}_{r+s} \tag{12}$$

Crosslinking or network polymer formation is due to the presence of a di-functional monomer, such as 1,3-butadiene, an important monomer widely used in the rubber industry. Addition of a radical to this monomer yields an allylic radical with two possible reasonance structures. This radical reaction proceeds via propagation at either the 1,2 carbon or 1,4 carbon sites. Both dead polymer molecules that may form have an unsaturated (pendant or residual) double bond internally and this will react with another radical to cause crosslinking (or *tetra*-functional long chain branching).

2.2.3 Model Development in a Batch/Semi-batch Reactor

Monomer Balances

If fully reversible, a six-component polymerization involves 36 propagation reactions (6 *homo*-propagations and 30 *cross*-propagations) and 36 depropagation reactions (6 *homo*-depropagations and 30 *cross*-depropagations). Assuming monomer consumption is largely due to propagation steps for producing long chains (Long Chain Approximation or LCA of type I), monomer balances are as follows:

$$\frac{dN_i}{dt} = F_{i,in} - R_{pi}V \tag{13}$$

where N_i, $F_{i,in}$, and R_{pi} stand for the moles, the molar inflow rate, and the rate of consumption of monomer species *i*, respectively, and V is the volume of the reaction mixture. In a batch reactor, $F_{i,in}$ becomes zero. R_{pi} is expressed in terms of rate constants, and radical and monomer concentrations, as shown below, when depropagation is negligible.

$$R_{pi} = \left(k_{p1i}[R_1^\bullet] + k_{p2i}[R_2^\bullet] + \cdots k_{p6i}[R_6^\bullet]\right)[M_i] \tag{14}$$

$$[M] = \sum_{i=1}^{6}[M_i],\ \ [R^\bullet] = \sum_{i=1}^{6}[R_i^\bullet],\ \ \ f_i = \frac{[M_i]}{[M]},\ \ \Phi_j^\bullet = \frac{[R_j^\bullet]}{[R^\bullet]}$$

where [M], $[R^\bullet]$, f_i and $\Phi_j^\bullet$ are the total monomer and radical concentrations, and the mole fraction of monomer species *i* and radical species *j*, respectively.

Radical Balances: No Depropagation

Initiator (N_I) and impurity (N_Z) balances are needed to build the full radical balance. Radicals are generally generated by initiator decomposition and consumed in termination or in reactions with impurities.

$$\frac{dN_I}{dt} = F_{I,in} - k_d N_I \tag{15}$$

$$\frac{dN_Z}{dt} = F_{Z,in} - k_{fz} N_Z [R^\bullet] \tag{16}$$

where k_d and k_{fz} are the initiator decomposition rate constant and impurity reaction rate constant, respectively. The total radical concentration is calculated using the following balance:

$$\frac{d\left(V[R^\bullet]\right)}{dt} = R_I - k_{fz} N_Z [R^\bullet] - k_t [R^\bullet]^2 V \tag{17}$$

where k_t is the overall termination rate constant ($k_t = k_{tc} + k_{td}$), and R_I, the initiation rate, will be defined later in Equation 50. Using the steady state hypothesis (SSH) for radicals, based on Equation 17, the total radical concentration is calculated as:

$$[R^\bullet] = \frac{1}{2}\left\{\left[\left(\frac{k_{fz}(N_z/V)}{k_t}\right)^2 + 4\frac{(R_I/V)}{k_t}\right]^{1/2} - \frac{k_{fz}(N_z/V)}{k_t}\right\} \tag{18}$$

Multiplying this with the corresponding radical fractions $\Phi_j^\bullet$ gives the individual radical concentrations. In order to calculate $\Phi_j^\bullet$, radical balances are formulated by assuming that *cross*-propagation rates of two radicals are equal and therefore, SSH of radicals in multi-component polymerization is also valid (Long Chain Approximation or LCA of type II). In a six-component case, for example, 30 *cross*-propagation reaction constants should be considered.

$$\begin{aligned}\frac{d[R_i^\bullet]}{dt} &= \sum_{\substack{j=1\\(j\neq i)}}^{6} R_{ji} - \sum_{\substack{j=1\\(j\neq i)}}^{6} R_{ij} \\ &= \left(k_{p1i}[R_1^\bullet] + k_{p2i}[R_2^\bullet] + \cdots + k_{p6i}[R_6^\bullet]\right)[M_i] \\ &\quad - \left(k_{pi1}[M_1] + k_{pi2}[M_2] + \cdots + k_{pi6}[M_6]\right)[R_i^\bullet] \approx 0\end{aligned} \tag{19}$$

where R_{ij} is the reaction rate of a radical (ending in monomer *i*) with monomer *j*.

Radical fractions can now be solved from a generalized system (set) of equations. Rearranging into a matrix form, Equation 19 can be expressed as

$$\mathbf{M} \cdot \mathbf{r} = \mathbf{b} \tag{20}$$

where

$$\mathbf{M} = \begin{bmatrix} -\sum_{j=2}^{6}\left(k_{p1j} f_j\right) & k_{p21} f_1 & k_{p31} f_1 & k_{p41} f_1 & k_{p51} f_1 & k_{p61} f_1 \\ k_{p12} f_2 & -\sum_{\substack{j=1\\(j\neq 2)}}^{6}\left(k_{p2j} f_j\right) & k_{p32} f_2 & k_{p42} f_2 & k_{p52} f_2 & k_{p62} f_2 \\ k_{p13} f_3 & k_{p23} f_3 & -\sum_{\substack{j=1\\(j\neq 3)}}^{6}\left(k_{p3j} f_j\right) & k_{p43} f_3 & k_{p53} f_3 & k_{p63} f_3 \\ k_{p14} f_4 & k_{p24} f_4 & k_{p34} f_4 & -\sum_{\substack{j=1\\(j\neq 4)}}^{6}\left(k_{p4j} f_j\right) & k_{p54} f_4 & k_{p64} f_4 \\ k_{p15} f_5 & k_{p25} f_5 & k_{p35} f_5 & k_{p45} f_5 & -\sum_{\substack{j=1\\(j\neq 5)}}^{6}\left(k_{p5j} f_j\right) & k_{p65} f_5 \\ k_{p16} f_6 & k_{p26} f_6 & k_{p36} f_6 & k_{p46} f_6 & k_{p56} f_6 & -\sum_{j=1}^{5}\left(k_{p6j} f_j\right) \end{bmatrix}$$

$$\mathbf{r} = \left[\Phi_1^\bullet \quad \Phi_2^\bullet \quad \Phi_3^\bullet \quad \Phi_4^\bullet \quad \Phi_5^\bullet \quad \Phi_6^\bullet\right]', \quad \mathbf{b} = \left[0 \quad 0 \quad 0 \quad 0 \quad 0 \quad 0\right]'$$

Since $\sum_{i=1}^{6} \Phi_i^\bullet = 1$, substituting $\Phi_6^\bullet = 1 - \Phi_1^\bullet - \Phi_2^\bullet - \Phi_3^\bullet - \Phi_4^\bullet - \Phi_5^\bullet$ and rearranging again, the following expression is obtained:

$$\mathbf{M} = \begin{bmatrix} -\sum_{j=2}^{6}\left(k_{p1j}f_j\right)-k_{p61}f_1 & \left(k_{p21}-k_{p61}\right)f_1 & \left(k_{p31}-k_{p61}\right)f_1 & \left(k_{p41}-k_{p61}\right)f_1 & \left(k_{p51}-k_{p61}\right)f_1 \\ \left(k_{p12}-k_{p62}\right)f_2 & -\sum_{\substack{j=1\\(j\neq 2)}}^{6}\left(k_{p2j}f_j\right)-k_{p62}f_2 & \left(k_{p32}-k_{p62}\right)f_2 & \left(k_{p42}-k_{p62}\right)f_2 & \left(k_{p52}-k_{p62}\right)f_2 \\ \left(k_{p13}-k_{p63}\right)f_3 & \left(k_{p23}-k_{p63}\right)f_3 & -\sum_{\substack{j=1\\(j\neq 3)}}^{6}\left(k_{p3j}f_j\right)-k_{p63}f_3 & \left(k_{p43}-k_{p63}\right)f_3 & \left(k_{p53}-k_{p63}\right)f_3 \\ \left(k_{p14}-k_{p64}\right)f_4 & \left(k_{p24}-k_{p64}\right)f_4 & \left(k_{p34}-k_{p64}\right)f_4 & -\sum_{\substack{j=1\\(j\neq 4)}}^{6}\left(k_{p4j}f_j\right)-k_{p64}f_4 & \left(k_{p54}-k_{p64}\right)f_4 \\ \left(k_{p15}-k_{p65}\right)f_5 & \left(k_{p25}-k_{p65}\right)f_5 & \left(k_{p35}-k_{p65}\right)f_5 & \left(k_{p45}-k_{p65}\right)f_5 & -\sum_{\substack{j=1\\(j\neq 5)}}^{6}\left(k_{p5j}f_j\right)-k_{p65}f_5 \end{bmatrix}$$

$$\mathbf{r} = \left[\Phi_1^{\bullet} \quad \Phi_2^{\bullet} \quad \Phi_3^{\bullet} \quad \Phi_4^{\bullet} \quad \Phi_5^{\bullet}\right]', \ \mathbf{b} = \left[-k_{p61}f_1 \quad -k_{p62}f_2 \quad -k_{p63}f_3 \quad -k_{p64}f_4 \quad -k_{p65}f_5\right]'$$

Finally, radical fractions are calculated by $\mathbf{r} = \mathbf{M}^{-1} \cdot \mathbf{b}$; individual radical concentrations can be obtained by multiplying the total radical concentration in Equation 18 by each radical fraction.

Radical Balances: Depropagation

In the depropagation case, radical concentration calculations become more complicated. There are 72 reactions in total including 36 propagations and 36 depropagations which need to be considered for a six-monomer system.

$$\begin{array}{lll} R_1^{\bullet} + M_1 \underset{\bar{k}_{11}}{\overset{k_{11}}{\longleftrightarrow}} R_{11}^{\bullet} & R_2^{\bullet} + M_1 \underset{\bar{k}_{21}}{\overset{k_{21}}{\longleftrightarrow}} R_{21}^{\bullet} & \cdots \quad R_6^{\bullet} + M_1 \underset{\bar{k}_{61}}{\overset{k_{61}}{\longleftrightarrow}} R_{61}^{\bullet} \\ R_1^{\bullet} + M_2 \underset{\bar{k}_{12}}{\overset{k_{12}}{\longleftrightarrow}} R_{12}^{\bullet} & R_2^{\bullet} + M_2 \underset{\bar{k}_{22}}{\overset{k_{22}}{\longleftrightarrow}} R_{22}^{\bullet} & \cdots \quad R_6^{\bullet} + M_2 \underset{\bar{k}_{62}}{\overset{k_{62}}{\longleftrightarrow}} R_{62}^{\bullet} \\ \vdots & \vdots & \vdots \\ R_1^{\bullet} + M_6 \underset{\bar{k}_{16}}{\overset{k_{16}}{\longleftrightarrow}} R_{16}^{\bullet} & R_2^{\bullet} + M_6 \underset{\bar{k}_{26}}{\overset{k_{26}}{\longleftrightarrow}} R_{26}^{\bullet} & \cdots \quad R_6^{\bullet} + M_6 \underset{\bar{k}_{66}}{\overset{k_{66}}{\longleftrightarrow}} R_{66}^{\bullet} \end{array} \tag{21}$$

Therefore, Equations 14 and 19 should be modified to include *homo*- and *cross*-depropagation terms using the extended Krüger's six-component model.

$$R_{pj} = \sum_{i=1}^{6} k_{pij}[R_i^{\bullet}][M_j] - \sum_{i=1}^{6} \bar{k}_{pij}[R_{ij}^{\bullet}] \tag{22}$$

$$\frac{d[R_j^{\bullet}]}{dt} = \sum_{\substack{i=1\\(i\neq j)}}^{6}\left(k_{pij}[R_i^{\bullet}][M_j] + \bar{k}_{pji}[R_{ji}^{\bullet}]\right) - \sum_{\substack{i=1\\(i\neq j)}}^{6}\left(k_{pji}[R_j^{\bullet}][M_i] + \bar{k}_{pij}[R_{ij}^{\bullet}]\right) \tag{23}$$

Krüger (13) calculated the penultimate radical concentration $[R_{ij}^{\bullet}]$ using the probability that a monomer of type *j* is attached to a (penultimate) radical ending in *i*, P_{ij}.

$$[R_j^{\bullet}] = \sum_{i=1}^{6} [R_{ij}^{\bullet}], \quad P_{ij} = \frac{[R_{ij}^{\bullet}]}{[R_j^{\bullet}]} \tag{24}$$

where $\sum_{i=1}^{6} P_{ij} = 1$

Equations 22 and 23 can be rewritten using Equation 24 as follows:

$$R_{pj} = \sum_{i=1}^{6} k_{pij} [R_i^{\bullet}][M_j] - \sum_{i=1}^{6} \overline{\overline{k}}_{pij} P_{ij} [R_j^{\bullet}] \tag{25}$$

$$\frac{d[R_j^{\bullet}]}{dt} = \sum_{\substack{i=1 \\ (i \neq j)}}^{6} \left(k_{pij} [R_i^{\bullet}][M_j] + \overline{\overline{k}}_{pji} P_{ji} [R_i^{\bullet}] \right) - \sum_{\substack{i=1 \\ (i \neq j)}}^{6} \left(k_{pji} [R_j^{\bullet}][M_i] + \overline{\overline{k}}_{pij} P_{ij} [R_j^{\bullet}] \right) \tag{26}$$

Assuming SSH, the left side of Equation 26 becomes zero. On the other hand, the probability P_{ij} in Equation 24 is expressed in terms of rate constants and species concentrations.

$$P_{ij} = \frac{k_{pij} [R_i^{\bullet}][M_j] - \overline{\overline{k}}_{pij} [R_{ij}^{\bullet}]}{\sum_{l=1}^{6} k_{plj} [R_l^{\bullet}][M_j] - \sum_{l=1}^{6} \overline{\overline{k}}_{plj} [R_{lj}^{\bullet}]} = \frac{k_{pij} [R_i^{\bullet}][M_j] - \overline{\overline{k}}_{pij} P_{ij} [R_j^{\bullet}]}{\sum_{l=1}^{6} k_{plj} [R_l^{\bullet}][M_j] - \sum_{l=1}^{6} \overline{\overline{k}}_{plj} P_{lj} [R_j^{\bullet}]} \tag{27}$$

Equation 27 introduces nonlinearities and hence, Equations 26 and 27 should be solved simultaneously by a numerical method.

In our example of *hexa*-polymerization, there are 36 probabilities and 6 radical fractions that need to be calculated. Therefore, the required number of (nonlinear) Equations 26 and 27 becomes 42 and they can be solved by an appropriate numerical method (e.g., either Newton's or trust region technique).

Other Important Balances

If a chain transfer agent (N_{CTA}) and/or solvent (N_S) are present in the reactor, they will decrease molecular weight and the following balances should also be included:

$$\frac{dN_{CTA}}{dt} = F_{CTA,in} - k_{fCTA} N_{CTA} [R^{\bullet}] \tag{28}$$

$$\frac{dN_S}{dt} = F_{S,in} - k_{fS} N_S [R^\bullet] \tag{29}$$

where k_{fCTA} and k_{fS} represent chain transfer rate constants to CTA and solvent, respectively.

Due to the change in density from monomer to polymer, the volume of the polymerizing mixture will shrink during the reaction according to the following expression:

$$\frac{dV}{dt} = \sum_{i=1}^{6} \left[\frac{F_{i,in} Mw_i}{\rho_{i,monomer}} - R_{pi} Mw_i \left(\frac{1}{\rho_{i,monomer}} - \frac{1}{\rho_{polymer}} \right) V \right] \tag{30}$$

where Mw_i, $\rho_{i,monomer}$, and $\rho_{polymer}$ are the molecular weight and the density of monomer species *i*, and the density of polymer, respectively.

Another important balance is necessary for the moles of each monomer in the reactor which are bound as polymer. In a batch reactor, where there is no inflow/outflow of polymer from the reactor, the amount of consumed monomers is equal to that of the generated polymer according to LCA I, and conversion/polymer composition calculations can be obtained directly from the monomer balances in Equation 13. However, in a semi-batch reactor, additional balances are needed for the inflow of monomers that are incorporated in the multi-component polymer in order to calculate conversion/polymer composition profiles properly:

$$\frac{dP_i}{dt} = F_{pi,in} + R_{pi} V \tag{31}$$

where P_i and $F_{pi,in}$ are the moles and molar inflow of monomer species *i* bound as polymer.

Conversion, Composition, Sequence Length Indicators and Triad Fractions

The total molar conversion of monomers to multi-component polymer is given by

$$X = \frac{[M]_0 - [M]}{[M]_0} = \frac{\sum_{i=1}^{6} P_i}{\sum_{i=1}^{6} (N_i + P_i)} \tag{32}$$

Similarly, partial conversion of monomer species *i* is

$$X_i = \frac{P_i}{N_i + P_i} \tag{33}$$

Conversion versus time profiles indicate how fast polymerization proceeds (polymer productivity).

The instantaneous polymer composition, the overall mole fraction of monomer *i* incorporated instantaneously in the polymer, is calculated as

$$F_i = \frac{dN_i}{\sum_{i=1}^{6}(dN_i)} = \frac{R_{pi}}{R_p} = \frac{R_{pi}}{\sum_{i=1}^{6} R_{pi}} \tag{34}$$

Equation 34 covers all kinds of multi-component cases (and reduces to *homo*-polymerization). When reduced to simpler cases without depropagation, it becomes identical with the Mayo-Lewis (co-polymer) equation (12), Alfrey-Goldfinger (*ter*-polymer) model (25), and Walling-Briggs (*ter*- and higher) equations (26). Comparing these instantaneous polymer compositions with the ones from Valvassori-Sartori (27) and Hocking-Klimchuck (28) composition equations, which are derived from a simplified LCA II, the differences are not significantly large relative to typically encountered experimental errors (5).

The accumulated polymer composition, the average mole fraction of monomer *i* incorporated into the polymer at a certain conversion level, is determined by

$$\overline{F_i} = \frac{P_i}{\sum_{i=1}^{6} P_i} \tag{35}$$

Co-polymer composition in a batch reactor usually exhibits the so-called ‘composition drift’. Polymer composition is an important indicator closely related to the polymer’s mechanical, chemical and optical properties. Therefore, it should be controlled to produce a desired product. Polymer composition control will be discussed later in section 3.16 as a case study.

Estimation of reactivity ratios is key to calculating polymer composition as well as radical fractions mentioned earlier. The definition of a reactivity ratio under the terminal model is the ratio of a *homo*-propagation rate constant divided by a *cross*-propagation rate constant.

$$r_{ij} = \frac{k_{pii}}{k_{pij}} \quad (i \neq j) \tag{36}$$

A six-component system basically requires 30 binary reactivity ratios for *cross*-propagations and 6 individual *homo*-propagation rate constants. Furthermore, the number of parameters will be more than that considering depropagation. Therefore, successful multi-component studies rely on the establishment of good *homo*- and *co*-polymerization kinetic data.

Multi-component polymer compositions obtained in Equations 34 and 35 are able to describe the overall macroscopic instantaneous/accumulated mole ratio of monomer units in the polymer chain. However, they cannot give a whole picture regarding the distribution of monomer sequences, for example, in block *co*-polymers such as -AA--A-BB--B-AA-, and purely alternating *co*-polymers such as -A-B-A-B-A-B-, having the same composition. This microstructural property, i.e., information about the average number of monomer units coming from how they are distributed along the polymer chain, can be revealed by the sequence length distribution. Because of reflecting intramolecular homo(hetero)geneity, average sequence length and sequence length distribution (SLD) can be important indicators of multi-component polymer quality/behaviour, especially when the individual *homo*-polymers have widely differing properties.

To illustrate this, a statistical approach (Koenig (29)) was followed. Assuming the polymerization behaviour follows the terminal model with full depropagation, the probability p_{ij}, that a growing radical with unit i in its end adds monomer j, in a six-monomer system is defined as:

$$p_{ij} = \frac{k_{pij}[R_i^\bullet][M_j] - \overline{\overline{k}}_{pij}[R_{ij}^\bullet]}{\sum_{l=1}^{6} k_{pil}[R_i^\bullet][M_l] - \sum_{l=1}^{6} \overline{\overline{k}}_{pil}[R_{il}^\bullet]} = \frac{k_{pij}[R_i^\bullet][M_j] - \overline{\overline{k}}_{pij} P_{ij}[R_j^\bullet]}{\sum_{l=1}^{6} k_{pil}[R_i^\bullet][M_l] - \sum_{l=1}^{6} \overline{\overline{k}}_{pil} P_{il}[R_l^\bullet]} \tag{37}$$

where

$$\sum_{j=1}^{6} p_{ij} = p_{ii} + \sum_{k=1}^{6} p_{ik} = 1 \quad (k \neq i)$$

The probability p_{ij} is totally different from (and not to be confused with) P_{ij} (capital letter) for depropagation in Equation 27, despite their algebraic similarity. Using p_{ij}, the probability distribution of having n consecutive units of monomer i, that is, a sequence of monomer i with length n in a growing chain, is:

$$N_{in} = p_{ii}^{n-1} \sum_{k=1}^{6} p_{ik} \quad (k \neq i) \tag{38}$$

where

$$\sum_{n=1}^{\infty} N_{in} = \sum_{k=1}^{6} p_{ik} \left(\sum_{n=1}^{\infty} p_{ii}^{n-1} \right) \approx \sum_{k=1}^{6} p_{ik} \frac{1}{1-p_{ii}} = \frac{1-p_{ii}}{1-p_{ii}} = 1 \quad (k \neq i)$$

The instantaneous number and weight average sequence lengths of monomer i in *hexa*-polymerization are calculated in Equations 39 and 40, respectively.

$$\begin{aligned} \overline{\overline{n}}_i &= \frac{\sum_{n=1}^{\infty} nN_{in}}{\sum_{n=1}^{\infty} N_{in}} = \sum_{n=1}^{\infty} nN_{in} = N_{i1} + 2N_{i2} + 3N_{i3} + \cdots = \sum_{n=1}^{\infty} \left(np_{ii}^{n-1} \sum_{k=1}^{6} p_{ik} \right) = \sum_{n=1}^{\infty} \left\{ np_{ii}^{n-1} (1-p_{ii}) \right\} \\ &= \sum_{n=1}^{\infty} np_{ii}^{n-1} - \sum_{n=1}^{\infty} np_{ii}^{n} \approx \frac{1}{(1-p_{ii})^2} - \frac{p_{ii}}{(1-p_{ii})^2} = \frac{1}{1-p_{ii}} = \frac{1}{\sum_{k=1}^{6} p_{ik}} \end{aligned} \tag{39}$$

$$\begin{aligned} \overline{\overline{w}}_i &= \frac{\sum_{n=1}^{\infty} n^2 N_{in}}{\sum_{n=1}^{\infty} nN_{in}} = \frac{\sum_{n=1}^{\infty} n^2 N_{in}}{\overline{\overline{n}}_i} = \sum_{k=1}^{6} p_{ik} \sum_{n=1}^{\infty} n^2 N_{in} = \sum_{k=1}^{6} p_{ik} \sum_{n=1}^{\infty} n^2 \left(p_{ii}^{n-1} \sum_{k=1}^{6} p_{ik} \right) = \left(\sum_{k=1}^{6} p_{ik} \right)^2 \sum_{n=1}^{\infty} n^2 p_{ii}^{n-1} \\ &= (1-p_{ii})^2 \sum_{n=1}^{\infty} n^2 p_{ii}^{n-1} \approx (1-p_{ii})^2 \frac{1+p_{ii}}{(1-p_{ii})^3} = \frac{1+p_{ii}}{1-p_{ii}} \end{aligned} \tag{40}$$

In order to determine the cumulative probability distribution as a weighted composite of the instantaneous values, these instantaneous values should be integrated. The governing equations are expressed as follows, based on approaches described in (30-31):

$$\overline{\overline{N_{in}}} = \frac{\int_0^{X_i} \left(\frac{N_{in}}{\overline{n_i}} \right) dX_i}{\int_0^{X_i} \frac{dX_i}{\overline{n_i}}} = \frac{\int_0^{X} \left(\frac{N_{in}}{\overline{n_i}} \right) F_i dX}{\int_0^{X} \frac{F_i dX}{\overline{n_i}}} = \frac{\int_0^{X} \left\{ p_{ii}^{n-1} \left(\sum_{k=1}^{6} p_{ik} \right)^2 \right\} F_i dX}{\int_0^{X} \left(\sum_{k=1}^{6} p_{ik} \right) F_i dX} = \frac{\int_0^{X} \left\{ p_{ii}^{n-1} (1-p_{ii})^2 \right\} F_i dX}{\int_0^{X} (1-p_{ii}) F_i dX} \tag{41}$$

where

$$\sum_{n=1}^{\infty} \overline{\overline{N_{in}}} = \frac{\int_0^{X} \left(\sum_{n=1}^{\infty} p_{ii}^{n-1} \right) (1-p_{ii})^2 F_i dX}{\int_0^{X} (1-p_{ii}) F_i dX} = \frac{\int_0^{X} \frac{1}{(1-p_{ii})} (1-p_{ii})^2 F_i dX}{\int_0^{X} (1-p_{ii}) F_i dX} = \frac{\int_0^{X} (1-p_{ii}) F_i dX}{\int_0^{X} (1-p_{ii}) F_i dX} = 1 \tag{42}$$

The cumulative number-average sequence length of monomer *i* is calculated as

$$\overline{\overline{N_i}} = \frac{\sum_{n=1}^{\infty} n \overline{\overline{N_{in}}}}{\sum_{n=1}^{\infty} \overline{\overline{N_{in}}}} = \frac{\int_0^{X} \left(\sum_{n=1}^{\infty} n p_{ii}^{n-1} \right) (1-p_{ii})^2 F_i dX}{\int_0^{X} (1-p_{ii}) F_i dX} \approx \frac{\int_0^{X} \frac{1}{(1-p_{ii})^2} (1-p_{ii})^2 F_i dX}{\int_0^{X} (1-p_{ii}) F_i dX} = \frac{\int_0^{X} F_i dX}{\int_0^{X} (1-p_{ii}) F_i dX} \tag{43}$$

whereas the cumulative weight-average sequence length of monomer *i* is given by

$$\begin{aligned} \overline{\overline{W_i}} &= \frac{\sum_{n=1}^{\infty} n^2 \overline{\overline{N_{in}}}}{\sum_{n=1}^{\infty} n \overline{\overline{N_{in}}}} = \frac{\sum_{n=1}^{\infty} n^2 \overline{\overline{N_{in}}}}{\overline{\overline{N_i}}} = \frac{\int_0^{X} \left(\sum_{n=1}^{\infty} n^2 p_{ii}^{n-1} \right) (1-p_{ii})^2 F_i dX}{\overline{\overline{N_i}} \int_0^{X} (1-p_{ii}) F_i dX} \\ &\approx \frac{\int_0^{X} \frac{1+p_{ii}}{(1-p_{ii})^3} (1-p_{ii})^2 F_i dX}{\overline{\overline{N_i}} \int_0^{X} (1-p_{ii}) F_i dX} = \frac{\int_0^{X} \frac{1+p_{ii}}{1-p_{ii}} F_i dX \Big/ \int_0^{X} (1-p_{ii}) F_i dX}{\int_0^{X} F_i dX \Big/ \int_0^{X} (1-p_{ii}) F_i dX} = \frac{\int_0^{X} \frac{1+p_{ii}}{1-p_{ii}} F_i dX}{\int_0^{X} F_i dX} \end{aligned} \tag{44}$$

Another way to investigate polymer microstructure is the calculation of dyad, triad, or pentad fractions. Among them, triad fraction calculations, being more frequently used, have again been extended herein to six-component polymerizations as an example. The triad fractions are described by the probability functions p_{ij} of Equation 37. Generally, there are three patterns of triad fractions, given in Equations 45 to 47.

$$A_{iii} = p_{ii}^2 = \left(\frac{r_{ij} f_i}{f_j + r_{ij} f_i} \right)^2 \tag{45}$$

$$A_{jij} = p_{ij}^2 = \left(\frac{f_j}{f_j + r_{ij} f_i} \right)^2 \neq p_{ji} p_{ij} \tag{46}$$

$$A_{iij} = A_{jii} = p_{ii} p_{ij} = p_{ii}(1 - p_{ii}) = \frac{r_{ij} f_i f_j}{(f_j + r_{ij} f_i)^2} \tag{47}$$

where $i, j = \{1, 2, 3, 4, 5, 6\}$ (there are 126 distinguishable cases out of total 216 triads). Considering all distinguishable monomer 1-centred triad fractions, their summation should equal 1, as shown in the sample calculation that follows:

$$\begin{aligned}
\sum_{j=1}^{6}\sum_{k=1}^{6} A_{j1k} &= (A_{111} + A_{112} + A_{113} + A_{114} + A_{115} + A_{116}) + (A_{211} + A_{212} + A_{213} + A_{214} + A_{215} + A_{216}) \\
&+ (A_{311} + A_{312} + A_{313} + A_{314} + A_{315} + A_{316}) + (A_{411} + A_{412} + A_{413} + A_{414} + A_{415} + A_{416}) \\
&+ (A_{511} + A_{512} + A_{513} + A_{514} + A_{515} + A_{516}) + (A_{611} + A_{612} + A_{613} + A_{614} + A_{615} + A_{616}) \\
&= (A_{111} + A_{112} + A_{113} + A_{114} + A_{115} + A_{116}) + (A_{112} + A_{212} + A_{213} + A_{214} + A_{215} + A_{216}) \\
&+ (A_{113} + A_{213} + A_{313} + A_{314} + A_{315} + A_{316}) + (A_{114} + A_{214} + A_{314} + A_{414} + A_{415} + A_{416}) \\
&+ (A_{115} + A_{215} + A_{315} + A_{415} + A_{515} + A_{516}) + (A_{116} + A_{216} + A_{316} + A_{416} + A_{516} + A_{616}) \\
&= (A_{111} + A_{212} + A_{313} + A_{414} + A_{515} + A_{616}) + 2(A_{112} + A_{113} + A_{114} + A_{115} + A_{116}) \\
&+ 2(A_{213} + A_{214} + A_{215} + A_{216}) + 2(A_{314} + A_{315} + A_{316}) \\
&+ 2(A_{415} + A_{416}) + 2A_{516} \\
&= p_{11}^2 + p_{12}^2 + p_{13}^2 + p_{14}^2 + p_{15}^2 + p_{16}^2 \\
&+ 2p_{11}p_{12} + 2p_{11}p_{13} + 2p_{11}p_{14} + 2p_{11}p_{15} + 2p_{11}p_{16} \\
&+ 2p_{12}p_{13} + 2p_{12}p_{14} + 2p_{12}p_{15} + 2p_{12}p_{16} \\
&+ 2p_{13}p_{14} + 2p_{13}p_{15} + 2p_{13}p_{16} \\
&+ 2p_{14}p_{15} + 2p_{14}p_{16} \\
&+ 2p_{15}p_{16} \\
&= (p_{11} + p_{12} + p_{13} + p_{14} + p_{15} + p_{16})^2 = 1^2 = 1
\end{aligned} \tag{48}$$

Accumulated triad fractions are obtained by the usual integration of the corresponding instantaneous properties over conversion, such as:

$$\overline{\overline{A_{jik}}} = \frac{\int_0^X (A_{jik} F_i) dX}{\int_0^X F_i dX} \tag{49}$$

Pseudo-rate Constant Method

The pseudo-rate constant method enables a complicated multi-component polymerization system to be viewed as a virtual "*homo*-polymerization". The monomer and radical fractions obtained above are used in the pseudo-rate constant calculations for the multi-component case. Individual rate constants are properly weighed into the overall pseudo-rate constant, depending on the specific reaction step.

The rate of initiation in multi-component polymerization can be written in the same way as for *homo*-polymerization:

$$R_I = 2\sum_{i=1}^{l} f_i k_{di}[I]_i \tag{50}$$

where l denotes the number of possible initiators used in the recipe; each initiator has its own decomposition rate constant, efficiency factor and concentration, k_{di}, f_i and $[I]_i$, respectively.

The rate of multi-component polymerization is the rate of disappearance of monomer species in the system.

$$R_p = -\frac{d\left(\sum_{i=1}^{6}[M_i]\right)}{dt} = \sum_{i=1}^{6}\sum_{j=1}^{6}\left(k_{pij}[R_i^\bullet][M_j] - \overline{\overline{k}}_{pij}P_{ij}[R_j^\bullet]\right) = k_{p,pseudo}[M][R^\bullet] \tag{51}$$

The pseudo-propagation rate constant can be expressed as

$$k_{p,pseudo} = \sum_{i=1}^{6}\sum_{j=1}^{6}\left(k_{pij}\Phi_i^\bullet f_j - \frac{\overline{\overline{k}}_{pij}P_{ij}\Phi_i^\bullet}{[M]}\right) \tag{52}$$

The rate of termination is given by

$$R_t = k_{t,pseudo}[R^\bullet]^2 = \sum_{i=1}^{6}\sum_{j=1}^{6}k_{tij}[R_i^\bullet][R_j^\bullet] = \sum_{i=1}^{6}k_{tii}[R_i^\bullet]^2 + \sum_{i=1}^{6}\sum_{\substack{j=2\\(i\neq j)}}^{6}2k_{tij}[R_i^\bullet][R_j^\bullet] \tag{53}$$

where, when $i = j$, k_{tij} becomes the *homo*-termination rate constant, whereas when $i \neq j$, k_{tij} is the *cross*-termination rate constant ($k_{tij} = k_{tji}$).

The pseudo-termination rate constant is

$$k_{t,pseudo} = \sum_{i=1}^{6}\sum_{j=1}^{6} k_{tij}\Phi_i^{\bullet}\Phi_j^{\bullet} \tag{54}$$

The pseudo-rate constants for chain transfer reactions are as follows:

$$k_{fm,pseudo} = \sum_{i=1}^{6}\sum_{j=1}^{6} k_{fmij}\Phi_i^{\bullet} f_j \tag{55}$$

$$k_{fp,pseudo} = \sum_{i=1}^{6}\sum_{j=1}^{6} k_{fpij}\Phi_i^{\bullet} \overline{F_j} \tag{56}$$

$$k_{fCTA,pseudo} = \sum_{i=1}^{6} k_{fCTAi}\Phi_i^{\bullet}, \quad k_{fS,pseudo} = \sum_{i=1}^{6} k_{fSi}\Phi_i^{\bullet}, \quad k_{fZ,pseudo} = \sum_{i=1}^{6} k_{fZi}\Phi_i^{\bullet} \tag{57}$$

Transfer reactions ideally affect molecular weights but not polymerization rate. In Equations 55 and 56, the *cross*-transfer reaction constants may also be needed, if applicable, based on the reaction mechanism. However, since these values have scarcely been reported, they still remain uncertain. If needed, and for all practical purposes, they can be defined as

$$k_{fmij} = \frac{k_{fmii}}{r_{ij}} \tag{58}$$

$$k_{fpij} = k_{fpjj} \tag{59}$$

Molecular Weight Calculations

The instantaneous number- and weight-average molecular weights (M_n and M_w, respectively) of linear multi-component polymers can be calculated as

$$M_n = \frac{Mw_{eff}}{\tau + 0.5\beta}, \quad M_w = \frac{Mw_{eff}(2\tau + 3\beta)}{(\tau + \beta)^2} \tag{60}$$

where

$$Mw_{eff} = \sum_{i=1}^{6}\left[Mw_i\left(\frac{R_{pi}}{R_p}\right)\right] = \sum_{i=1}^{6}\left(Mw_i F_i\right)$$

$$\tau = \frac{k_{td}[R^{\bullet}] + k_{fCTA}[CTA] + k_{fS}[S] + k_{fZ}[Z]}{k_p[M]} + \frac{k_{fm}}{k_p}, \quad \beta = \frac{k_{tc}[R^{\bullet}]}{k_p[M]}$$

Equation 60 is identical with the *homo*-polymerization case except for the use of the pseudo-effective molecular weight and pseudo-rate constants. The instantaneous weight

fraction of polymer of chain length r at some conversion level X, and hence information about the instantaneous molecular weight distribution, are given as follows:

$$w(r,X)=(\tau+\beta)\left[\tau+\frac{\beta}{2}(\tau+\beta)(r-1)\right]\frac{r}{(1+\tau+\beta)^{r}} \tag{61}$$

The cumulative number-/weight-average molecular weights and weight fraction of polymer of chain length r are given by

$$\overline{M_n}=\frac{X}{\int_0^X M_n^{-1}dX},\quad \overline{M_w}=\frac{1}{X}\int_0^X M_w dX \tag{62}$$

$$\overline{w(r,X)}=\frac{1}{X}\int_0^X w(r,X)dX \tag{63}$$

The equations cited above are valid for linear (non-branched) systems. When additional reactions such as transfer to polymer and/or terminal/internal double bond polymerization are significant, branched or crosslinked polymer molecules are obtained, and hence the method of moments should be applied for the radical and dead polymer distributions. The i^{th} moments of the live radical distribution (λ_i) and dead polymer molecule distribution (μ_i) are defined as

$$\lambda_i=\sum_{r=1}^{\infty} r^i[R_r^\bullet],\quad \mu_i=\sum_{r=1}^{\infty} r^i[P_r] \tag{64}$$

In order to derive moment equations, population balances of live radical and dead polymer molecules are required. As an example, considering the basic reaction steps in *homo*-polymerization for simplicity (initiation, propagation, termination, and chain transfer to monomer and solvent), the balances for radicals of chain length 1 and r, and dead polymer molecules of chain length r, are:

$$\begin{aligned}\frac{d[R_1^\bullet]}{dt}&=2fk_d[I]-k_p[R_1^\bullet][M]-(k_{tc}+k_{td})[R_1^\bullet][R^\bullet]\\&\quad+k_{fm}[M][R^\bullet]+k_{fS}[S][R^\bullet]-k_{fm}[R_1^\bullet][M]-k_{fS}[R_1^\bullet][S]\end{aligned} \tag{65}$$

$$\frac{d[R_r^\bullet]}{dt}=k_p[M]([R_{r-1}^\bullet]-[R_r^\bullet])-(k_{tc}+k_{td})[R_r^\bullet][R^\bullet]-k_{fm}[R_r^\bullet][M]-k_{fS}[R_r^\bullet][S] \tag{66}$$

$$\frac{d[P_r]}{dt} = \frac{1}{2} k_{tc} \sum_{s=1}^{r-1} [R^{\bullet}_{r-s}][R^{\bullet}_s] + k_{td}[R^{\bullet}_r][R^{\bullet}] + k_{fm}[R^{\bullet}_r][M] + k_{fS}[R^{\bullet}_r][S] \tag{67}$$

The zeroth moment of live radicals is calculated as follows:

$$\begin{aligned}
\frac{d\lambda_0}{dt} &= \frac{d\left(\sum_{r=1}^{\infty}[R^{\bullet}_r]\right)}{dt} = \frac{d\left([R^{\bullet}_1] + \sum_{r=2}^{\infty}[R^{\bullet}_r]\right)}{dt} = \frac{d[R^{\bullet}_1]}{dt} + \frac{d\left(\sum_{r=2}^{\infty}[R^{\bullet}_r]\right)}{dt} \\
&= \begin{pmatrix} 2fk_d[I] - k_p[R^{\bullet}_1][M] - (k_{tc} + k_{td})[R^{\bullet}_1][R^{\bullet}] \\ + k_{fm}[M][R^{\bullet}] + k_{fS}[S][R^{\bullet}] - k_{fm}[R^{\bullet}_1][M] - k_{fS}[R^{\bullet}_1][S] \end{pmatrix} \\
&+ \left(k_p[M](\sum_{r=2}^{\infty}[R^{\bullet}_{r-1}] - \sum_{r=2}^{\infty}[R^{\bullet}_r]) - (k_{tc} + k_{td})[R^{\bullet}]\sum_{r=2}^{\infty}[R^{\bullet}_r] - (k_{fm}[M] + k_{fS}[S])\sum_{r=2}^{\infty}[R^{\bullet}_r] \right) \\
&= 2fk_d[I] + k_p[M]\left(\sum_{r=2}^{\infty}[R^{\bullet}_{r-1}] - \sum_{r=2}^{\infty}[R^{\bullet}_r] - [R^{\bullet}_1]\right) - (k_{tc} + k_{td})[R^{\bullet}]\left(\sum_{r=2}^{\infty}[R^{\bullet}_r] + [R^{\bullet}_1]\right) \\
&- \left(k_{fm}[M] + k_{fS}[S]\right)\left(\sum_{r=2}^{\infty}[R^{\bullet}_r] + [R^{\bullet}_1] - [R^{\bullet}]\right) \\
&= 2fk_d[I] - (k_{tc} + k_{td})[R^{\bullet}]^2 = 2fk_d[I] - (k_{tc} + k_{td})\lambda_0{}^2
\end{aligned} \tag{68}$$

since

$$\sum_{r=2}^{\infty}[R^{\bullet}_{r-1}] = \sum_{r=1}^{\infty}[R^{\bullet}_r] = \lambda_0\,, \quad \sum_{r=2}^{\infty}[R^{\bullet}_r] + [R^{\bullet}_1] = \sum_{r=1}^{\infty}[R^{\bullet}_r] = [R^{\bullet}] = \lambda_0$$

The zeroth moment λ_0 is identical with the total radical concentration.

The first and second moments of live radicals subsequently become Equations 69 and 70.

$$\begin{aligned}
\frac{d\lambda_1}{dt} &= \frac{d\left(\sum_{r=1}^{\infty} r[R^{\bullet}_r]\right)}{dt} = \frac{d\left([R^{\bullet}_1] + \sum_{r=2}^{\infty} r[R^{\bullet}_r]\right)}{dt} = \frac{d[R^{\bullet}_1]}{dt} + \frac{d\left(\sum_{r=2}^{\infty} r[R^{\bullet}_r]\right)}{dt} \\
&= \begin{pmatrix} 2fk_d[I] - k_p[R^{\bullet}_1][M] - (k_{tc} + k_{td})[R^{\bullet}_1][R^{\bullet}] \\ + k_{fm}[M][R^{\bullet}] + k_{fS}[S][R^{\bullet}] - k_{fm}[R^{\bullet}_1][M] - k_{fS}[R^{\bullet}_1][S] \end{pmatrix} \\
&+ \left(k_p[M](\sum_{r=2}^{\infty} r[R^{\bullet}_{r-1}] - \sum_{r=2}^{\infty} r[R^{\bullet}_r]) - (k_{tc} + k_{td})[R^{\bullet}]\sum_{r=2}^{\infty} r[R^{\bullet}_r] - (k_{fm}[M] + k_{fS}[S])\sum_{r=2}^{\infty} r[R^{\bullet}_r] \right) \\
&= 2fk_d[I] + k_p[M]\left(\sum_{r=2}^{\infty} r[R^{\bullet}_{r-1}] - \sum_{r=2}^{\infty} r[R^{\bullet}_r] - [R^{\bullet}_1]\right) - (k_{tc} + k_{td})[R^{\bullet}]\left(\sum_{r=2}^{\infty} r[R^{\bullet}_r] + [R^{\bullet}_1]\right) \\
&- \left(k_{fm}[M] + k_{fS}[S]\right)\left(\sum_{r=2}^{\infty} r[R^{\bullet}_r] + [R^{\bullet}_1] - [R^{\bullet}]\right) \\
&= 2fk_d[I] + k_p\lambda_0[M] - (k_{tc} + k_{td})\lambda_0\lambda_1 + \left(k_{fm}[M] + k_{fS}[S]\right)(\lambda_0 - \lambda_1)
\end{aligned} \tag{69}$$

since

$$\sum_{r=2}^{\infty} r[R_{r-1}^{\bullet}] = \sum_{r=1}^{\infty} (r+1)[R_r^{\bullet}] = \sum_{r=1}^{\infty} r[R_r^{\bullet}] + \sum_{r=1}^{\infty} [R_r^{\bullet}] = \lambda_1 + \lambda_0 \,,\ \sum_{r=2}^{\infty} r[R_r^{\bullet}] + [R_1^{\bullet}] = \sum_{r=1}^{\infty} r[R_r^{\bullet}] = \lambda_1$$

$$\frac{d\lambda_2}{dt} = \frac{d\left(\sum_{r=1}^{\infty} r^2[R_r^{\bullet}]\right)}{dt} = \frac{d\left([R_1^{\bullet}] + \sum_{r=2}^{\infty} r^2[R_r^{\bullet}]\right)}{dt} = \frac{d[R_1^{\bullet}]}{dt} + \frac{d\left(\sum_{r=2}^{\infty} r^2[R_r^{\bullet}]\right)}{dt}$$

$$\begin{aligned}
&= \begin{pmatrix} 2fk_d[I] - k_p[R_1^{\bullet}][M] - (k_{tc} + k_{td})[R_1^{\bullet}][R^{\bullet}] \\ + k_{fm}[M][R^{\bullet}] + k_{fS}[S][R^{\bullet}] - k_{fm}[R_1^{\bullet}][M] - k_{fS}[R_1^{\bullet}][S] \end{pmatrix} \\
&+ \begin{pmatrix} k_p[M](\sum_{r=2}^{\infty} r^2[R_{r-1}^{\bullet}] - \sum_{r=2}^{\infty} r^2[R_r^{\bullet}]) - (k_{tc} + k_{td})[R^{\bullet}]\sum_{r=2}^{\infty} r^2[R_r^{\bullet}] \\ - (k_{fm}[M] + k_{fS}[S])\sum_{r=2}^{\infty} r^2[R_r^{\bullet}] \end{pmatrix} \\
&= 2fk_d[I] + k_p[M]\left(\sum_{r=2}^{\infty} r^2[R_{r-1}^{\bullet}] - \sum_{r=2}^{\infty} r^2[R_r^{\bullet}] - [R_1^{\bullet}]\right) - (k_{tc} + k_{td})[R^{\bullet}]\left(\sum_{r=2}^{\infty} r^2[R_r^{\bullet}] + [R_1^{\bullet}]\right) \\
&- \left(k_{fm}[M] + k_{fS}[S]\right)\left(\sum_{r=2}^{\infty} r^2[R_r^{\bullet}] + [R_1^{\bullet}] - [R^{\bullet}]\right) \\
&= 2fk_d[I] + k_p[M](2\lambda_1 + \lambda_0) - (k_{tc} + k_{td})\lambda_0\lambda_2 + \left(k_{fm}[M] + k_{fS}[S]\right)(\lambda_0 - \lambda_2)
\end{aligned} \tag{70}$$

since

$$\sum_{r=2}^{\infty} r^2[R_{r-1}^{\bullet}] = \sum_{r=1}^{\infty} (r+1)^2[R_r^{\bullet}] = \sum_{r=1}^{\infty} (r^2 + 2r + 1)[R_r^{\bullet}] = \lambda_2 + 2\lambda_1 + \lambda_0$$

$$\sum_{r=2}^{\infty} r^2[R_r^{\bullet}] + [R_1^{\bullet}] = \sum_{r=1}^{\infty} r^2[R_r^{\bullet}] = \lambda_2$$

Similarly, the moments for dead polymer molecules can be written as follows:

$$\begin{aligned}
\frac{d\mu_0}{dt} &= \frac{d\left(\sum_{r=1}^{\infty}[P_r]\right)}{dt} \\
&= \frac{1}{2}k_{tc}\sum_{r=2}^{\infty}\sum_{s=1}^{r-1}[R_{r-s}^{\bullet}][R_s^{\bullet}] + k_{td}[R^{\bullet}]\sum_{r=1}^{\infty}[R_r^{\bullet}] + \left(k_{fm}[M] + k_{fS}[S]\right)\sum_{r=1}^{\infty}[R_r^{\bullet}] \\
&= \left(\frac{1}{2}k_{tc} + k_{td}\right)\lambda_0^{\,2} + \left(k_{fm}[M] + k_{fS}[S]\right)\lambda_0
\end{aligned} \tag{71}$$

since

$$\sum_{r=2}^{\infty}\sum_{s=1}^{r-1}[R_{r-s}^{\bullet}][R_s^{\bullet}] = \sum_{r=2}^{\infty}[R_{r-1}^{\bullet}][R_1^{\bullet}] + \sum_{r=3}^{\infty}[R_{r-2}^{\bullet}][R_2^{\bullet}] + \sum_{r=4}^{\infty}[R_{r-3}^{\bullet}][R_3^{\bullet}] + \cdots$$

$$= \sum_{r=1}^{\infty}[R_r^{\bullet}][R_1^{\bullet}] + \sum_{r=1}^{\infty}[R_r^{\bullet}][R_2^{\bullet}] + \sum_{r=1}^{\infty}[R_r^{\bullet}][R_3^{\bullet}] + \cdots$$

$$= \sum_{r=1}^{\infty}[R_r^{\bullet}]\left([R_1^{\bullet}] + [R_2^{\bullet}] + [R_3^{\bullet}] + \cdots\right) = \left(\sum_{r=1}^{\infty}[R_r^{\bullet}]\right)^2 = {\lambda_0}^2$$

$$\frac{d\mu_1}{dt} = \frac{d\left(\sum_{r=1}^{\infty} r[P_r]\right)}{dt}$$

$$= \frac{1}{2}k_{tc}\sum_{r=2}^{\infty} r\sum_{s=1}^{r-1}[R_{r-s}^{\bullet}][R_s^{\bullet}] + k_{td}[R^{\bullet}]\sum_{r=1}^{\infty} r[R_r^{\bullet}] + \left(k_{fm}[M] + k_{fS}[S]\right)\sum_{r=1}^{\infty} r[R_r^{\bullet}] \qquad (72)$$

$$= \left(k_{tc} + k_{td}\right)\lambda_0\lambda_1 + \left(k_{fm}[M] + k_{fS}[S]\right)\lambda_1$$

since

$$\sum_{r=2}^{\infty} r\sum_{s=1}^{r-1}[R_{r-s}^{\bullet}][R_s^{\bullet}] = \sum_{r=2}^{\infty} r[R_{r-1}^{\bullet}][R_1^{\bullet}] + \sum_{r=3}^{\infty} r[R_{r-2}^{\bullet}][R_2^{\bullet}] + \sum_{r=4}^{\infty} r[R_{r-3}^{\bullet}][R_3^{\bullet}] + \cdots$$

$$= \sum_{r=1}^{\infty}(r+1)[R_r^{\bullet}][R_1^{\bullet}] + \sum_{r=1}^{\infty}(r+2)[R_r^{\bullet}][R_2^{\bullet}] + (r+3)\sum_{r=1}^{\infty}[R_r^{\bullet}][R_3^{\bullet}] + \cdots$$

$$= \sum_{r=1}^{\infty} r[R_r^{\bullet}]\left([R_1^{\bullet}] + [R_2^{\bullet}] + [R_3^{\bullet}] + \cdots\right) + \sum_{r=1}^{\infty}[R_r^{\bullet}]\left([R_1^{\bullet}] + 2[R_2^{\bullet}] + 3[R_3^{\bullet}] + \cdots\right)$$

$$= \sum_{r=1}^{\infty} r[R_r^{\bullet}]\sum_{r=1}^{\infty}[R_r^{\bullet}] + \sum_{r=1}^{\infty}[R_r^{\bullet}]\sum_{r=1}^{\infty} r[R_r^{\bullet}] = \lambda_1\lambda_0 + \lambda_0\lambda_1 = 2\lambda_0\lambda_1$$

$$\frac{d\mu_2}{dt} = \frac{d\left(\sum_{r=1}^{\infty} r^2[P_r]\right)}{dt}$$

$$= \frac{1}{2}k_{tc}\sum_{r=2}^{\infty} r^2\sum_{s=1}^{r-1}[R_{r-s}^{\bullet}][R_s^{\bullet}] + k_{td}[R^{\bullet}]\sum_{r=1}^{\infty} r^2[R_r^{\bullet}] + \left(k_{fm}[M] + k_{fS}[S]\right)\sum_{r=1}^{\infty} r^2[R_r^{\bullet}] \qquad (73)$$

$$= \left(k_{tc} + k_{td}\right)\lambda_0\lambda_2 + k_{tc}{\lambda_1}^2 + \left(k_{fm}[M] + k_{fS}[S]\right)\lambda_2$$

since

$$\sum_{r=2}^{\infty} r^2 \sum_{s=1}^{r-1} [R^{\bullet}_{r-s}][R^{\bullet}_{s}] = \sum_{r=2}^{\infty} r^2 [R^{\bullet}_{r-1}][R^{\bullet}_{1}] + \sum_{r=3}^{\infty} r^2 [R^{\bullet}_{r-2}][R^{\bullet}_{2}] + \sum_{r=4}^{\infty} r^2 [R^{\bullet}_{r-3}][R^{\bullet}_{3}] + \cdots$$

$$= \sum_{r=1}^{\infty} (r+1)^2 [R^{\bullet}_{r}][R^{\bullet}_{1}] + \sum_{r=1}^{\infty} (r+2)^2 [R^{\bullet}_{r}][R^{\bullet}_{2}] + (r+3)^2 \sum_{r=1}^{\infty} [R^{\bullet}_{r}][R^{\bullet}_{3}] + \cdots$$

$$= \sum_{r=1}^{\infty} r^2 [R^{\bullet}_{r}]\left([R^{\bullet}_{1}] + [R^{\bullet}_{2}] + [R^{\bullet}_{3}] + \cdots\right) + 2\sum_{r=1}^{\infty} r[R^{\bullet}_{r}]\left([R^{\bullet}_{1}] + 2[R^{\bullet}_{2}] + 3[R^{\bullet}_{3}] + \cdots\right)$$

$$+ \sum_{r=1}^{\infty} [R^{\bullet}_{r}]\left([R^{\bullet}_{1}] + 4[R^{\bullet}_{2}] + 9[R^{\bullet}_{3}] + \cdots\right)$$

$$= \sum_{r=1}^{\infty} r^2 [R^{\bullet}_{r}] \sum_{r=1}^{\infty} [R^{\bullet}_{r}] + 2\sum_{r=1}^{\infty} r[R^{\bullet}_{r}] \sum_{r=1}^{\infty} r[R^{\bullet}_{r}] + \sum_{r=1}^{\infty} [R^{\bullet}_{r}] \sum_{r=1}^{\infty} r^2 [R^{\bullet}_{r}]$$

$$= \lambda_2 \lambda_0 + 2\lambda_1^{\,2} + \lambda_0 \lambda_2 = 2\lambda_0 \lambda_2 + 2\lambda_1^{\,2}$$

Now, considering all possible reaction steps mentioned earlier and including chain transfer to polymer and internal/terminal double bond polymerization, the moment Equations 68 to 73 can be written as

$$\frac{d\lambda_0}{dt} = R_i - k_t \lambda_0^2 - k_{fZ} \lambda_0 [Z] \tag{74}$$

$$\frac{d\lambda_1}{dt} = R_i + k_p [M] \lambda_0 - k_t \lambda_0 \lambda_1 + \left(k_{fCTA}[CTA] + k_{fm}[M] + k_{fS}[S]\right)(\lambda_0 - \lambda_1) + k_{fP}\left(\lambda_0 \mu_2 - \lambda_1 \mu_1\right) + k_p^{*}\left(\lambda_0 \mu_1 - \lambda_1 \mu_1 + \lambda_1 \mu_0\right) + k_p^{**} \lambda_0 \mu_2 - k_{fZ}[Z] \lambda_1 \tag{75}$$

$$\frac{d\lambda_2}{dt} = R_i + k_p [M](\lambda_0 + 2\lambda_1) - k_t \lambda_0 \lambda_2 + \left(k_{fCTA}[CTA] + k_{fm}[M] + k_{fS}[S]\right)(\lambda_0 - \lambda_2) + k_{fP}\left(\lambda_0 \mu_3 - \lambda_2 \mu_1\right) + k_p^{*}\left(\lambda_0 \mu_2 + 2\lambda_1 \mu_1 + \lambda_2 \mu_0 - \lambda_2 \mu_1\right) + k_p^{**}\left(\lambda_0 \mu_3 + 2\lambda_1 \mu_2\right) - k_{fZ}[Z] \lambda_2 \tag{76}$$

$$\frac{d\mu_0}{dt} = \left(\frac{1}{2} k_{tc} + k_{td}\right) \lambda_0^2 + \left(k_{fm}[M] + k_{fCTA}[CTA] + k_{fS}[S] + k_{fZ}[Z] - k_p^{*} \mu_0 - k_p^{**} \mu_1\right) \lambda_0 \tag{77}$$

$$\frac{d\mu_1}{dt} = \left(k_{tc} + k_{td}\right) \lambda_0 \lambda_1 + \left(k_{fm}[M] + k_{fCTA}[CTA] + k_{fS}[S] + k_{fZ}[Z]\right) \lambda_1 + k_{fp}\left(\lambda_1 \mu_1 - \lambda_0 \mu_2\right) - \left(k_p^{*} \lambda_0 \mu_1 + k_p^{**} \lambda_0 \mu_2\right) \tag{78}$$

$$\frac{d\mu_2}{dt} = k_{tc}\left(\lambda_0 \lambda_2 + \lambda_1^{\,2}\right) + k_{td} \lambda_0 \lambda_2 + \left(k_{fm}[M] + k_{fCTA}[CTA] + k_{fS}[S] + k_{fZ}[Z]\right) \lambda_2 + k_{fp}\left(\lambda_2 \mu_1 - \lambda_0 \mu_3\right) - \left(k_p^{*} \lambda_0 \mu_2 + k_p^{**} \lambda_0 \mu_3\right) \tag{79}$$

In order to calculate μ_3 and avoid open-ended equations, $\mu_3 \approx \frac{\mu_2}{\mu_0 \mu_1}\left(2\mu_0\mu_2 - \mu_2^2\right)$ is usually employed for moment closure. Using the moment equations above, the cumulative number-/weight-average molecular weights of a multi-component polymer are calculated by:

$$\overline{\overline{M}}_n = Mw_{eff}\,\frac{\mu_1}{\mu_0} \tag{80}$$

$$\overline{\overline{M}}_w = Mw_{eff}\,\frac{\mu_2}{\mu_1} \tag{81}$$

Moment equations for calculation of molecular weight averages appear in the literature in different shapes and forms, often including only some of the previously cited reactions, and often derived with certain simplifying (yet valid) assumptions. For instance, as an example, see different yet equivalent versions of these moment equations in references (32-33).

Finally, as an indicator of long chain branching/crosslinking, the average number of *tri-*/*tetra*-functional branches per molecule can be computed from the following equations (32-33):

$$\frac{d\left(\mu_0\,\overline{\overline{B}}_{N3}\right)}{dt} = \left(k_{fp}\mu_1 + k_p^*\mu_0\right)\lambda_0 \tag{82}$$

$$\frac{d(\mu_0\,\overline{\overline{B}}_{N4})}{dt} = k_p^{**}\mu_2\lambda_0 \tag{83}$$

Diffusion Control Kinetics

The termination, propagation, transfer reaction rate constants and the initiator efficiency can all be affected by the presence of diffusional limitations throughout the polymerization and may show significant decreases. In bulk and concentrated solution polymerizations, the reaction rate rises remarkably at some conversion level between 20 and 50%, and this leads to significant increases in polymer molecular weights. Furthermore, it has been frequently observed at high conversion that the reaction rate

falls rapidly and a limiting conversion appears in spite of sufficient initiator/monomer amounts still unreacted. The former phenomenon is referred to as autoacceleration, Trommsdorff-Smith-Norrish, or simply gel effect, while the latter one is usually referred to as the glassy effect.

It is established that autoacceleration happens due to diffusional (mobility) limitations of radicals and macromolecules. As polymerization proceeds, the growing entangled polymer chains increase the reaction medium viscosity and the reduced radical mobility hinders further termination, while initiator is continuously decomposing into radicals and the radical chains keep propagating (growing). As a result, the radical concentration increases considerably and so does polymerization rate (and eventually molecular weights).

Several different approaches have been introduced to explain the autoacceleration and glassy effects as a function of other process variables. We invoke the free volume approach, which is a very powerful and well-tested semi-empirical model. The free volume equation is expressed as:

$$V_f = \sum_{i=1}^{n} [V_{f,i}^0 + \alpha_i (T - T_{g,i})] \frac{V_i}{V} \tag{84}$$

where

i is a reaction mixture component (monomer, polymer, and solvent)

$V_{f,i}^0$ is free volume of component i at the glass transition temperature

α_i is thermal expansion coefficient (difference) above and below T_g

T is reaction temperature

T_{gi} is glass transition temperature for component i

V_i, V are volume for component i and total reaction volume, respectively.

Free volume theory has suggested the 'universal values' of 0.025 for $V_{f,i}^0$ and 0.001 for α_i, for monomer(s) and solvent, and of 0.00048 for the polymer. However, where appropriate data exist, these parameters may be estimated for the specific system in

question. The glass transition temperature of the polymer (T_{gpoly}) at some conversion level can be calculated using Johnston's method:

$$\frac{1}{T_{gpoly}} = \sum_{i=1}^{6} \frac{w_i p_{ii}}{T_{gpi}} + \sum_{i=1}^{6} \sum_{\substack{j=2 \\ (j \neq i)}}^{6} \frac{w_i p_{ij} + w_j p_{ji}}{T_{gpij}} \tag{85}$$

where T_{gpi} is the glass transition temperature for the *homo*-polymer species i, T_{gpij} is that of an (ideal) alternating *co*-polymer coming from monomers i and j, w_i is the weight fraction of monomer i bound in the polymer chains, and p_{ij} is the probability of forming a dyad of monomers i and j, which has been defined earlier.

A decrease for k_t will be observed first because termination is chemically the fastest step and large macroradicals are involved (and are hence more vulnerable to restrictions of mobility). The diffusion control of the overall (pseudo-) k_t is usually divided into three intervals: segmental, translational, and reaction-diffusion. Even at low conversions, the termination rate may be controlled by segmental diffusion, which is described according to (32) as follows:

$$k_{t,seg} = k_{t,pseudo}\left(1 + \delta_c\, c\right) \tag{86}$$

where

$k_{t,pseudo}$ is the chemically controlled pseudo-termination rate constant in Equation 54

δ_c is a parameter dependent on molecular weight and solvent quality

c is the mass concentration of accumulated polymer.

In this region, when the reaction medium is a thermodynamically "good solvent", the polymer coil size decreases and the termination rate constant may actually increase until the onset of translational diffusion. To recap, in the first (segmental diffusion) interval, the overall termination rate constant is equal to the segmental diffusion termination rate constant ($k_{t,seg}$) plus the reaction-diffusion termination rate constant (to be discussed shortly), as per Equation 87:

$$k_{t,overall} = k_{t,seg} + k_{t,rd} \tag{87}$$

The second interval, translational diffusion or gel effect region, is determined by a gel effect parameter K_3 suggested by Marten and Hamielec (34):

$$K_3 = \overline{\overline{M}}_{w\,cr}^{\,m} \exp\left(\frac{A}{V_{f,cr1}}\right) \tag{88}$$

where

$\overline{\overline{M}}_{w\,cr}$ is a critical accumulated weight-average molecular weight of polymer

$V_{f,cr1}$ is a critical free-volume

A, *m* are gel effect model parameters for the specific monomer system found in the monomer database; usually, $m = 0.5$.

Stickler *et al*. (35) performed experiments to determine K_3 values in MMA polymerization and built a temperature-dependent Arrhenius expression for K_3. In the multi-component case, we used the Arrhenius form and calculated a pseudo-K_3, composed of the individual values of $K_{3,i}$ via superposition.

$$K_{3,i} = A_{K,i} \exp\left(\frac{E_{K,i}}{RT}\right) \tag{89}$$

$$K_{3,pseudo} = \exp\left[1/\sum_{i=1}^{6}\left(\frac{\overline{\overline{F}}_i}{\log(K_{3,i})}\right)\right] \tag{90}$$

where $\overline{\overline{F}}_i$ is the cumulative polymer composition of monomer species *i*.

$K_{3,pseudo}$ in Equation 90 can be calculated for the polymer system in question based on the characteristics of each monomer in the species database.

In the model, the calculated $K_{3,test}$ (see Equation 91) is compared with the predetermined $K_{3,pseudo}$ of Equation 90 as conversion varies:

$$K_{3,test} = \overline{\overline{M}}_{w}^{\,m} \exp\left(\frac{A_{pseudo}}{V_f}\right) \tag{91}$$

$$\frac{1}{A_{pseudo}} = \sum_{i=1}^{6}\left(\frac{F_i}{A_i}\right) \tag{92}$$

where A_i and F_i are the gel effect model parameter and instantaneous polymer composition for monomer species *i*, respectively. For A_i, see the discussion around Equation 88. These A_i parameters are combined into a pseudo-gel effect model parameter A_{pseudo} for the multi-component case, as per Equation 92.

When $K_{3,test}$ becomes equal to or greater than $K_{3,pseudo}$, then the corresponding $\overline{\overline{M}}_w$ and V_f (from Equation 91) at the specific time (conversion) step become $\overline{\overline{M}}_{w\,cr}$ and $V_{f,cr1}$, respectively. This signifies the onset of the gel effect (translational diffusion region) and the translationally diffusion-controlled termination rate constant is now governed by Equation 93:

$$k_{t,trans} = k_{t,cr}\left(\frac{\overline{\overline{M}}_{w\,cr}}{\overline{\overline{M}}_w}\right)^n \exp\left[-A_{pseudo}\left(\frac{1}{V_f} - \frac{1}{V_{f,cr1}}\right)\right] \tag{93}$$

where $k_{t,cr}$ is the overall termination constant at the critical point, and *n* is a parameter, usually equal to 1.75. This termination rate constant $k_{t,trans}$ will be observed to decrease significantly in this region.

To recap, in this second (translational diffusion) interval, the overall termination rate constant is equal to the translational diffusion termination rate constant ($k_{t,trans}$) plus the reaction-diffusion termination rate constant, as per Equation 94:

$$k_{t,overall} = k_{t,trans} + k_{t,rd} \tag{94}$$

At very high conversion (usually, above 85%), it is expected that the chain mobility affected by translational diffusion will decrease so greatly that radical chains cannot move any more. However, two macroradical ends may move toward each other by monomer addition. This final interval, reaction-diffusion or residual termination, is described as

$$k_{t,rd} = \frac{8\pi N_A \delta D}{1000} \tag{95}$$

$$\delta = \left(\frac{6V_m}{\pi N_A} \right)^{1/3} \tag{96}$$

$$D = \frac{n_s l_0^{\,2}}{6} k_p [M] \tag{97}$$

where

N_A is Avogadro's number

D is a reaction-diffusion coefficient

δ is a reaction radius

V_m is the molar volume of monomer

n_s is the average number of monomer units in a polymer chain

l_0 is the length of a monomer unit in the chain

k_p is the propagation rate constant

[M] is monomer concentration.

In this final interval, the overall termination rate constant is the same as in Equation 94. Stickler (36) and Stickler *et al*. (35) enhanced their kinetic model by adding $k_{t,rd}$ to $k_{t,trans}$ in Equation 94, thus achieving a very good agreement between conversion data and model predictions in MMA polymerization.

Under polymerization conditions where the reaction temperature is lower than the glass-transition temperature of the polymerizing mixture being synthesized, even the mobility of small monomer units is limited by diffusion in essentially a solid (glassy) polymer matrix. Thus, even propagation/transfer reactions become diffusion-controlled. The onset happens when the free volume of the polymerizing mixture becomes lower than an experimentally determined critical free volume, and this can be modeled similarly to translational diffusion-controlled termination:

$$k_p = k_{p0} \exp\left[-B\left(\frac{1}{V_f} - \frac{1}{V_{f,cr2}} \right) \right] \tag{98}$$

$$k_{f,smallmoleale} = k_{f0} \exp\left[-B\left(\frac{1}{V_f} - \frac{1}{V_{f,cr2}} \right) \right] \tag{99}$$

where

k_{p0} and k_{f0} are the chemically controlled propagation/transfer rate constants

B is the glass-transition effect model parameter

$V_{f,cr2}$ is the critical free volume for diffusion control of propagation/transfer rate constants.

In addition, the initiator efficiency can also undergo diffusion control and begin to decrease at high conversion, in a way similar to k_p. When the free volume of the reaction medium becomes less than an experimentally determined critical free volume, initiator efficiency is calculated using

$$f = f_0 \exp\left[-C\left(\frac{1}{V_f} - \frac{1}{V_{f,cr3}}\right)\right] \tag{100}$$

where

f_0 is the initial initiator efficiency

C is the efficiency-related model parameter

$V_{f,cr3}$ is the critical free volume for diffusion control of initiator efficiency.

3 Results and Discussion

The multi-component polymerization model has been widely tested with experimental data from various monomer systems: for example, *homo*-polymerizations of Sty, MMA, HEA, BA, and BMA; *co*-polymerizations of Sty/acrylonitrile (AN), MMA/BA, Sty/HEA, Sty/BA, Sty/BMA, and AMS/MMA; *ter*-polymerizations of Sty/BMA/hydroxyethyl methacrylate (HEMA), AMS/MMA/BA, Sty/ethyl acrylate (EA)/HEA, MMA/BA/vinyl acetate (VAc); and *tetra*-polymerization of Sty/ (EA)/HEA/MAA. This testing is further to the extensive model and ingredient database testing described previously in references (2-8). Testing includes a wide range of polymerization conditions and recipes, with both commonly employed and less frequently encountered monomer systems. Sample experimental results and model predictions are presented in the subsections below according to various recipes and conditions. This important exercise clearly shows that the multi-component model can successfully reduce to simpler cases, thus increasing

one's confidence in the reliability of the model and the accompanying (unaltered) ingredient database.

3.1 Sty *Homo*-polymerization

Sty is a monomer that has been extensively studied by many researchers. Figure 1 shows Sty bulk *homo*-polymerization (with 2,2'-azo-bis-isobutyronitrile (AIBN) initiator) model predictions vs. experimental data (37). Predictions and data show good agreement over the entire conversion range. The most distinctive characteristic of Sty is that it undergoes thermal self-polymerization without initiator at higher temperatures (over 100℃). Additionally, chain transfer to thermal initiation byproducts can affect molecular weights (24), according to:

$$\tau_{total} = \tau - \left(1.013\times10^{-3}\right)\log_{10}\left(\frac{473.12-T}{202.5}\right)X \tag{101}$$

where $\tau = \dfrac{k_{td}[R^{\bullet}] + k_{fCTA}[CTA] + k_{fS}[S] + k_{fZ}[Z]}{k_p[M]} + \dfrac{k_{fm}}{k_p}$, T is the reaction temperature (K), and X is overall conversion.

Figures 2 and 3 are example plots of Sty bulk thermal polymerization at 170℃, with experimental data from (24). The model gives satisfactory predictions of both conversion and molecular weight averages ('acc' in Figure 3 (and form here on in other figures that will follow) refers to an accumulated or cumulative property).

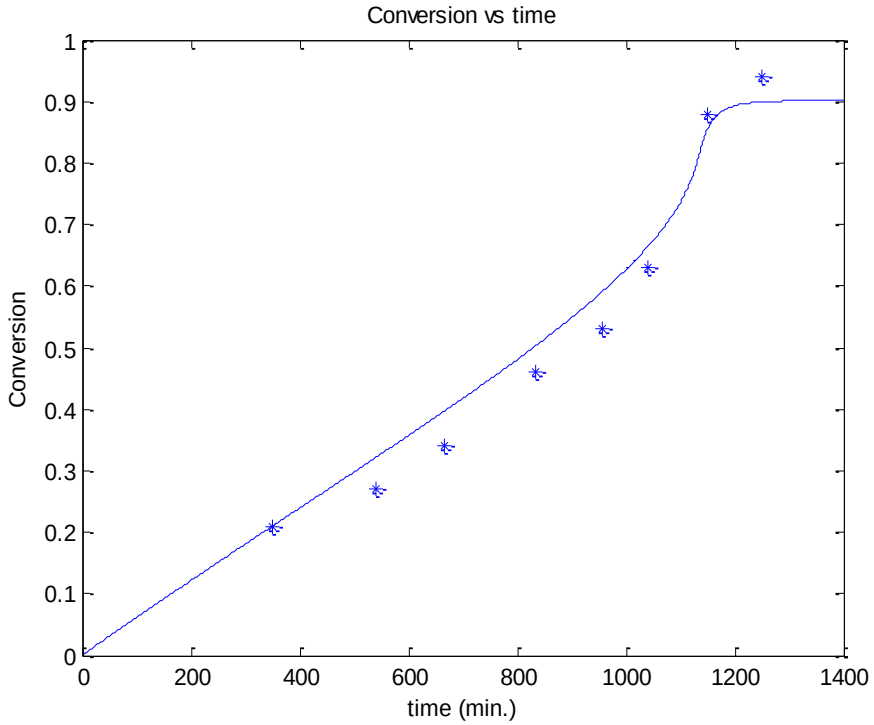

Figure 1. Simulation of bulk polymerization of Sty at 60℃, $[AIBN]_0$ = 0.0164 M

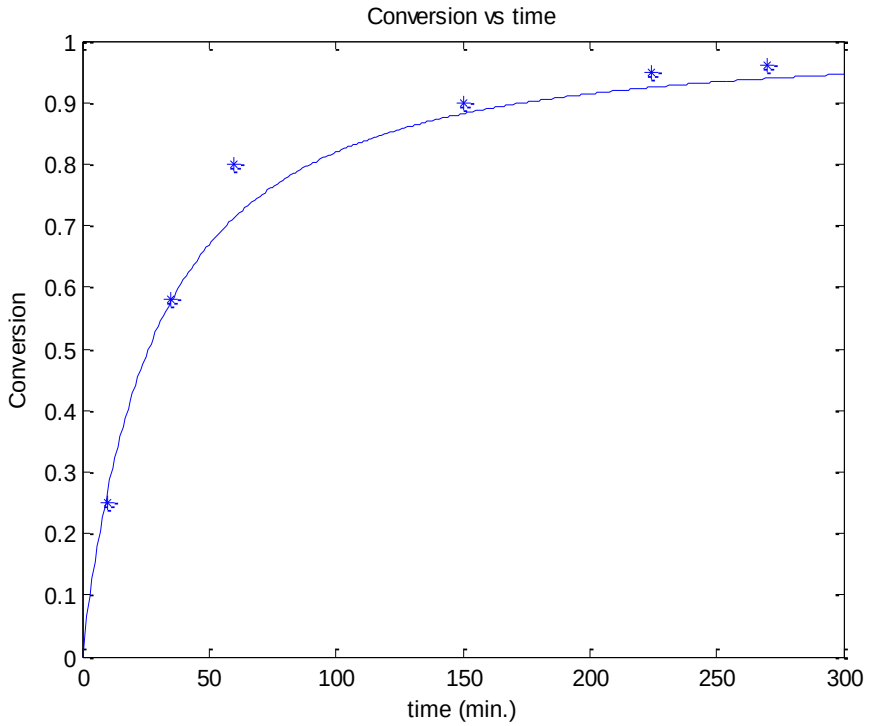

Figure 2. Simulation of bulk thermal polymerization of Sty at 170℃

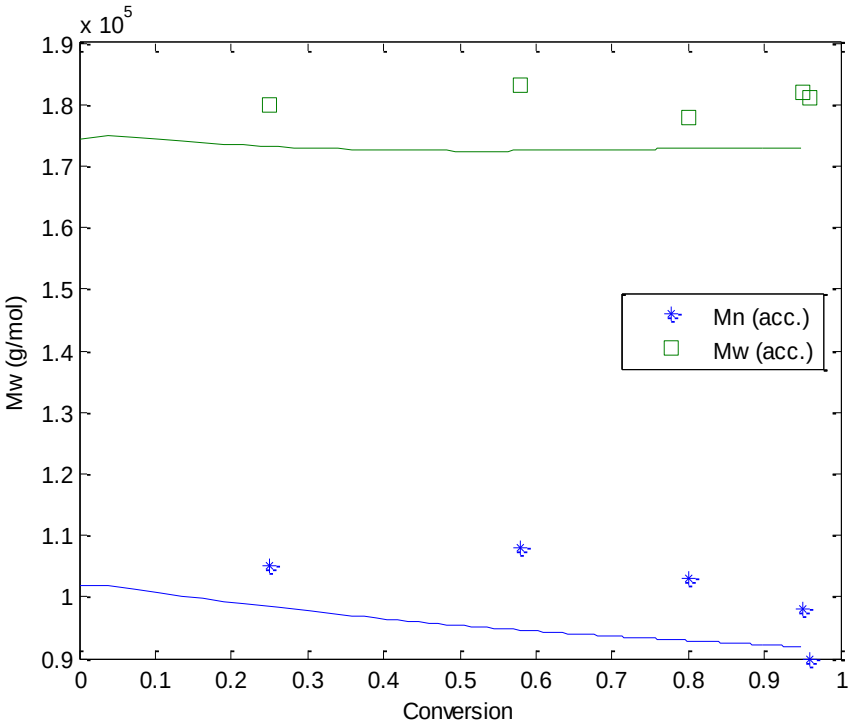

Figure 3. Simulation of molecular weights of Sty thermal polymerization at 170℃

3.2 MMA *Homo*-polymerization

MMA is another widely studied monomer. The model is tested with the experimental data in (38), related to bulk polymerization experiments at 50, 70, and 90℃ using two AIBN initiator concentration levels (0.0258 and 0.01548 mol/L). Figure 4 represents model predictions and experimental data of conversion at $[I]_0$ = 0.0258 mol/L. The expected temperature effect on polymerization rate is evident and captured well by the model.

Figures 5 and 6 show number-/weight-average molecular weight results. The model predictions again follow the experimental data well in this monomer system. Molecular weights decrease as reaction temperature increases, and the model successfully explains free-radical polymerization trends.

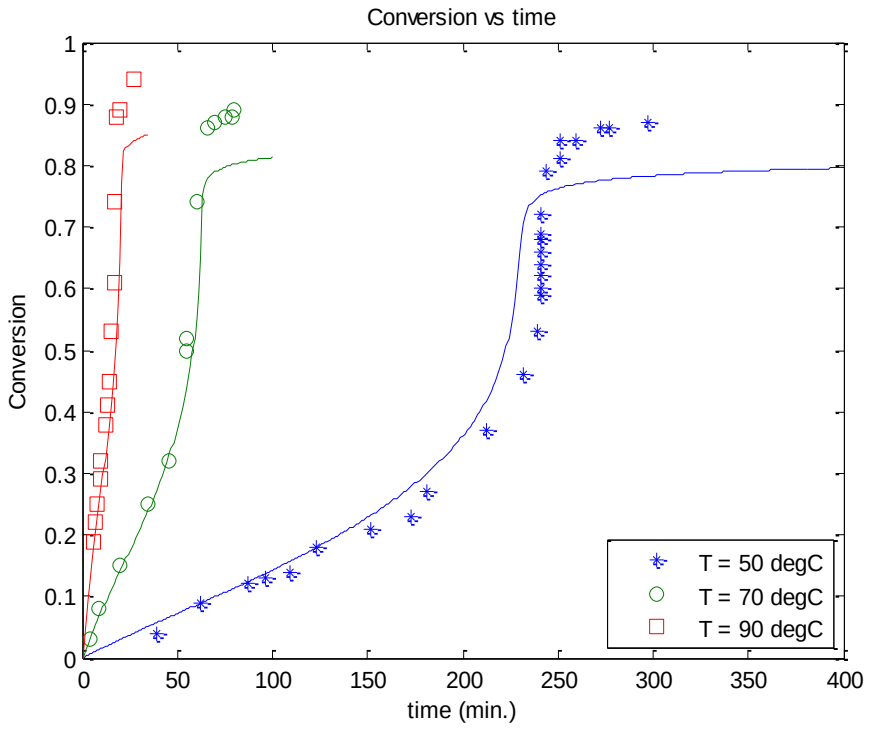

Figure 4. Simulation of bulk polymerizations of MMA at 50, 70, and 90℃, $[AIBN]_0$ = 0.0258 M

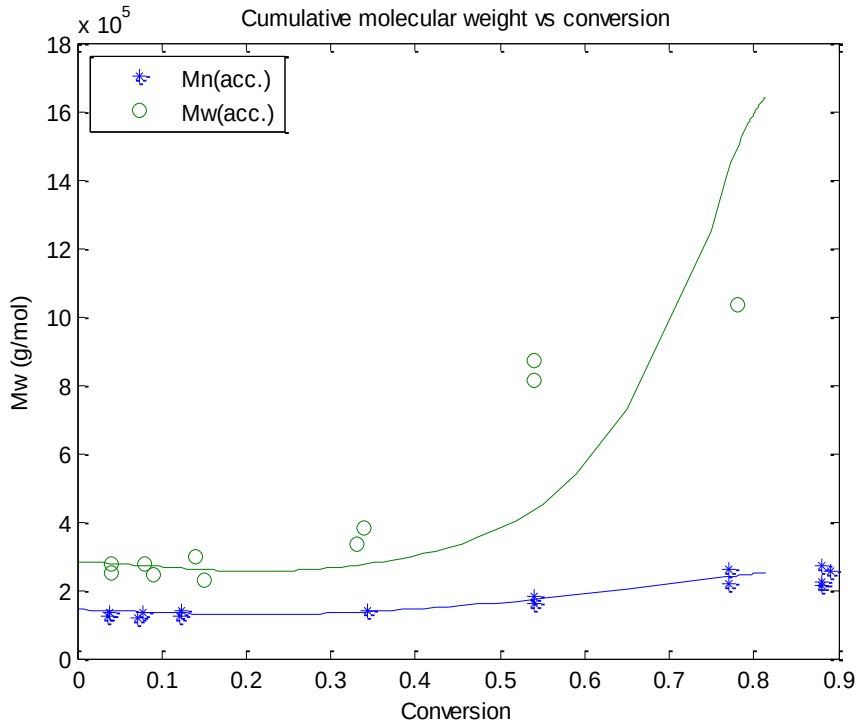

Figure 5. Molecular weight predictions for MMA polymerization at 70℃, $[AIBN]_0 = 0.0258$ M

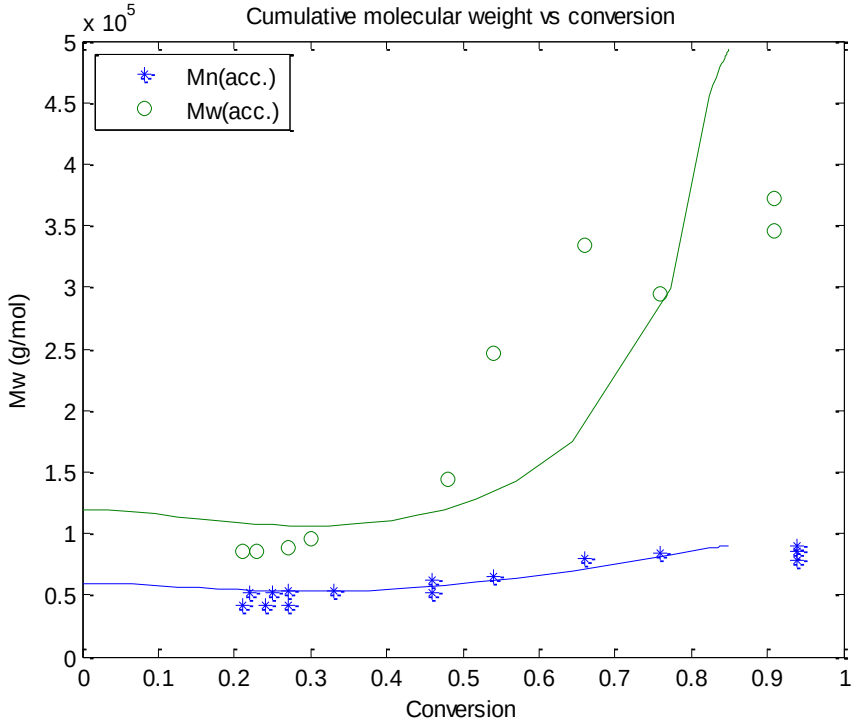

Figure 6. Molecular weight predictions for MMA polymerization at 90℃, $[AIBN]_0 = 0.0258$ M

3.3 HEA *Homo*-polymerization

HEA *homo*-polymerization rate constants could be estimated based on polymerization kinetic data by Kim (39). The multi-component model was also compared in Figure 7 with experimental data (at three different temperature levels (50, 60, and 70℃) with $6.6x10^{-5}$ moles of BPO (benzoyl peroxide) initiator) collected by (40). Fast rates and no limiting conversion are observed in the plot and certain discrepancies are observed at high conversion levels and higher temperatures (60 and 70℃), for this largely unstudied and very fast-reacting monomer that yields highly viscous polymerizing mixtures (see also section 3.8). This monomer is used later in this paper for further model testing of *co*-, *ter*-, and *tetra*-polymerizations.

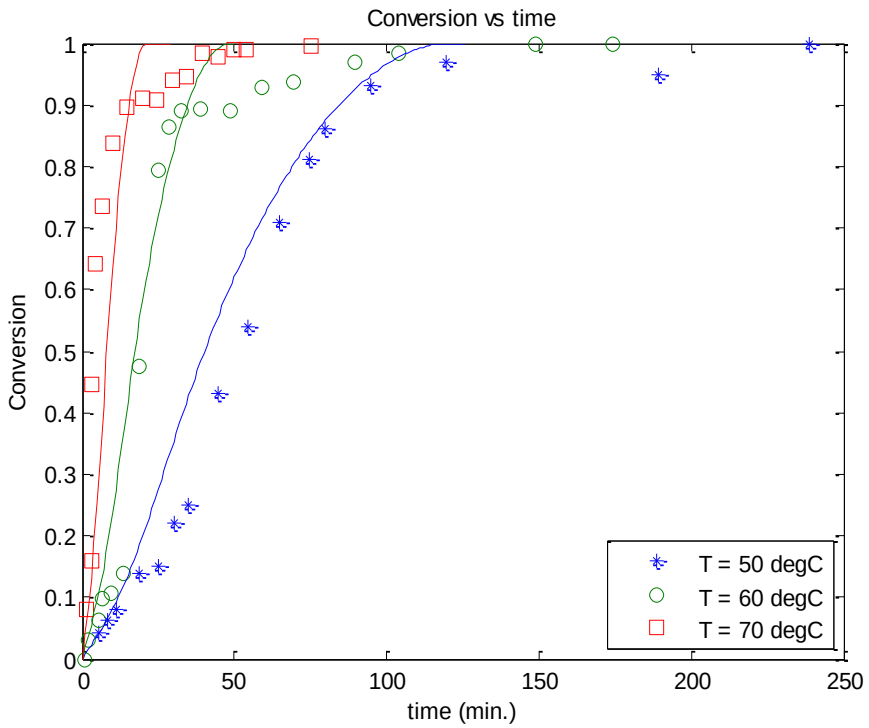

Figure 7. Simulation of bulk polymerizations of HEA with BPO

3.4 BA *Homo*-polymerization

Kinetic and experimental information on BA is not as readily available as for Sty or MMA. Dubé *et al.* (41) performed full conversion range experiments of BA polymerization using a 2^2 factorial design (T = 50 and 60℃, and $[AIBN]_0$ = 0.001 M, 0.00025 M). BA polymerization is a fast reaction characterized by a high k_p value. Representative results are shown in Figure 8. The glass transition temperature of BA polymer is low (about -50℃) and there is significant branching formation via transfer to polymer and terminal double bond polymerization (at this point, model testing has been conducted neglecting backbiting reactions due to the lower temperatures employed). The model follows the experimental data well at low to medium conversion levels, but slight discrepancies are observed at high conversion level. Due to complete lack of data in the literature, the number-/weight-average molecular weight profiles could not be compared.

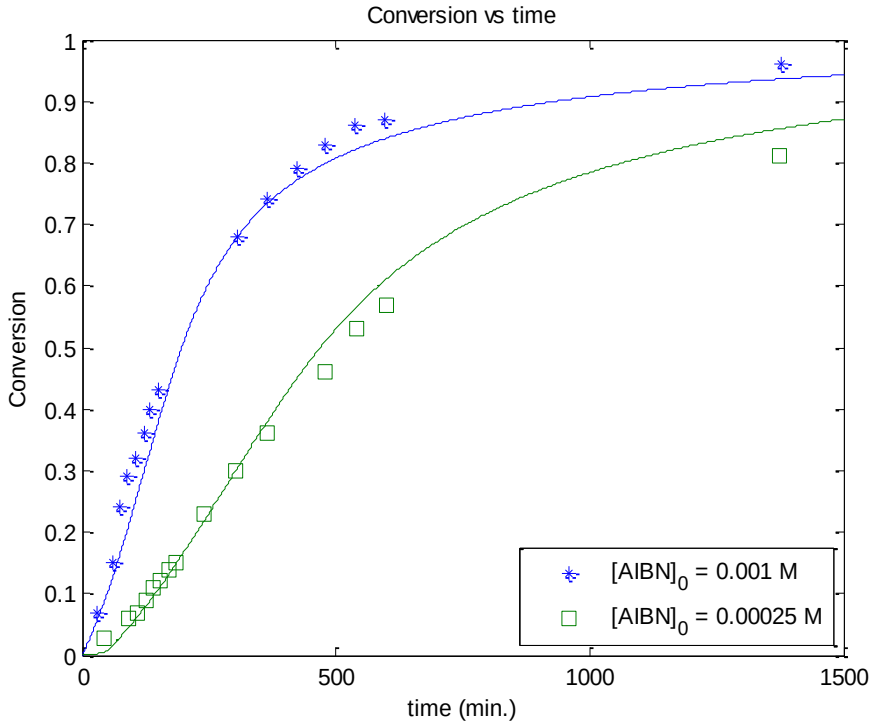

Figure 8. Simulation of bulk polymerizations of BA at 50℃

3.5 BMA *Homo*-polymerization

Model predictions are compared with experimental data reported by (42), obtained at 60℃ using 2,2'-azo-bis-isobutyronitrile (AIBN) initiator. Figure 9 represents bulk polymerization results at different concentration levels of AIBN. The model predictions are good. At this stage of testing, depropagation is not active due to regular temperature levels being employed.

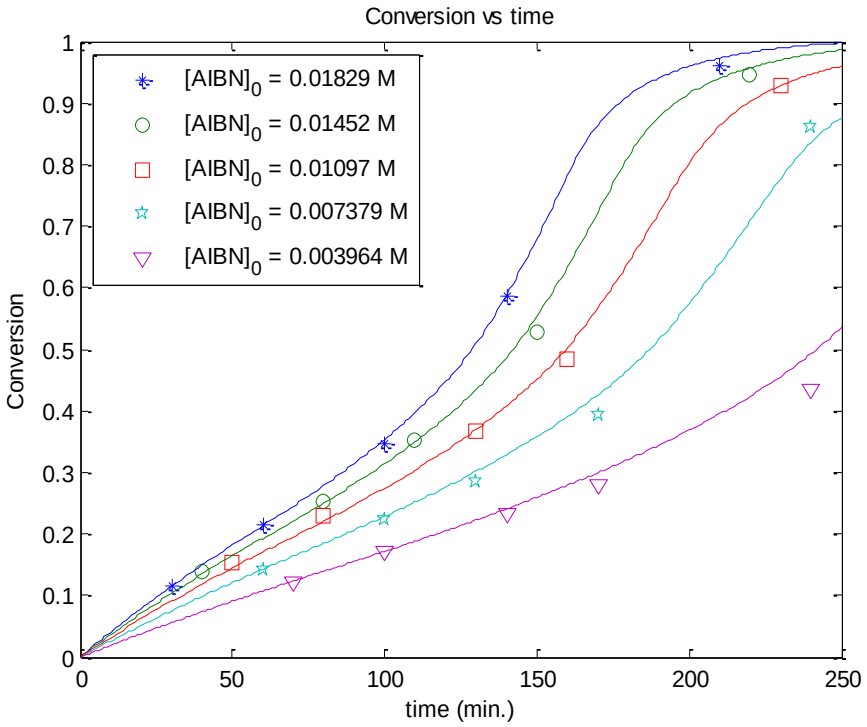

Figure 9. Simulation of bulk polymerizations of BMA at 60℃ with AIBN

3.6 MMA/BA *Co*-polymerization

Dubé and Penlidis (43) investigated MMA/BA *co*-polymer systems as part of a MMA/BA/VAc *ter*-polymerization study. Reactivity ratios were estimated as $r_{MMA\text{-}BA}$ = 1.789 and $r_{BA\text{-}MMA}$ = 0.297 (by the error-in-variables-model (EVM) method). The reactivity ratio values indicate that for this system there is no azeotropic composition and hence composition drift is expected for all monomer feed compositions. Figure 10 represents conversion profiles at a certain BA feed fraction (f_{BA0} = 0.439) at 60℃ with two initiator levels ($[AIBN]_0$ = 0.005 and 0.01 mol/L).

Figure 11 shows the composition drift of BA in the polymer. Significant drift is observed and the drift is not affected by the initiator concentration change. Figure 12 and 13 show the measured number-/weight-average molecular weights and corresponding predictions at different initiator levels. Model predictions give reasonable trends for this system.

Alb *et al*. (44) conducted BA/MMA solution *co*-polymerization with 70 wt% of butyl acetate solvent and 2 wt% of AIBN initiator at 66℃ under different initial monomer feed ratios (weight basis) using an automatic continuous online spectrum-monitoring technique, which enables the determination of instantaneous polymer compositions. Note that Figure 14 represents the instantaneous (not cumulative) composition drift of BA as a function of conversion. Looking at the reactivity ratios, it is evident that MMA incorporation into the polymer is more favored over BA, which leads to larger composition drift at higher initial BA/MMA feed ratios, since MMA is depleted earlier than BA. This can also be verified via the corresponding differential *co*-polymer composition distribution in Figure 15. The values of the y-axis represent the absolute values of the infinitesimal change of total conversion divided by the infinitesimal change of instantaneous polymer composition of BA, namely, the values of the inverse slopes of Figure 14. At the early stages of the *co*-polymerization, more MMA monomer is incorporated into the *co*-polymer than BA; the BA mole fraction in the *co*-polymer does not change much. Therefore, it is observed that with a higher initial MMA content in the system, the slope $|dF_{BA}/dX|$ becomes smaller in Figure 14, while the inverse slope $|dX/dF_{BA}|$ (the y-axis value of Figure 15, calculated numerically as $|\Delta X/\Delta F_{BA}|$) becomes

larger (the prediction profiles are also changing from 'J-shape' to 'U-shape' curves). Meyer and Lowry (45) reported that this 'U-shaped' differential *co*-polymer composition distribution is considered as characteristic of "incompatible" *co*-polymerizations when differences between reactivity ratios are relatively large. During the entire reaction, a virtual "*homo*-polymerization" of the more reactive monomer is favoured initially, while the "*homo*-polymerization" of the less reactive monomer takes place during the later or final stages of the *co*-polymerization.

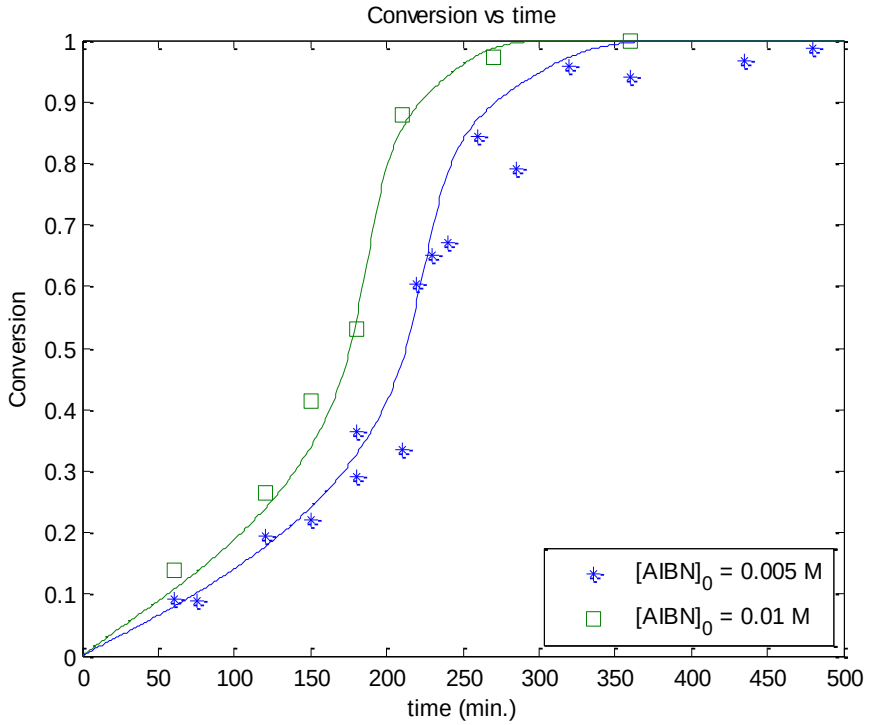

Figure 10. Simulation of bulk *co*-polymerizations of BA/MMA, T = 60℃, f_{BA0} = 0.439

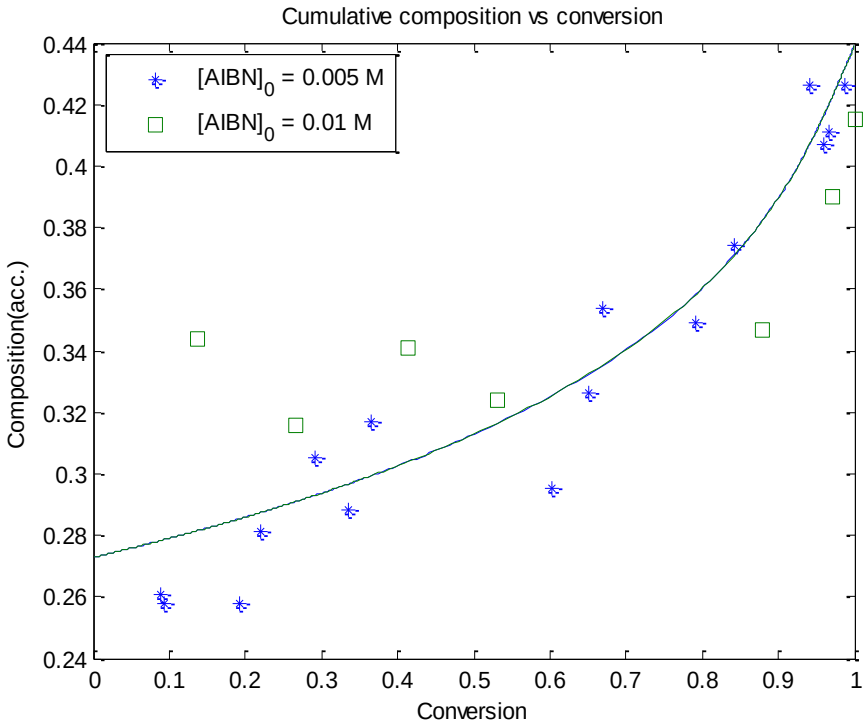

Figure 11. Cumulative polymer composition of BA in BA/MMA *co*-polymerization T = 60℃ and f_{BA0} = 0.439

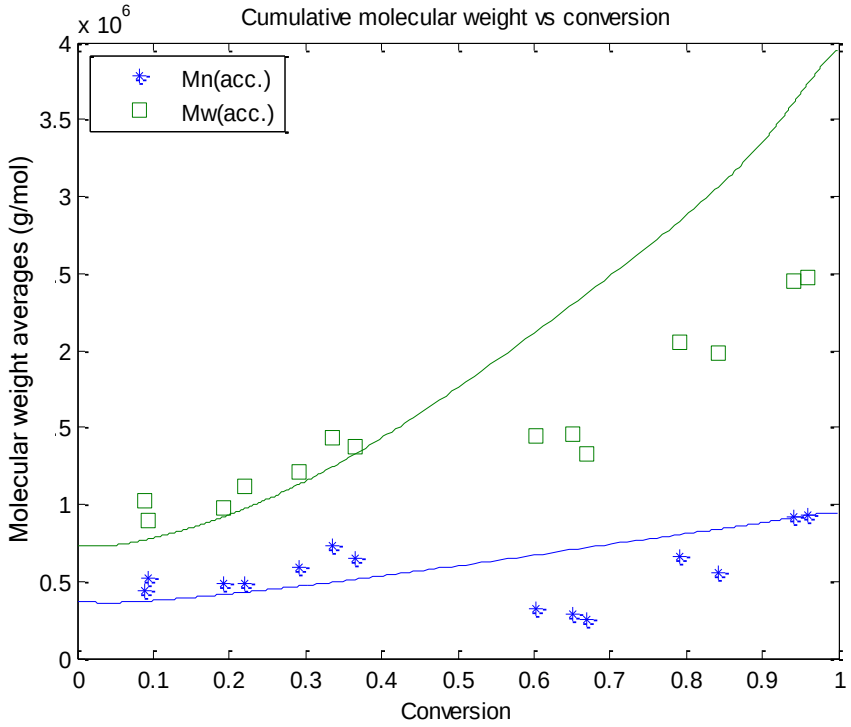

Figure 12. Molecular weight averages of BA/MMA *co*-polymerization T = 60℃, $[AIBN]_0$ = 0.005 M, and f_{BA0} = 0.439

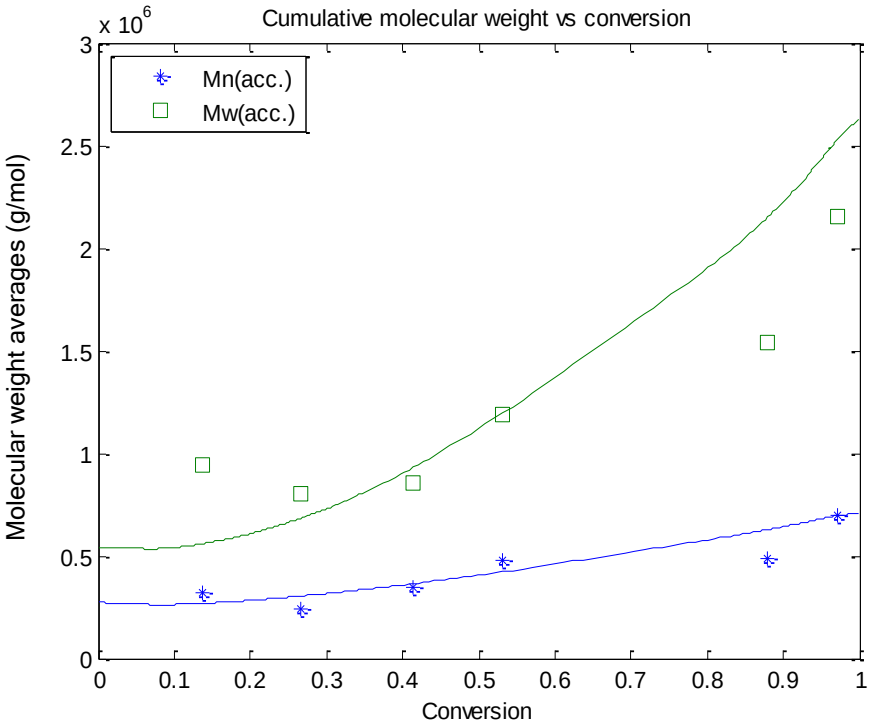

Figure 13. Molecular weight averages of BA/MMA *co*-polymerization
T = 60℃, $[AIBN]_0$ = 0.01 M, and f_{BA0} = 0.439

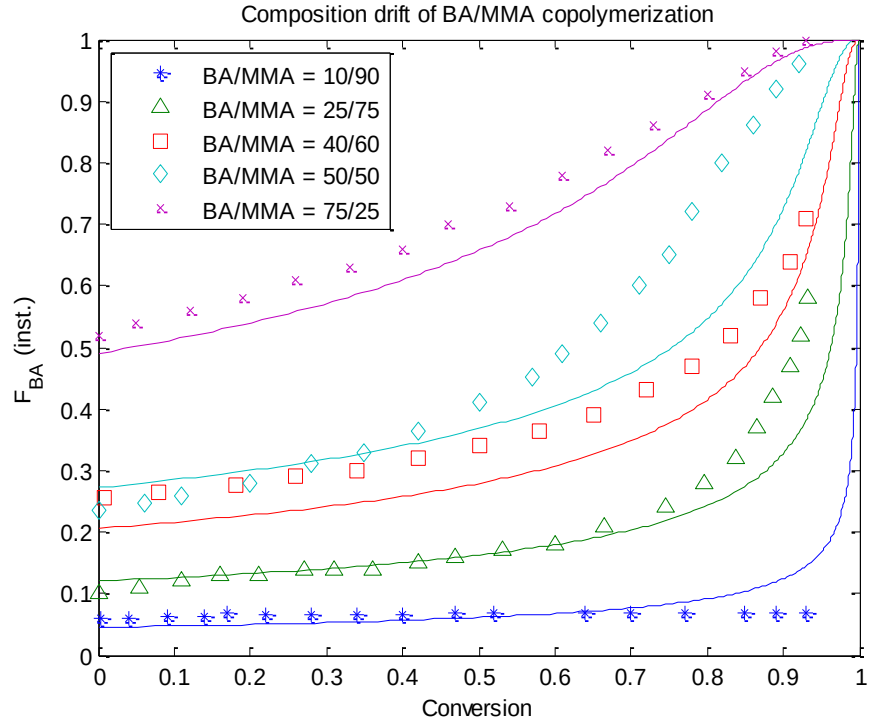

Figure 14. Simulation of composition drift of instantaneous F_{BA} in BA/MMA *co*-polymerization
T = 66℃, Butyl acetate (solvent) = 70 wt%, and AIBN = 2 wt% of total mixture

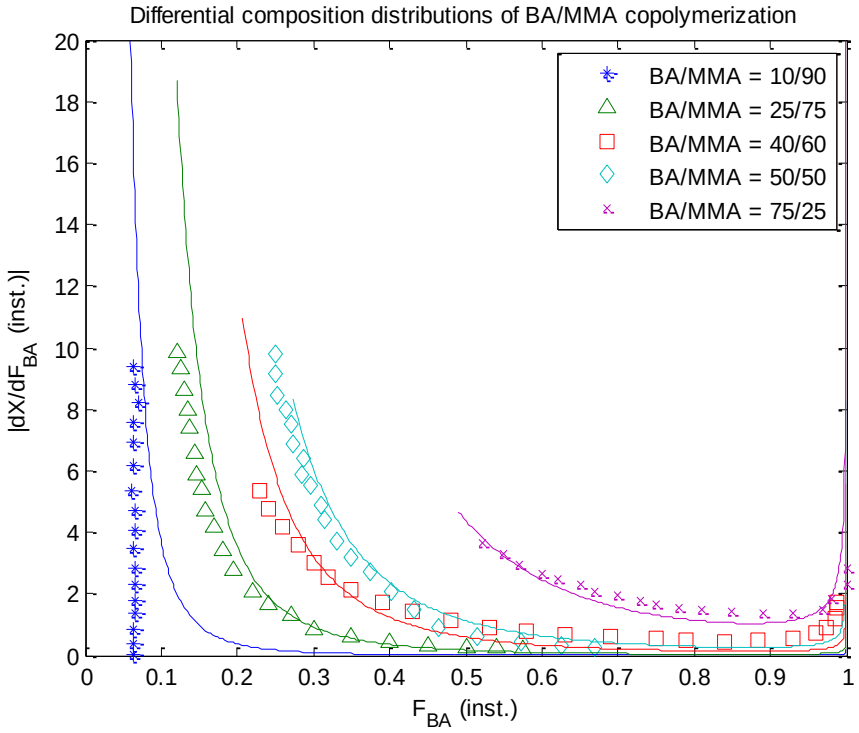

Figure 15. Differential instantaneous *co*-polymer composition distributions of BA in BA/MMA *co*-polymerization
T = 66℃, Butyl acetate (solvent) = 70 wt%, and AIBN = 2 wt% of total mixture

3.7 Sty/AN *Co*-polymerization

Sty/AN *co*-polymers are used as common thermoplastics with good mechanical and chemical properties, and easy to process as well. Sty and AN monomers are also often polymerized with butadiene to produce ABS rubber. In spite of the academic/industrial interest, its full conversion kinetics has been largely unstudied. Garcia-Rubio *et al*. (46) reported reactivity ratio values ($r_{\text{Sty-AN}}$, $r_{\text{AN-Sty}}$) = (0.36, 0.078) along with reliable *co*-polymerization experimental data.

AN monomer exhibits heterogeneous polymerization. In bulk, the polymer precipitates in the reaction medium (monomer) and forms a polymer-rich phase, which makes certain kinetic rate constants different from those in a homogeneous reaction. The complex mechanism of phase separation is not completely understood and this may also affect *co*-polymerization characteristics. Garcia-Rubio *et al*. (46) observed that Sty/AN in bulk is a homogeneous process throughout most of the conversion range when the Sty (monomer 1) initial feed composition is higher than 0.5, hence it was possible to test the multi-component model with experimental data from such an operating region. Figure 16 represents conversion profiles of bulk *co*-polymerizations with f_{Sty0} (f_{10}) from 0.5 to 0.9. Discrepancies start manifesting themselves at Sty content of 70 %.

In Figure 17, model predictions of residual Sty monomer mole fraction follow experimental data acceptably. It should be noted that the azeotropic point ($f_{\text{azeo.}}$) of this system is expected to exist between 0.5 and 0.6, after which the decreasing trend of residual monomer mole fraction starts to reverse in Figure 17. This is an important observation, indicating which monomer is preferentially incorporated into the polymer, determined by reactivity ratios. In this system, Sty monomer is more readily incorporated into the polymer than AN when f_{Sty0} is 0.5, a mole fraction slightly lower than the azeotropic point, and the opposite phenomenon happens at mole fractions higher than the azeotrope. The profiles are expected to level off at the limiting conversion, after which composition will stay constant.

Figure 18 shows the accumulated number-average sequence length of Sty (predictions and experimental data). This plot helps to understand how the Sty/AN microstructure will change throughout the entire conversion. When Sty and AN molar contents are similar in the system, the Sty average sequence length is slightly above one and the chain develops almost like an alternating *co*-polymer (-ABABAB-). As f_{Sty0} increases, the sequence length also increases, especially at high conversion. Then the monomer sequencing patterns resemble those of a block *co*-polymer (-AAABBBAA-). Model trends agree well with experimental data.

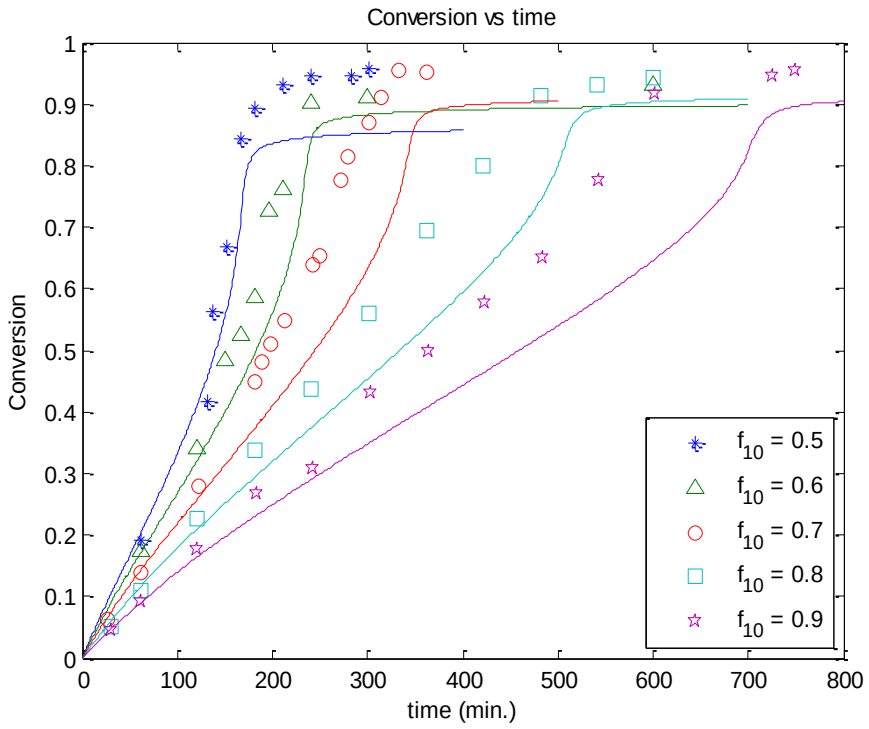

Figure 16. Simulation of bulk *co*-polymerizations of Sty/AN
T = 60℃ and [AIBN]$_0$ = 0.05 M (1 = Sty)

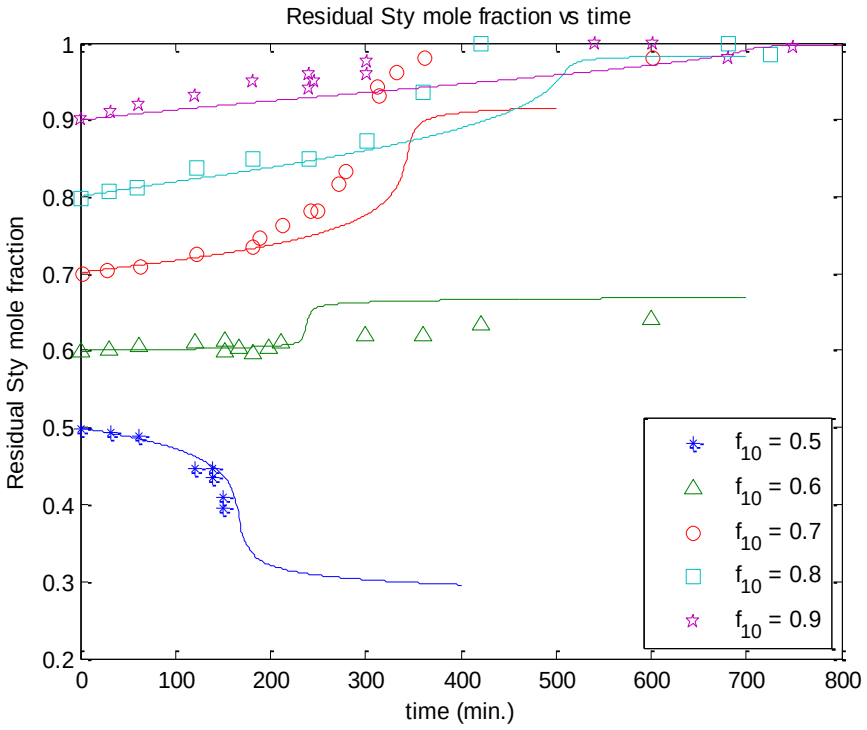

Figure 17. Simulation of residual mole fractions of Sty in Sty/AN *co*-polymerization T = 60℃ and $[AIBN]_0$ = 0.05 M (1 = Sty)

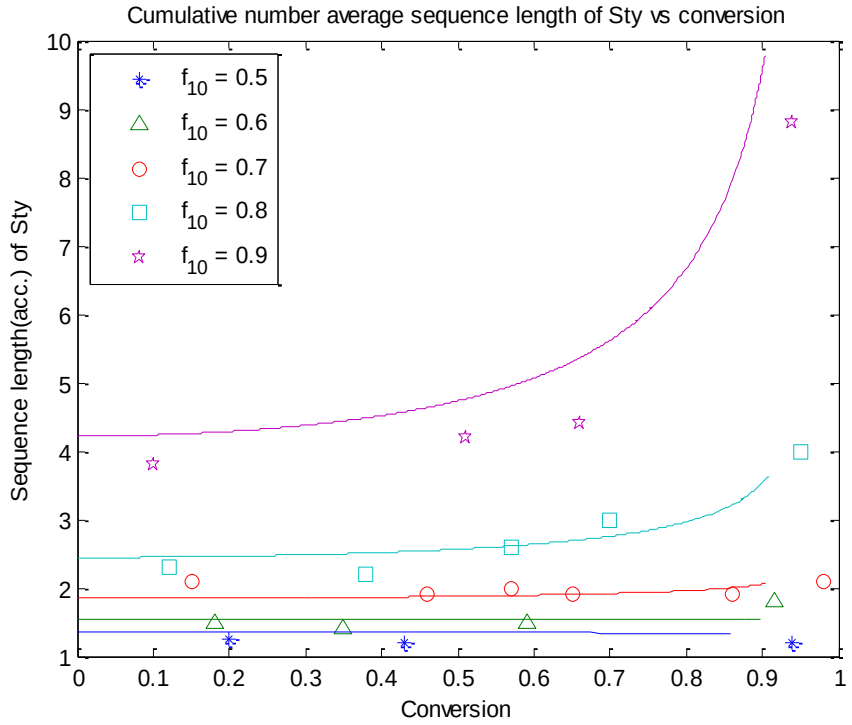

Figure 18. Simulation of accumulated number-average sequence lengths of Sty in Sty/AN *co*-polymerization, T = 60℃ and $[AIBN]_0$ = 0.05 M (1 = Sty)

3.8 Sty/HEA *Co*-polymerization

Sty/HEA full conversion range experiments were conducted by Kim (39). Kinetic studies of any polymerization involving HEA are extremely scarce. HEA polymerization exhibits high molecular weight products through crosslinking reactions by polymerization of divinyl impurities, which are side products in the hydroxylalkyl acrylate polymerization, and transfer to polymer. This leads to difficulties in the analysis of its polymer characteristics.

Some research groups have given approximate estimates for the reactivity ratios of Sty/HEA *co*-polymerization, but the model uses $r_{Sty\text{-}HEA} = 0.254$ and $r_{HEA\text{-}Sty} = 0.279$ from Kim (39), whose kinetic study was more systematic. A 2^3 factorial design was conducted to investigate the effect of temperature (40 and 50℃), initiator concentration ($[AIBN]_0$ = 0.025 and 0.05 mol/L), and initial monomer feed composition ($f_{10} = f_{Sty0} = 0.515$, and 0.840). Representative results are shown in Figures 19 to 21. Some discrepancies are observed at high conversion within otherwise quite satisfactory model trends.

McManus *et al*. (47) conducted not only Sty/HEA *co*-polymerizations (T = 50℃, $[AIBN]_0 = 0.025$ M, and $f_{10} = f_{Sty0} = 0.601$) but also Sty/EA/HEA *ter*-polymerization experiments. Their *co*-polymerization data are plotted along with the data from Kim (39) in Figure 21. Again, the model follows the experimental trends well. Model testing with the *ter*-polymerization experimental data will be discussed later.

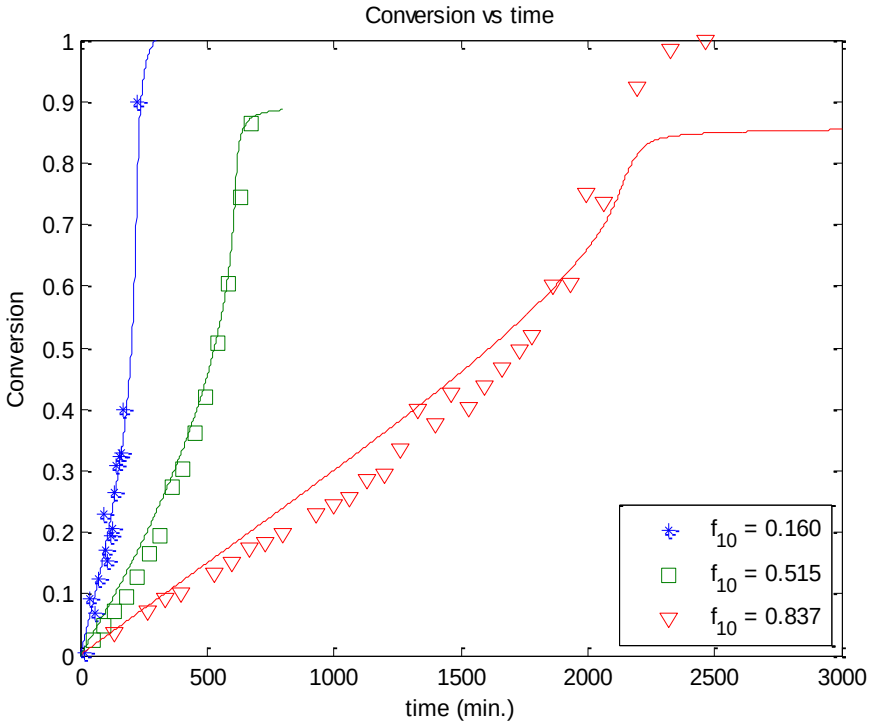

Figure 19. Simulation of Sty/HEA bulk *co*-polymerizations
T = 40℃, $[AIBN]_0$ = 0.05 M (1 = Sty)

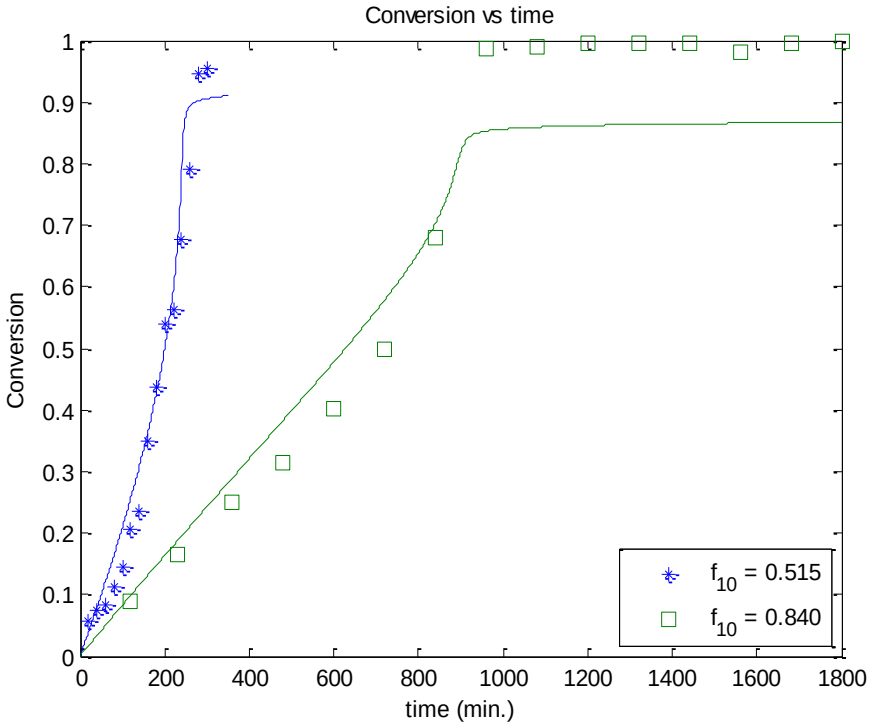

Figure 20. Simulation of Sty/HEA bulk *co*-polymerizations
T = 50℃, $[AIBN]_0$ = 0.05 M (1 = Sty)

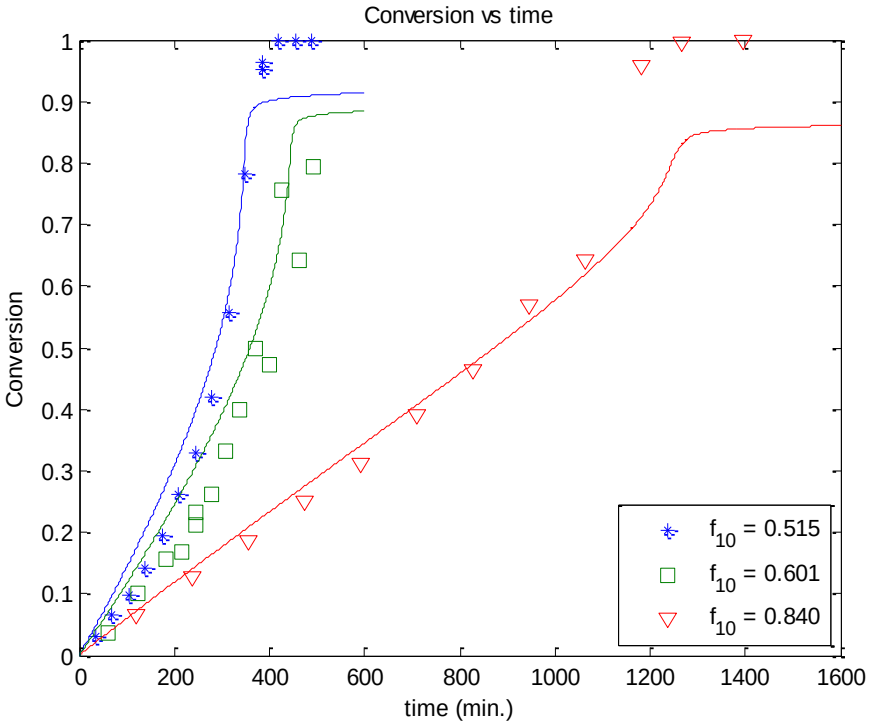

Figure 21. Simulation of Sty/HEA bulk *co*-polymerizations
T = 50℃, $[AIBN]_0$ = 0.025 M (1 = Sty)

3.9 Sty/BA *Co*-polymerization

These two monomers show different polymerization characteristics. Sty *homo*-polymer is hard and tough with a high glass transition temperature (T_g) around 105℃, while BA is flexible and rubbery with low T_g, around -45℃. BA *hom*o-polymerization exhibits its gel effect early with no limiting conversion, whereas Sty *hom*o-polymerization shows the opposite behaviour. Therefore, the overall kinetic behaviour of *co*-polymerization is mainly governed by the dominant monomer in the feed.

Dubé *et al*. (48) investigated Sty/BA *co*-polymerization kinetics and carried out full conversion range experiments under a variety of reaction conditions. The estimated reactivity ratios are $r_{\text{Sty-BA}}$ = 0.956, $r_{\text{BA-Sty}}$ = 0.183. Figures 22 to 24 represent sample simulations of bulk *co*-polymerizations with three initial monomer feed compositions (f_{10} = f_{Sty0} = 0.258, 0.600, and 0.942) at 50℃ and $[\text{AIBN}]_0$ = 0.05 mol/L. In Figure 22, as Sty content becomes more dominant in the monomer feed, the polymerization rate becomes slower. This makes sense since the Sty *homo*-polymerization rate is slower than BA *homo*-polymerization.

Figure 23 shows the average (cumulative or accumulated, acc) composition of Sty monomer in the *co*-polymer ($\overline{\overline{F_{Sty}}}$) throughout the entire conversion. As Sty content increases in the reaction medium, the extent of 'composition drift' is observed to decrease. Looking at the reactivity ratios, the value of $r_{\text{Sty-BA}}$ is almost equal to one, which means that the probability of reaction of a Sty radical with BA monomer is the same as that of a Sty radical with Sty monomer. On the other hand, the low value of $r_{\text{BA-Sty}}$ means that a BA radical prefers Sty monomer over its own monomer. Therefore, it is expected that Sty monomer is incorporated into the polymer at the early stages of the reaction and hence composition values decrease when the Sty monomer feed content (f_{Sty0}) is lower. At f_{Sty0} = 0.942, the cumulative composition does not change since this is the azeotropic composition of the *co*-polymer.

Figure 24 is a simulation of molecular weight averages of the *co*-polymer when f_{Sty} is 0.942. Predictions generally agree with the experimental data satisfactorily. The secondary reaction mechanism of BA monomer (to be discussed later) has again not been considered in this simulation due to the normal (regular) temperature levels employed.

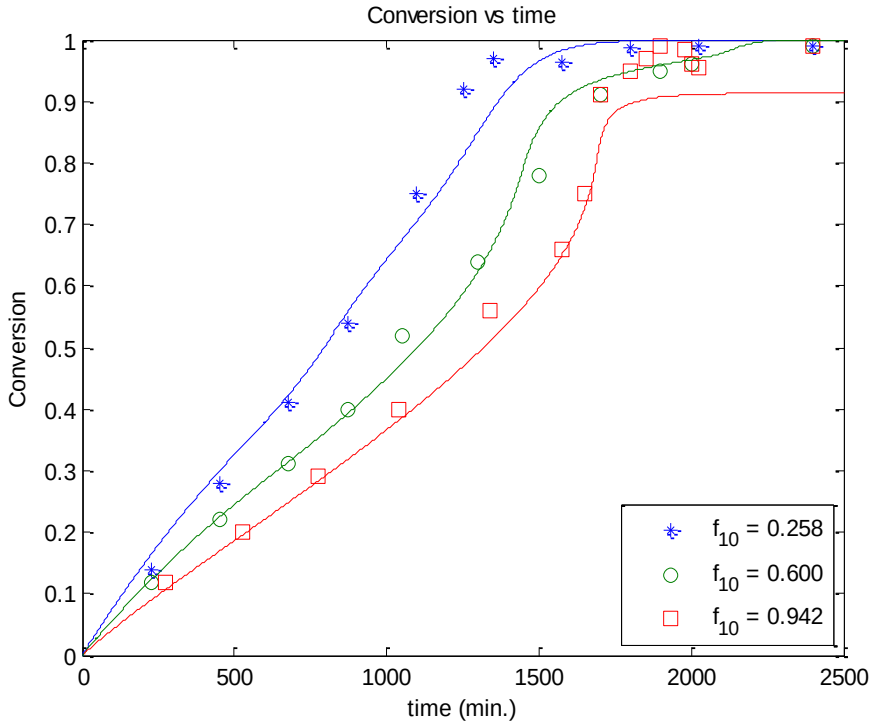

Figure 22. Simulation of bulk *co*-polymerizations of Sty/BA T = 50℃ and $[AIBN]_0$ = 0.05 M (1 = Sty)

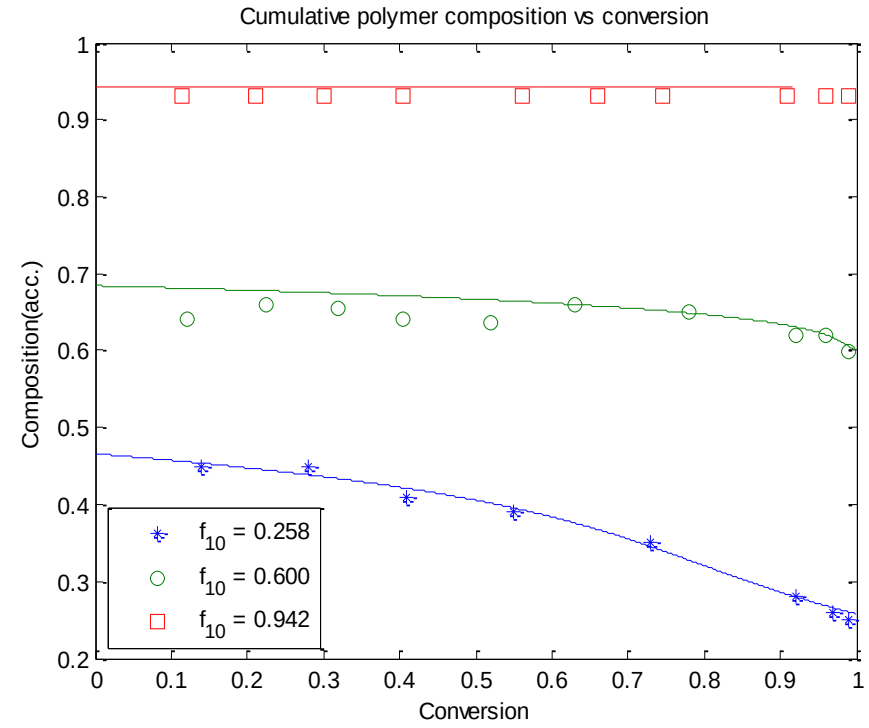

Figure 23. Cumulative polymer compositions of Sty in Sty/BA *co*-polymerization T = 50℃ and $[AIBN]_0$ = 0.05 M (1 = Sty)

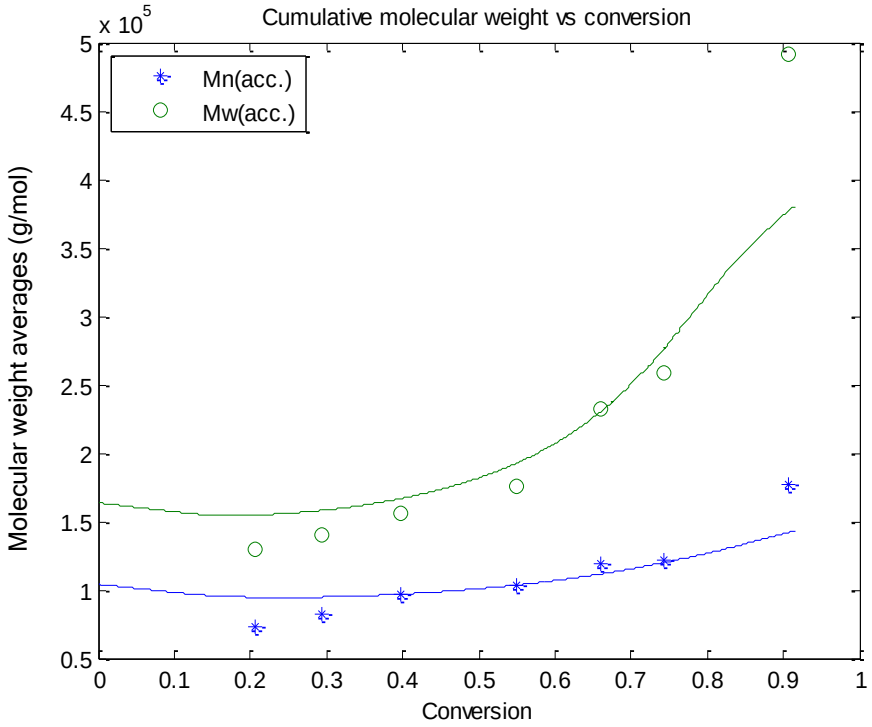

Figure 24. Molecular weight averages of Sty/BA *co*-polymerization T = 50℃, $[AIBN]_0$ = 0.05 M, and f_{Sty0} = 0.942

3.10 Sty/BMA *Co*-polymerization

Model testing of Sty/BMA semi-batch *co*-polymerization at elevated temperatures has been conducted with experimental data from Li *et al*. (21). They used a semi-batch starved-feed policy for the purpose of controlling polymer composition. They used equilibrium monomer concentration information from Bywater (49) to arrive at an expression for the depropagation rate constant of BMA as:

$$k_{dep} = k_p[M]_{eq} = k_p\left(1.76 - 1.37x_{wp}\right) \times 10^6 \times \exp(-6145/T) \qquad (102)$$

$[M]_{eq}$ is the equilibrium concentration of monomer and x_{wp} is the polymer mass fraction in the reactor. Depropagation is assumed to happen only for the radicals ending with a methacrylate unit in the terminal position. The reactivity ratios ($r_{\text{Sty-BMA}}$, $r_{\text{BMA-Sty}}$) = (0.61, 0.42) are from Li *et al*. (21) and the semi-batch feed policy is as follows:

- 215g of xylene solvent charged and heated to 138 ^{0}C; 492g of Sty/BMA monomer mixture (100/0, 75/25, 50/50, 25/75, 0/100 wt%) fed at a fixed rate over 360 min; 13.1 g of *tert*-butyl peroxyacetate initiator (TBPA) fed concurrently with the monomers at a fixed rate over 375 min.

All compositions gave satisfactory model prediction results, and the case of Sty/BMA (75/25 wt%) was chosen as the representative one for the sake of brevity. Figures 25 and 26 show trends of residual concentrations of Sty and BMA, respectively. Due to the semi-batch starved-feeds, the concentrations are rising to certain levels at the early stage of reaction, falling gradually in the aftermath. Figure 27 is the cumulative polymer composition vs. time plot. The composition profiles remain almost constant and therefore, 'composition drift' is eliminated during the entire reaction. This is because depropagation steps essentially counterbalance composition drift, despite the fact that the BMA propagation rate constant is more than twice higher (faster) than that of Sty. The combined effect of depropagation and high temperature results in low weight-average molecular weights, as shown in Figure 28.

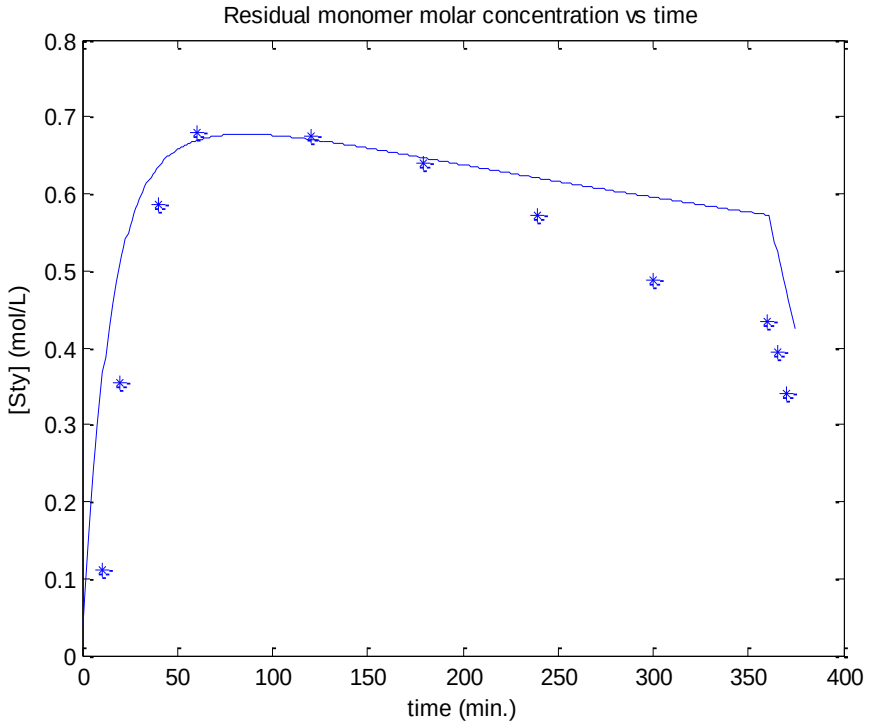

Figure 25. Residual monomer concentration of Sty in *co*-polymerization of Sty/BMA (75/25 wt%) according to the semi-batch policy

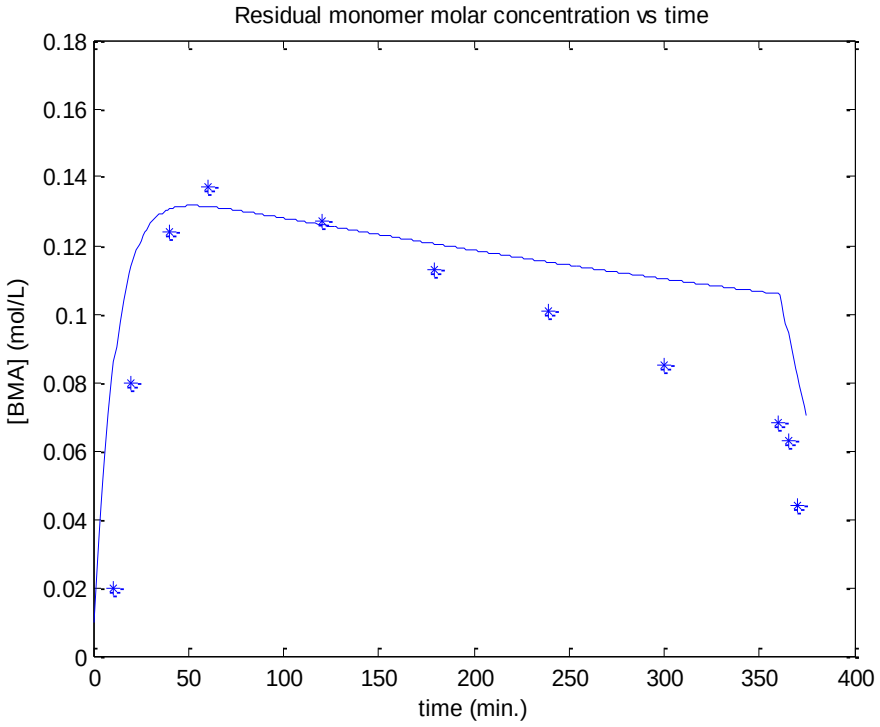

Figure 26. Residual monomer concentration of BMA in *co*-polymerization of Sty/BMA (75/25 wt%) according to the semi-batch policy

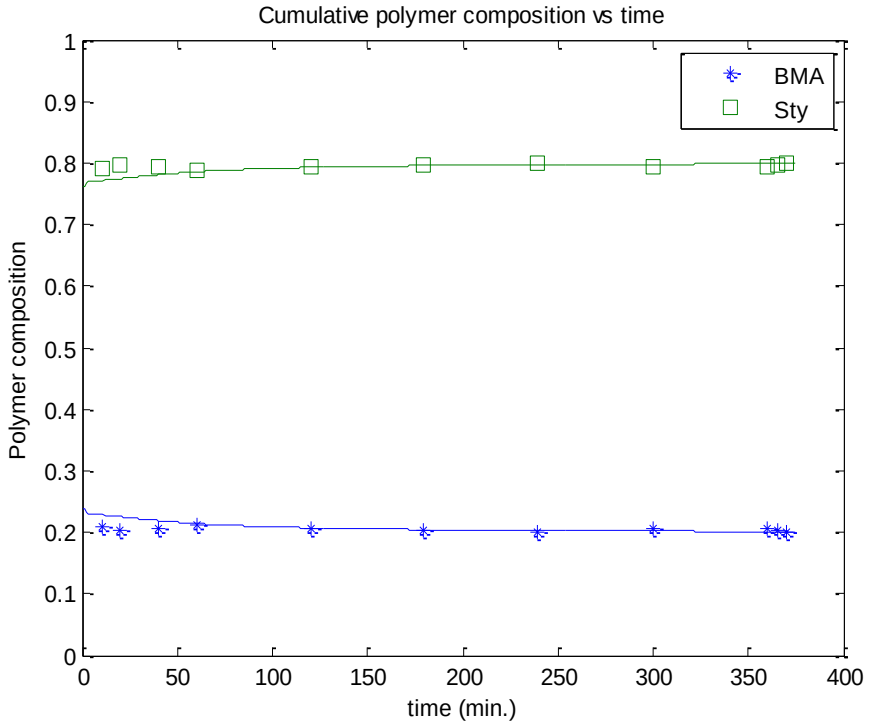

Figure 27. Cumulative polymer composition vs. time in *co*-polymerization of Sty/BMA (75/25 wt%) according to the semi-batch policy

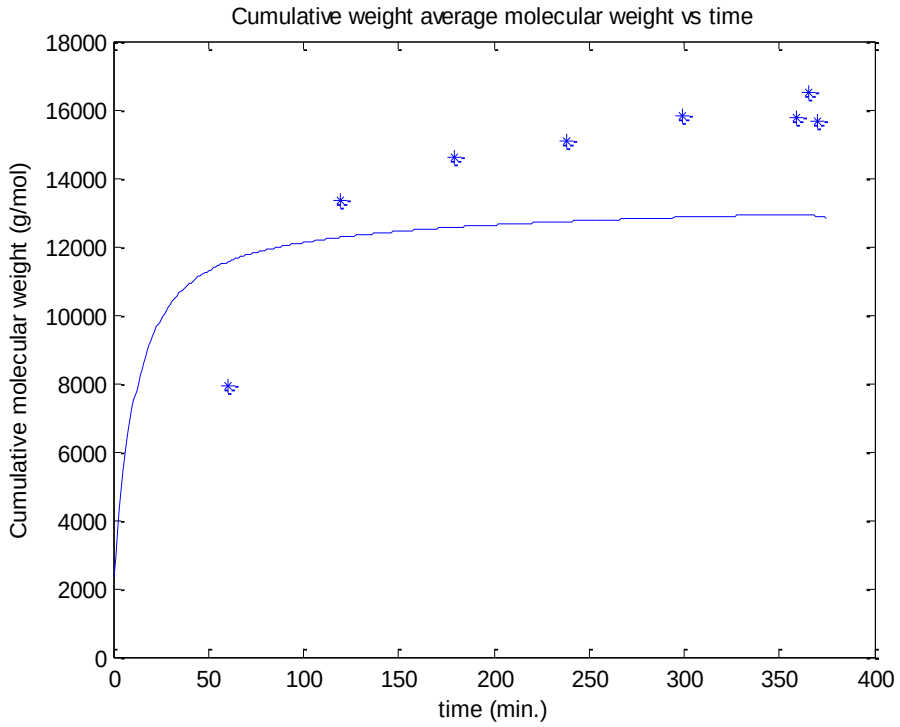

Figure 28. Weight-average molecular weight vs. time in *co*-polymerization of Sty/BMA (75/25 wt%) according to the semi-batch policy

3.11 AMS/MMA *Co*-polymerization

In Figures 29 and 30, the instantaneous polymer composition trends of AMS in AMS/MMA using the Mayo-Lewis and Krüger model predictions are compared with experimental data from Martinet and Guillot (50) for 60 and 80℃. The equilibrium constant of AMS and reactivity ratios at each temperature are as follows:

$$K_{eq,AMS} = \frac{\overline{k_{p11}}}{k_{p11}} = 7.1\text{, } (r_{\text{AMS-MMA}}, r_{\text{MMA-AMS}}) = (0.734, 0.548) \text{ at } 60℃$$

$$K_{eq,AMS} = \frac{\overline{k_{p11}}}{k_{p11}} = 12.9\text{, } (r_{\text{AMS-MMA}}, r_{\text{MMA-AMS}}) = (0.417, 0.516) \text{ at } 80℃$$

Due to the low ceiling temperature of AMS (61℃), depropagation becomes dominant as the reaction temperature and AMS feed ratio increase. When f_{AMS} is greater than 0.5, the Mayo-Lewis model assuming no depropagation does not hold any longer. Instead, the behaviour of polymer composition F_{AMS} is explained by Krüger's model very well at both temperature levels.

The depropagation batch model prediction trends are compared with full conversion experimental data by Palmer *et al*. (14) regarding conversion (Figure 31), cumulative polymer composition (Figure 32), and molecular weight averages (Figure 33), obtained at 140℃, with 2 wt% of *di-tert*-butyl peroxide (DTBP) initiator, and AMS/MMA = 45/55 wt% in the monomer feed. At this temperature, MMA also depropagates, with the depropagation parameters as listed below (1 = AMS, 2 = MMA):

$$K_{eq,AMS} = \frac{\overline{k_{p11}}}{k_{p11}} = 54\text{, } K_{eq,MMA} = \frac{\overline{k_{p22}}}{k_{p22}} = 0.45\text{, } \frac{\overline{k_{p12}}}{k_{p21}} = 1.388\text{, } \frac{\overline{k_{p21}}}{k_{p12}} = 24.96\text{,}$$

$$(r_{\text{AMS-MMA}}, r_{\text{MMA-AMS}}) = (0.003, 0.42) \text{ at } 140℃$$

A conversion limit is observed under 65% in Figure 31 due to significant depropagation (especially by AMS). Figures 32 and 33 show additional snapshots of the depropagation effects. The reactivity ratio $r_{\text{AMS-MMA}}$ is 0.003, which leads to a low average polymer composition for AMS (around 15%) in Figure 32. Also, in Figure 33, low molecular

weights are obtained. In spite of slight discrepancies from experimental data, the trends look very satisfactory.

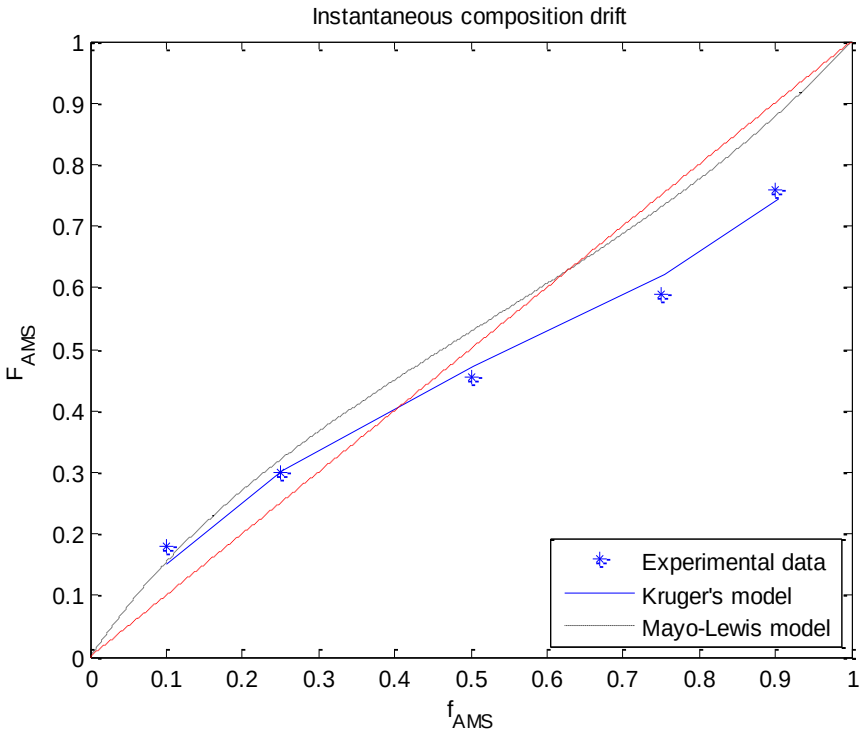

Figure 29. Composition F_{AMS} in AMS/MMA bulk *co*-polymerization T = 60℃ and AIBN = 0.5 mol%

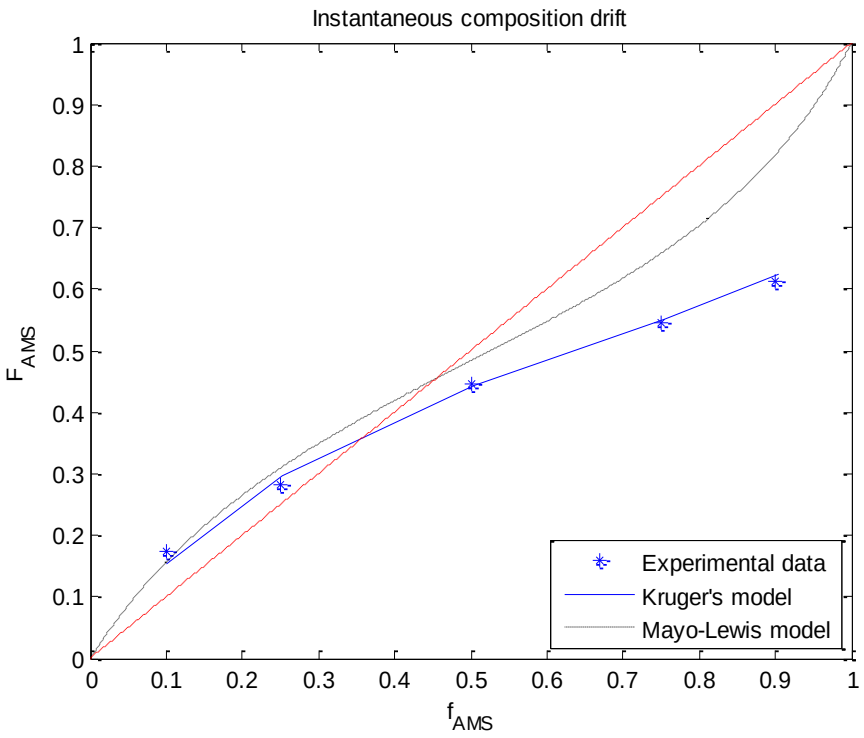

Figure 30. Composition F_{AMS} in AMS/MMA bulk *co*-polymerization T = 80℃ and AIBN = 0.5 mol%

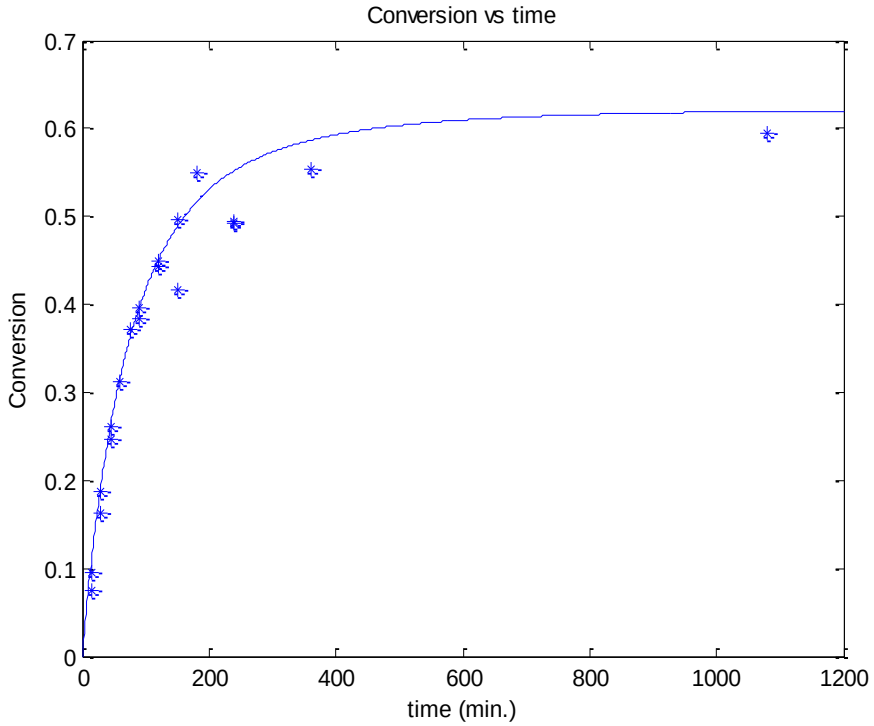

Figure 31. Simulation of AMS/MMA (45/55 wt%) bulk *co*-polymerization T = 140℃ and DTBP = 2 wt%

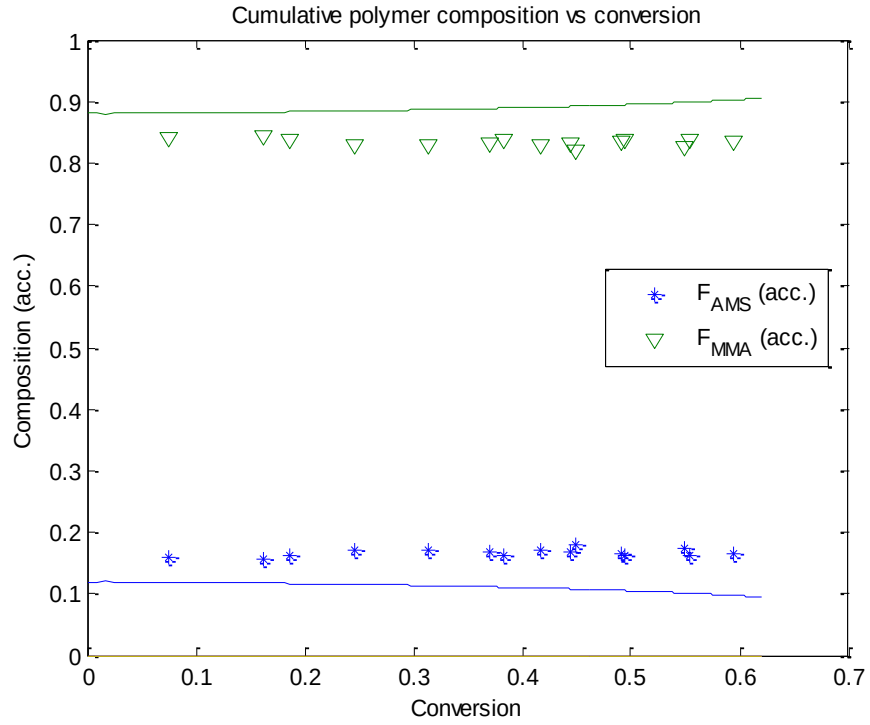

Figure 32. Cumulative polymer compositions of AMS and MMA in AMS/MMA (45/55 wt%) *co*-polymerization T = 140℃ and DTBP = 2 wt%

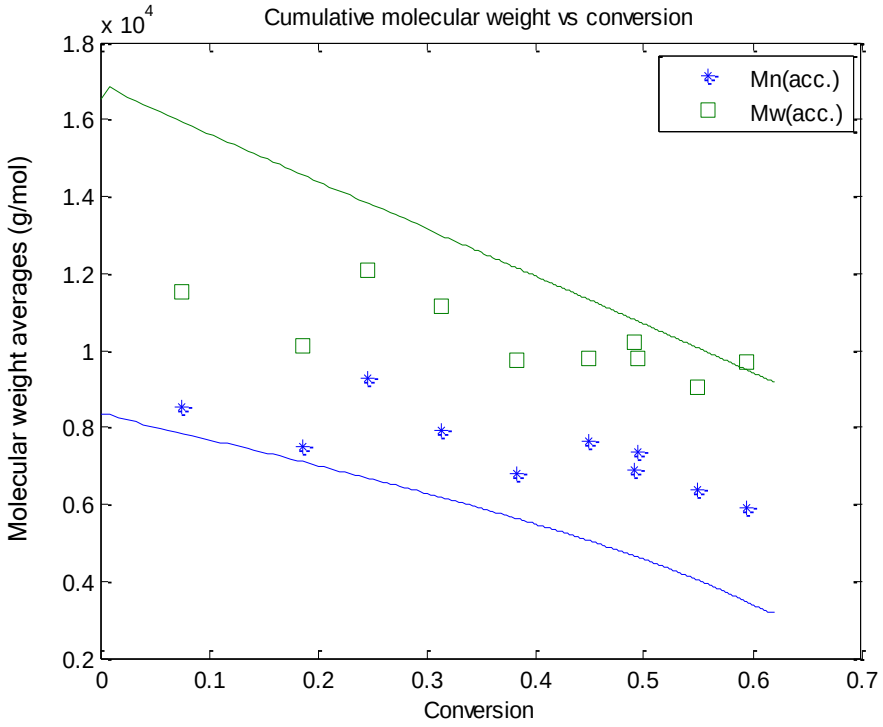

Figure 33. Molecular weight averages of AMS/MMA (45/55 wt%) *co*-polymerization T = 140℃ and DTBP = 2 wt%

3.12 MMA/BA/VAc *Ter*-polymerization

The simulations of *ter*- and higher multi-component polymerizations can be obtained by utilizing the existing *homo*- and *co*-polymerization database without any additional changes thanks to the pseudo-rate constant method. For instance, in this *ter*-polymerization case, all model predictions are based on the same database as for *homo*- and *co*-polymerizations of BA, MMA, and VAc. Dubé and Penlidis (51) conducted factorial design experiments over the full conversion range for bulk *ter*-polymerizations at T = 50 and 70℃, and $[AIBN]_0$ = 0.01 and 0.071 mol/L, for 30/30/40 wt% of BA/MMA/VAc initial monomer feed ratio.

Examining Figures 34 and 35 (Figure 36 will be discussed shortly), the polymerization behaviour can be divided into two stages. The rate is more or less constant up to about 60% conversion (first stage), after which it shows a dramatic increase (second stage). A 'double rate phenomenon' is observed. The corresponding *ter*-polymer composition plots in Figures 37 and 38, and average molecular weight plots in Figures 39 and 40, also corroborate the "double rate" phenomenon and the model satisfactorily describes the overall behaviour.

Dubé and Penlidis (51) reported that the samples taken out at higher conversions during the experiment at 70℃ contained a solid core surrounded by a lower viscosity liquid, and a feasible explanation was given in that non-isothermal behaviour had occurred. This points to possible discrepancies between (isothermal) model predictions and (non-isothermal) experimental data at mid- and high conversion levels, as shown in Figure 35 ($[AIBN]_0$ = 0.01 mol/L case). However, if one employs the actual non-isothermal profile (which is what really happened in this case), then one can obtain very good agreement, as shown in Figure 36. This is another example of the benefits of using a mathematical model, with respect to troubleshooting process behaviour. At first glance, if a discrepancy exists between experimental data and model predictions, the natural tendency is to fault the model. This case is indeed a counter-example, where actually the model is doing very well if fed the appropriate input information.

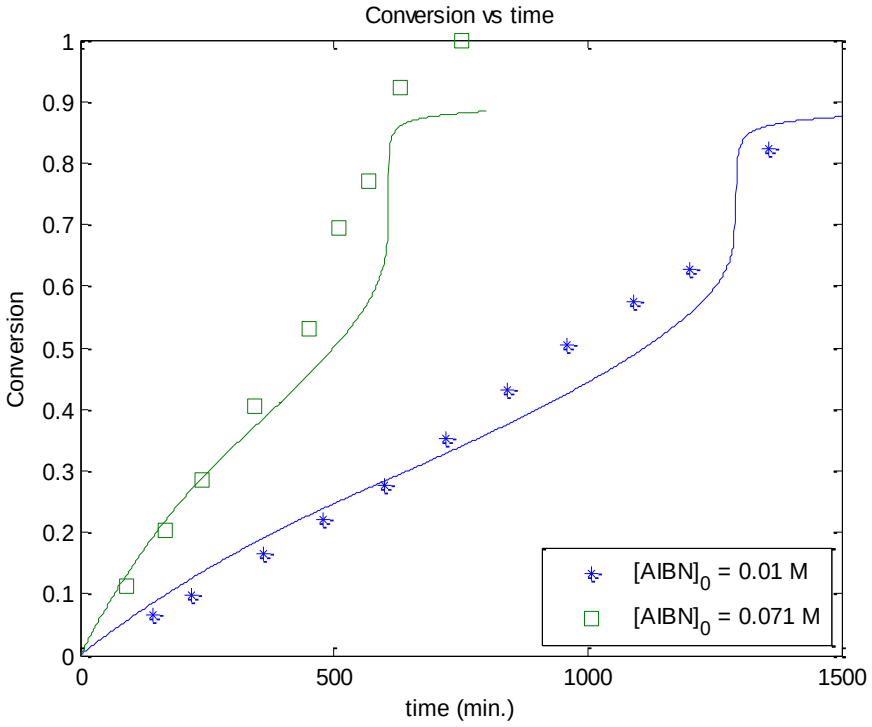

Figure 34. Simulation of bulk *ter*-polymerizations of BA/MMA/VAc T = 50℃ and (BA/MMA/VAc) = (30/30/40 wt%)

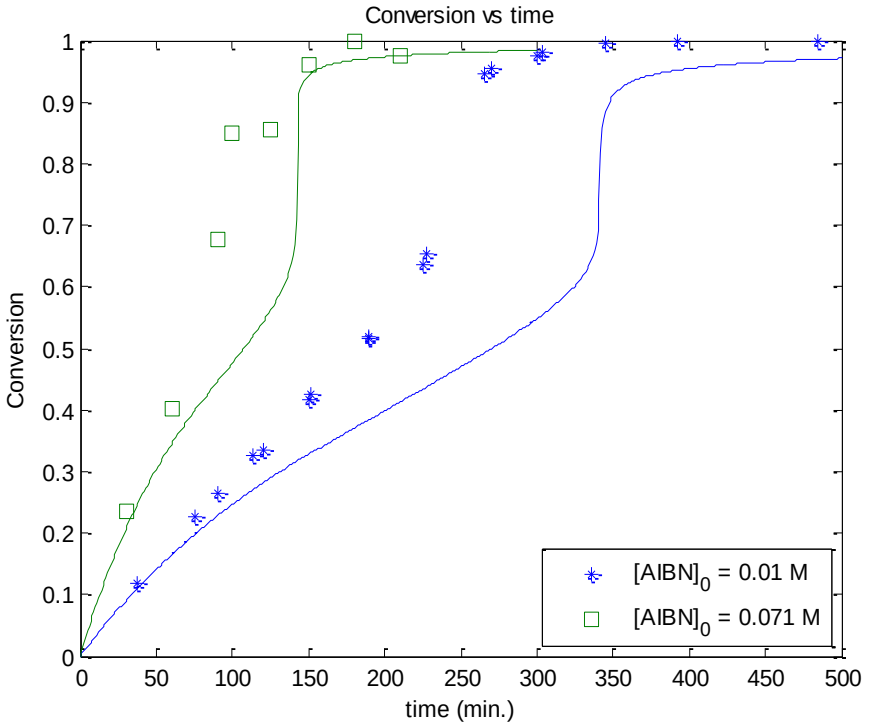

Figure 35. Simulation of bulk *ter*-polymerizations of BA/MMA/VAc T = 70℃ and (BA/MMA/VAc) = (30/30/40 wt%)

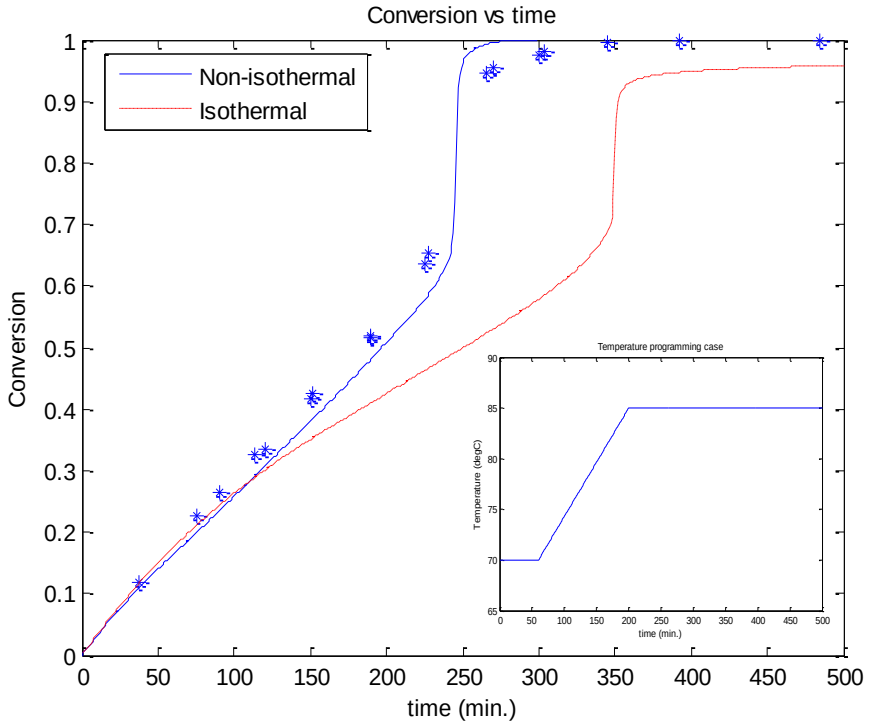

Figure 36. Simulation of bulk *ter*-polymerization of BA/MMA/VAc $[AIBN]_0$ = 0.01 M, (BA/MMA/VAc) = (30/30/40 wt%), non-isothermal profile

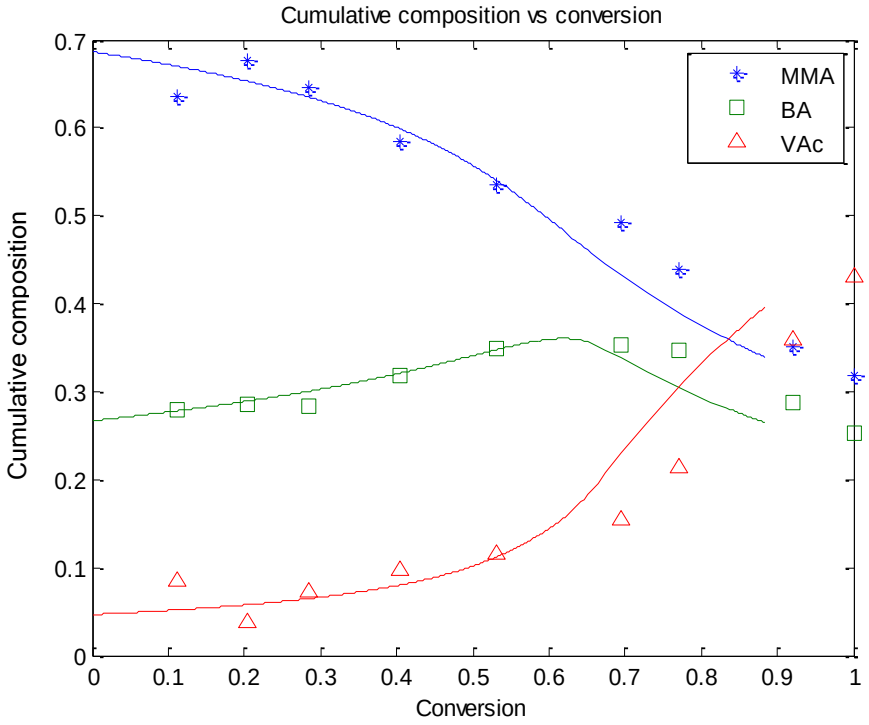

Figure 37. Cumulative polymer composition in BA/MMA/VAc *ter*-polymerization T = 50℃, $[AIBN]_0$ = 0.071 M, and (BA/MMA/VAc) = (30/30/40 wt%)

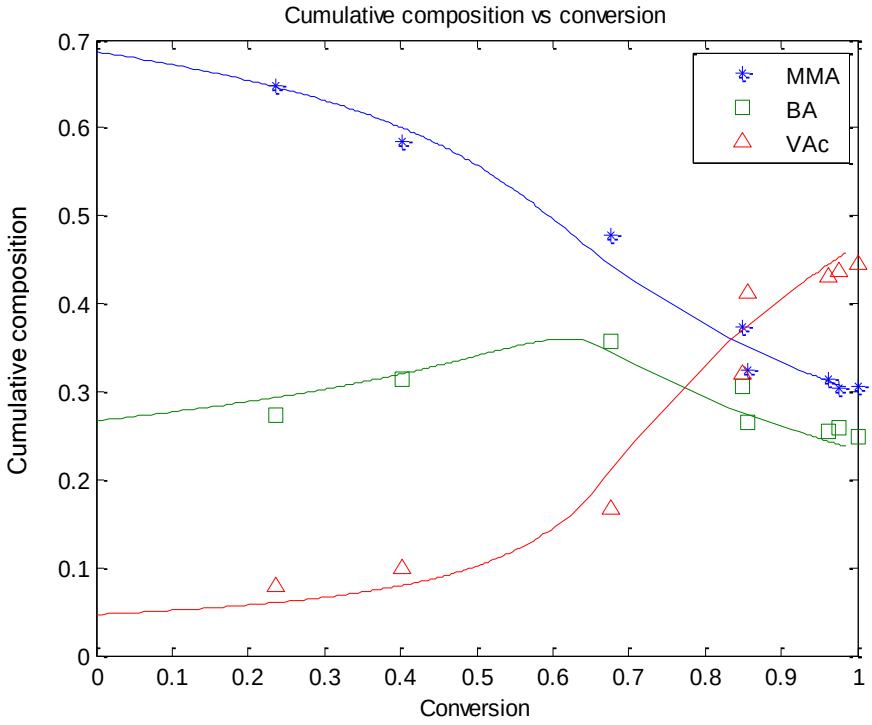

Figure 38. Cumulative polymer composition in BA/MMA/VAc *ter*-polymerization T = 70℃, $[AIBN]_0$ = 0.071 M, and (BA/MMA/VAc) = (30/30/40 wt%)

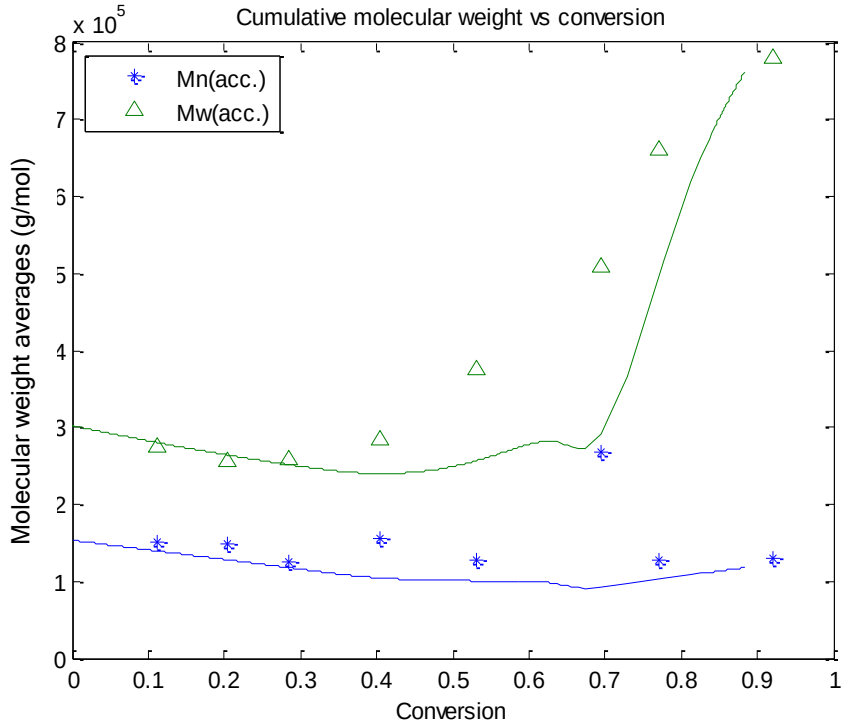

Figure 39. Molecular weight averages of BA/MMA/VAc *ter*-polymerization T = 50℃, $[AIBN]_0$ = 0.071 M, and (BA/MMA/VAc) = (30/30/40 wt%)

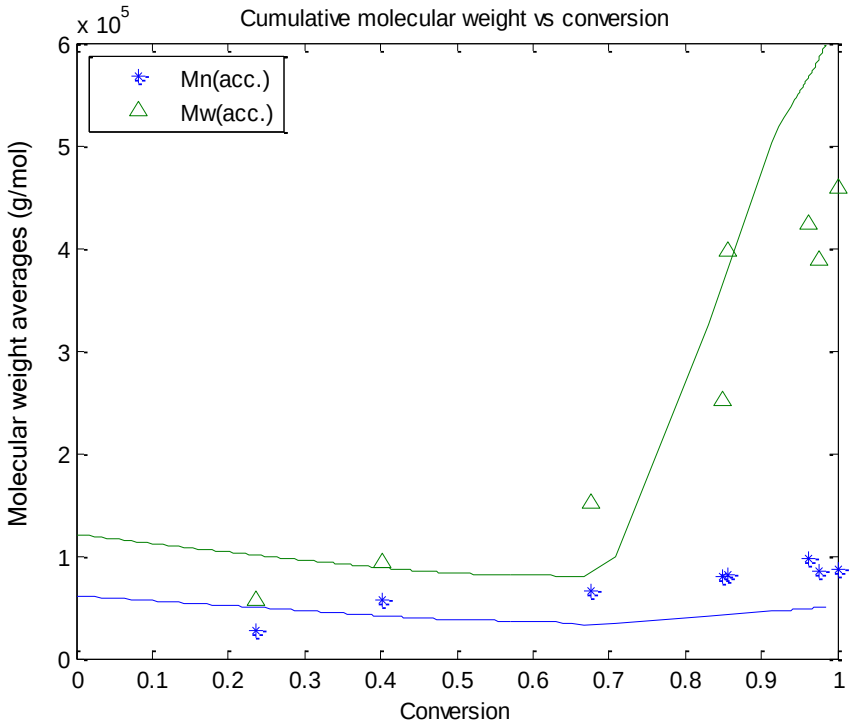

Figure 40. Molecular weight averages of BA/MMA/VAc *ter*-polymerization T = 70℃, $[AIBN]_0$ = 0.071 M, and (BA/MMA/VAc) = (30/30/40 wt%)

3.13 Sty/EA/HEA *Ter*-polymerization

Sty/EA/HEA and Sty/EA/MAA *ter*-polymers are used in the paint and surface coatings industry. McManus *et al*. (47) performed Sty/EA/HEA bulk *ter*-polymerizations at 60℃, $[AIBN]_0$ = 0.05 mol/L and two levels of initial monomer feed ratios (Sty/EA/HEA = 50/45/5 wt% and 50/40/10 wt%). Experiments were limited to maintaining a low HEA level because it was difficult to isolate residual HEA monomer from the polymer when the feed mole fraction of HEA was greater than 0.5, as this would have increased the experimental error. Figure 41 represents model predictions and experimental data, which agree with each other. As HEA content increases, polymerization rate increases.

The system was studied in (52) at elevated temperatures, starting with Sty/EA *co*-polymerization and extending it to Sty/EA/HEA/MAA solution *tetra*-polymerization. A 2^2 factorial design was performed to test the effect of temperature (100 and 130℃) and the presence of 0.5 wt% chain transfer agent (octanethiol). The feed composition ratio was Sty/EA/HEA = 42/42/16 wt%, *tert*-butyl peroxybenzoate (TBPB) initiator was used at 1.5 wt% of the total monomer mixture, as well as *m*-xylene solvent at 60 wt% of the total reaction mixture. The reactivity ratios estimated at elevated temperatures were ($r_{Sty\text{-}EA}$, $r_{EA\text{-}Sty}$) = (0.8996, 0.2083), ($r_{Sty\text{-}HEA}$, $r_{HEA\text{-}Sty}$) = (0.5527, 0.2347), and ($r_{EA\text{-}HEA}$, $r_{HEA\text{-}EA}$) = (0.7498, 2.2361) at 100℃; and ($r_{Sty\text{-}EA}$, $r_{EA\text{-}Sty}$) = (0.9305, 0.1996), ($r_{Sty\text{-}HEA}$, $r_{HEA\text{-}Sty}$) = (0.6193, 0.2408), and ($r_{EA\text{-}HEA}$, $r_{HEA\text{-}EA}$) = (0.6517, 1.4214) at 130℃.

In Figure 42, model predictions show good agreement with conversion experimental data and CTA effects are negligible on reaction rate. As expected, the reaction rate becomes faster as temperature increases. However, significant discrepancies were observed with respect to *ter*-polymer composition, as shown in Figure 43. These discrepancies are due to significant experimental error resulting from the highly branched and/or crosslinked polymer chains, as this would definitely affect *ter*-polymer composition characterized by solution ^{1}H-NMR.

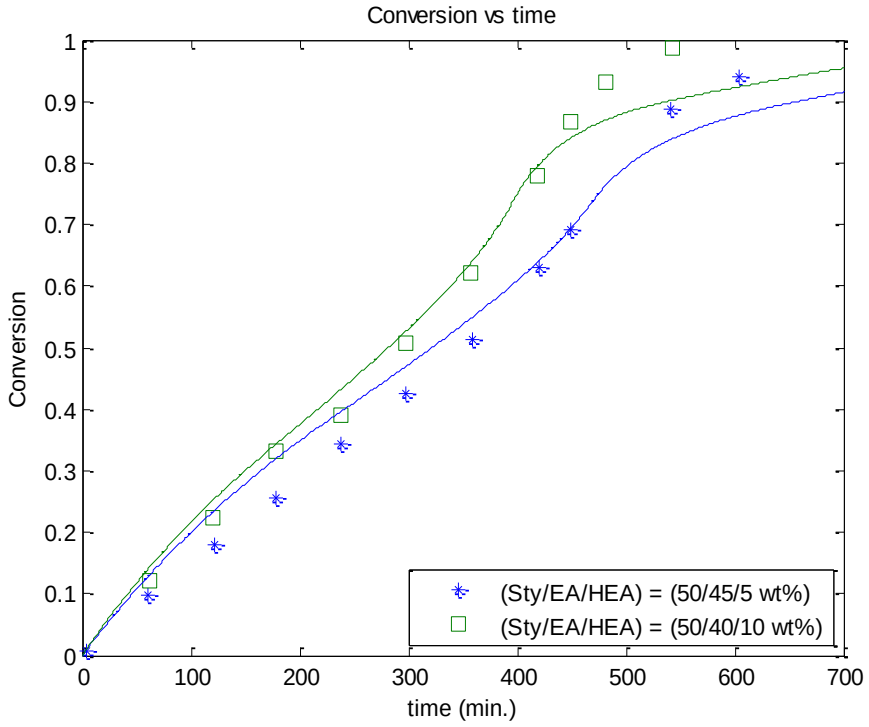

Figure 41. Simulation of bulk *ter*-polymerizations of Sty/EA/HEA T = 60℃ and $[AIBN]_0$ = 0.05 M

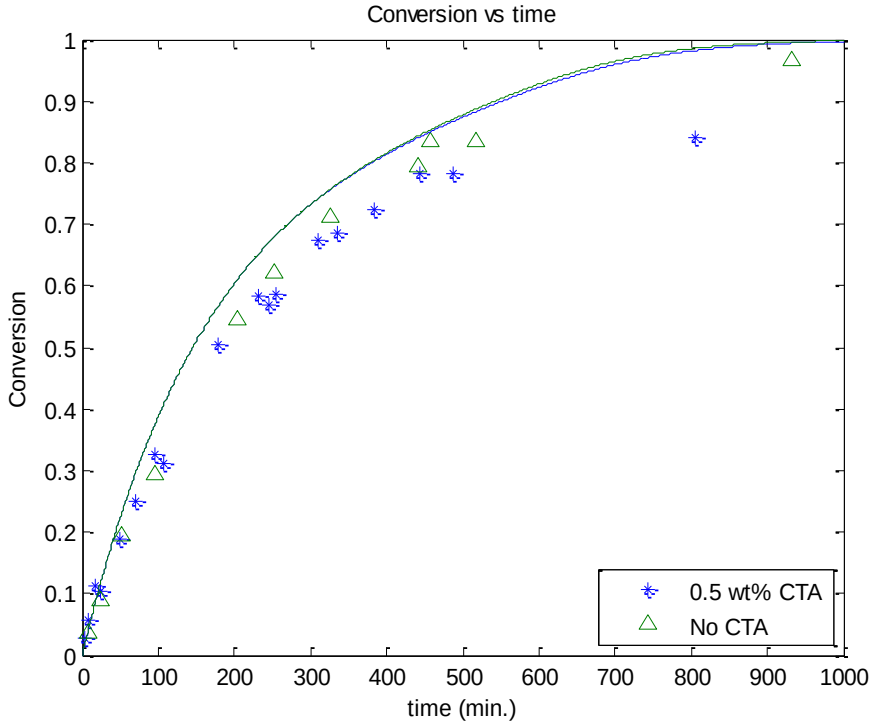

Figure 42. Simulation of solution *ter*-polymerization of Sty/EA/HEA (42/42/16 wt%) T = 100℃, *m*-xylene = 60 wt% of total mixture, and TBPB = 1.5 wt% of total monomer

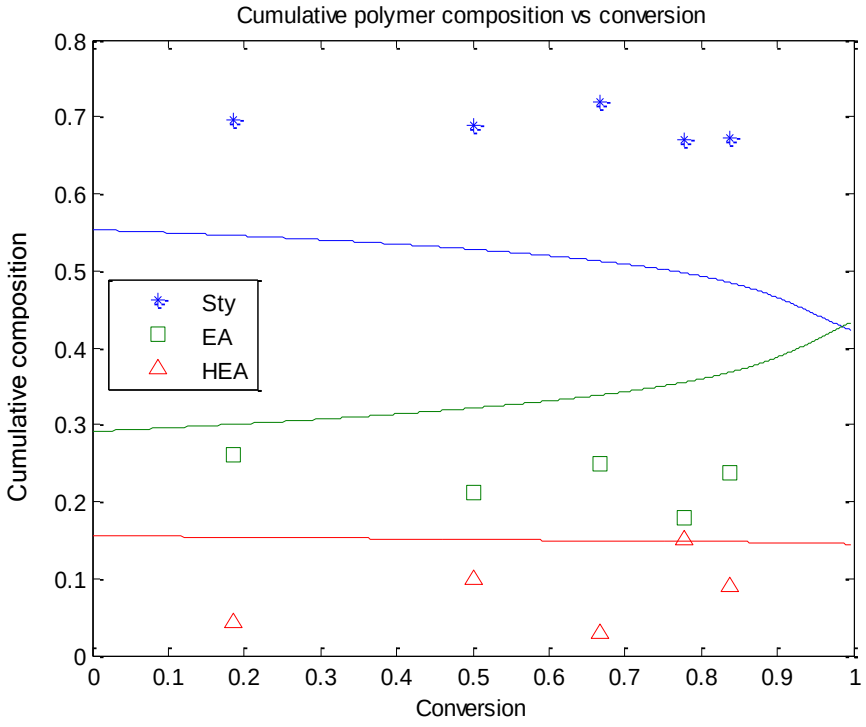

Figure 43. Polymer composition in Sty/EA/HEA (42/42/16 wt%) *ter*-polymerization
T = 100℃, *m*-xylene = 60 wt% of total mixture
octanethiol = 0.5 wt% and TBPB = 1.5 wt% of total monomer

3.14 AMS/MMA/BA *Ter*-polymerization

The depropagation model testing was extended next to AMS/MMA/BA bulk *ter*-polymerization. From *ter*-polymer composition measurements via ^{13}C-NMR, Leamen *et al*. (18) could obtain kinetic parameters at 140℃ as follows (1 = AMS, 2 = MMA, 3 = BA):

$$\frac{\overline{k}_{p11}}{k_{p13}} = 33, \quad \frac{\overline{k}_{p21}}{k_{p12}} = 14.041, \quad \frac{\overline{k}_{p12}}{k_{p21}} = 4.0401, \quad \frac{\overline{k}_{p13}}{k_{p31}} = 1.4629, \quad \frac{\overline{k}_{p31}}{k_{p13}} = 0.50796$$

(r_{12}, r_{21}) = (0.35956, 0.70698), (r_{13}, r_{31}) = (0.5575, 0.14299), (r_{23}, r_{32}) = (1.905, 0.34841)

Figure 44 compares instantaneous polymer composition vs. monomer feed composition of AMS/MMA/BA experimental data with model predictions generated by the multi-component model with the depropagation feature. The comparison is satisfactory. The model has also been tested with the full conversion experimental data (AMS/MMA/BA = 45/45/10 wt%, 140℃, 0.5 wt% of DTBP initiator) from McManus *et al*. (53) and reasonable trends were obtained (note that the recipe is similar to the AMS/MMA *co*-polymerization case). Figure 45 shows the molar conversion curve; the final conversion attained was close to 70% due to the severe depropagation of AMS at 140℃. AMS will incorporate into the polymer only via *cross*-propagation with MMA or BA (refer to the above depropagation parameters). Therefore, the low polymer composition of AMS in Figure 46 is obviously reasonable because the produced *ter*-polymer would be mainly composed of the other two monomers, MMA and BA.

The number-/weight-average molecular weights of AMS/MMA/BA *ter*-polymer in Figure 47 are measured around 20,000 g/mol. Comparing to the molecular weight averages of AMS/MMA *co*-polymer in Figure 33 (around 10,000 g/mol) at the same temperature level, this is due to the different amount of DTBP initiator (0.5 and 2 wt% in *ter*- and *co*-polymerization, respectively).

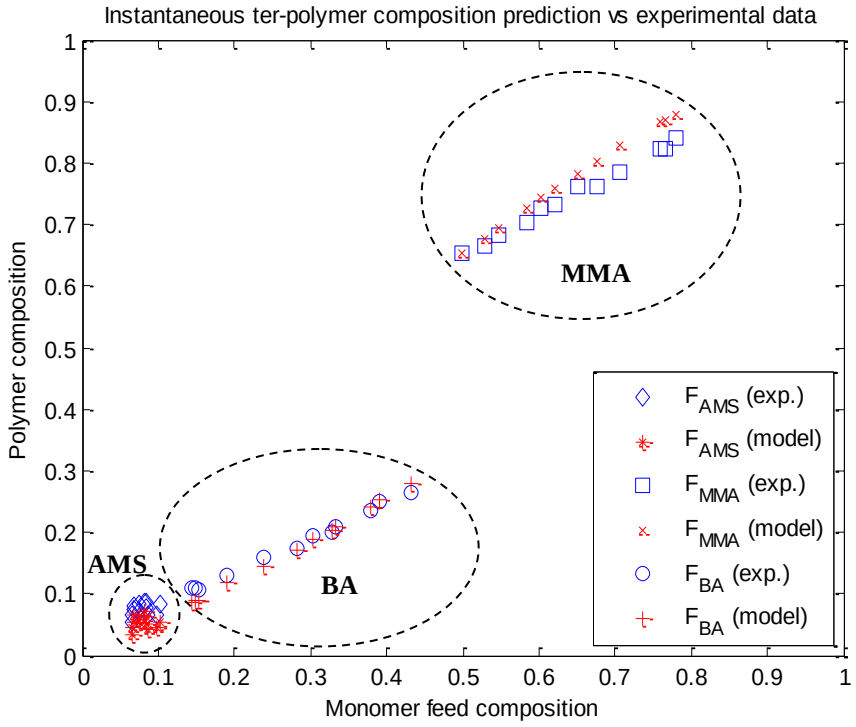

Figure 44. Composition predictions vs. experimental data of AMS/MMA/BA *ter*-polymerization, T = 140℃

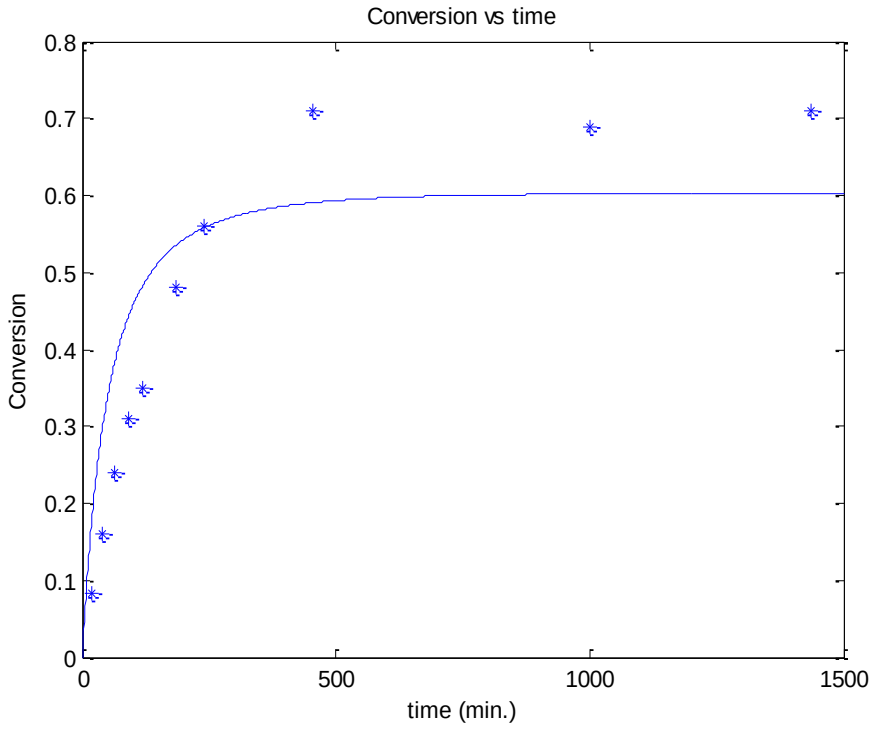

Figure 45. Simulation of AMS/MMA/BA (45/45/10 wt%) bulk *ter*-polymerization T = 140℃ and DTBP = 0.5 wt%

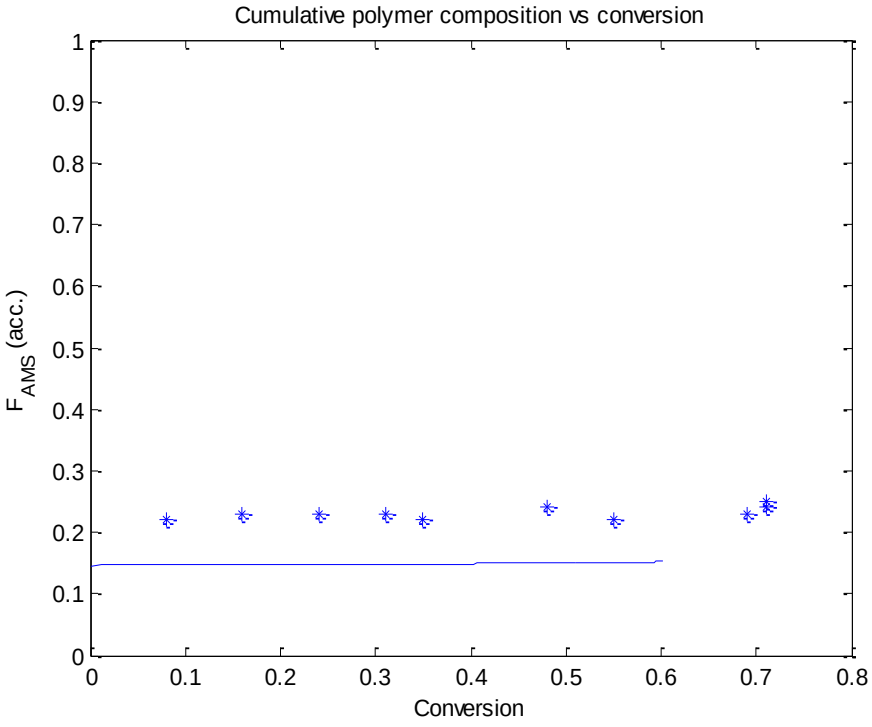

Figure 46. Polymer composition of AMS in AMS/MMA/BA (45/45/10 wt%) *ter*-polymerization, T = 140℃ and DTBP = 0.5 wt%

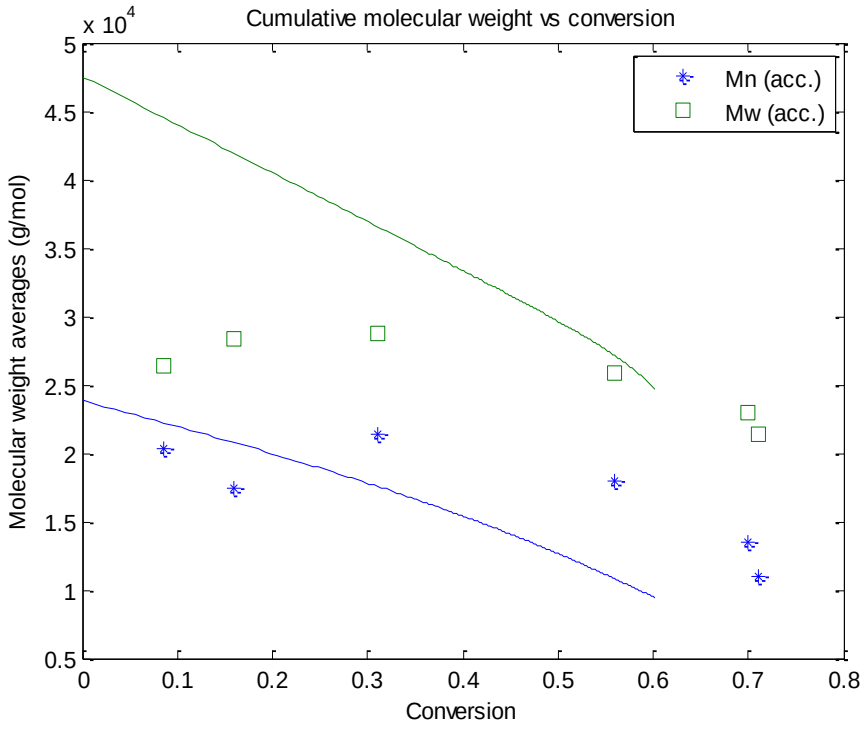

Figure 47. Molecular weight averages of AMS/MMA/BA (45/45/10 wt%) *ter*-polymerization T = 140℃ and DTBP = 0.5 wt%

3.15 Sty/EA/HEA/MAA *Tetra*-polymerization

This monomer system represents the highest degree of multi-component polymerization model testing that has been found so far with available experimental data. Solution polymerizations were conducted in (52) using 2^3 factorial design experiments. *m*-xylene was used as solvent with two levels of temperature (100 and 130℃), octanethiol as the CTA and *tert*-butyl peroxybenzoate (TBPB) as the initiator. The feed composition was set at (Sty/EA/HEA/MAA) = (41/41/16/2 wt%) and the amounts of solvent, CTA, and initiator were 60 wt%, 0.5 wt%, and 1.5 wt% of the total reaction mixture, respectively. Extra monomer feed compositions were further utilized, such as (Sty/EA/HEA/MAA) = (42/42/14/2, 42/42/11/5, and 39.5/39.5/16/5 wt%).

Figure 48 is a conversion plot at 100℃, with or without CTA. The CTA effect is not significant on polymerization rate. In the cumulative polymer composition plots (Figures 49 and 50), it is clear that temperature and CTA effects are negligible. Model prediction trends are similar to the ones of the experimental data but discrepancies are observed in actual levels. *Tetra*-polymer samples contained gel and were not completely dissolved during NMR analysis, as reported in (52). This acted as a source of error in both composition calculations (scattered points) and reactivity ratio estimation.

Finally, Figure 51 shows conversion profiles from additional experiments (change of monomer feed composition). There are almost no differences among polymerization rates and the model predictions are satisfactory.

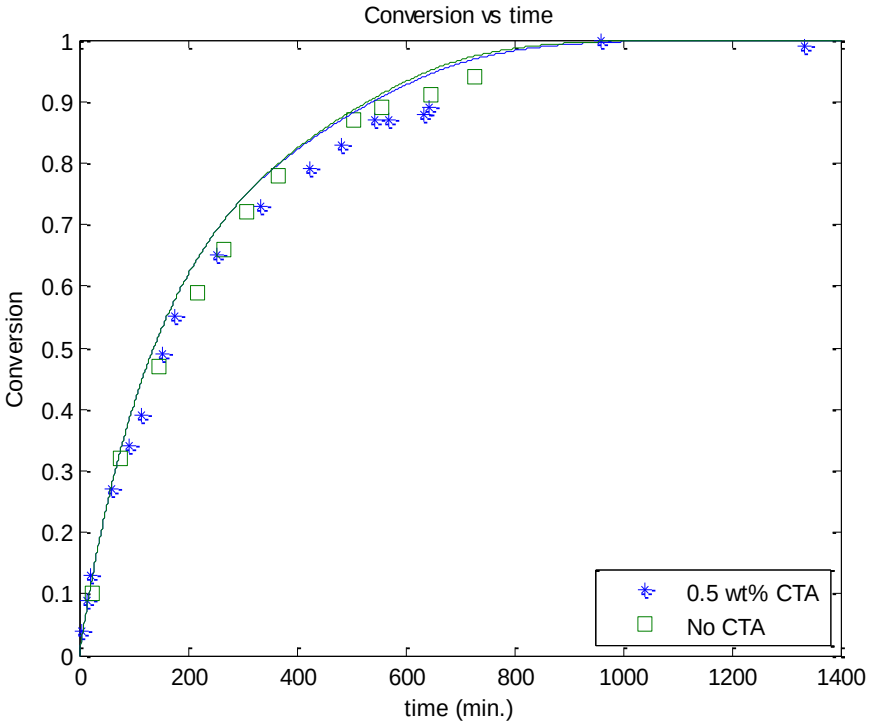

Figure 48. Solution *tetra*-polymerization of Sty/EA/HEA/MAA (41/41/16/2 wt%) T = 100℃, *m*-xylene = 60 wt% of total mixture, and TBPB = 1.5 wt% of total monomer

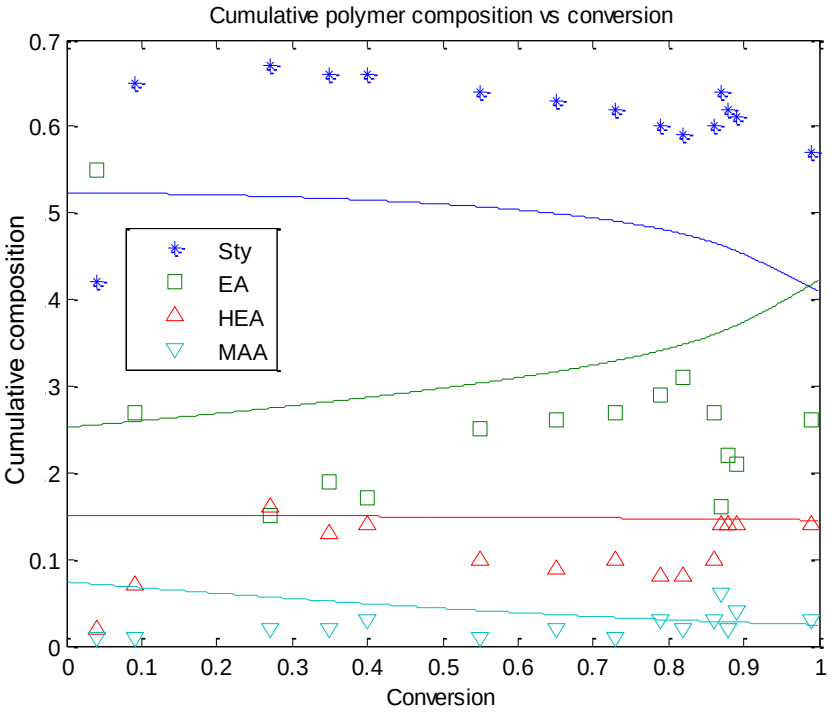

Figure 49. Polymer composition in Sty/EA/HEA/MAA (41/41/16/2 wt%) *tetra*-polymerization T = 100℃, *m*-xylene = 60 wt% of total mixture, octanethiol = 0.5 wt%, and TBPB = 1.5 wt% of total monomer

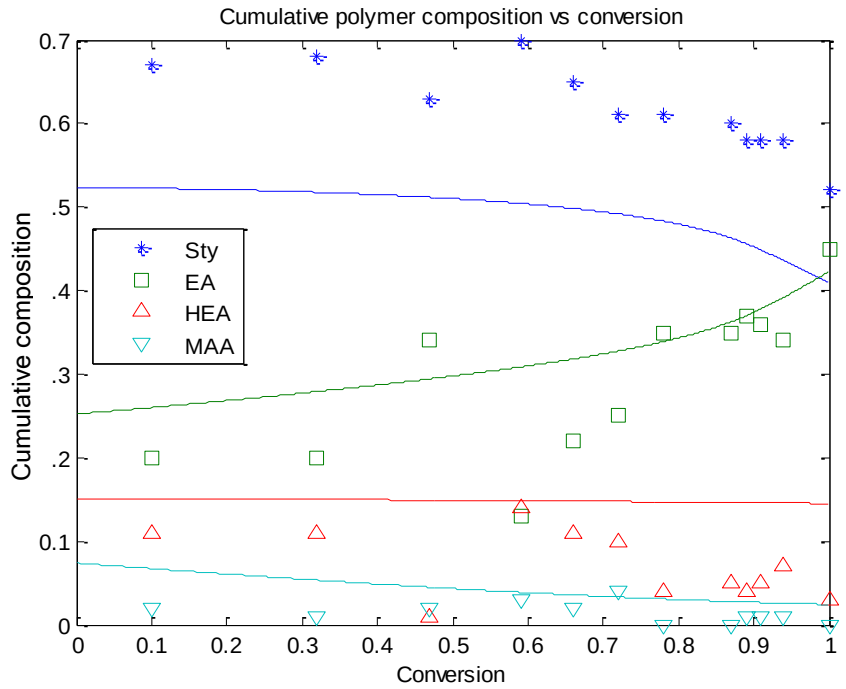

Figure 50. Polymer composition in Sty/EA/HEA/MAA (41/41/16/2 wt%) *tetra*-polymerization
T = 100℃, *m*-xylene = 60 wt% of total mixture
no octanethiol, and TBPB = 1.5 wt% of total monomer

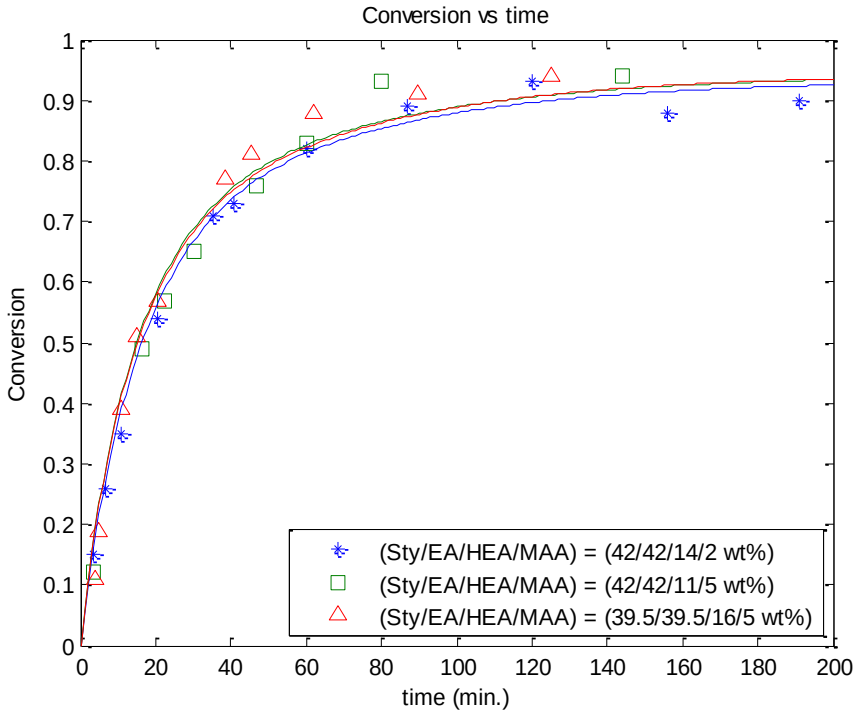

Figure 51. Simulation of solution *tetra*-polymerization of Sty/EA/HEA/MAA
T = 130℃, *m*-xylene = 60 wt% of total mixture
octanethiol = 0.5 wt%, and TBPB = 1.5 wt% of total monomer

3.16 Additional Case Studies/More Complex Model Features

Sequence Length (Triad Fractions) in Sty/BMA/HEMA *Ter*-polymerization

The semi-batch solution *ter*-polymerization of Sty/BMA/HEMA was investigated using the following recipe/conditions: solvent and initiator: pentyl acetate (PAc) and *di-tert*-butyl peroxide (DTBP); monomers: Sty, BMA, and hydroxyethyl methacrylate (HEMA); reaction temperature: 150℃; 50% of the total PAc is charged initially in the reactor. The molar feed flow rates of monomers, solvent, and initiator are presented in Figure 52. Figures 53 and 54 show conversion and solids content vs. time, respectively. Model trends follow the experimental data well. Conversion increased after about 240 minutes because the residual monomers were consumed in this period while the initiator solution feed was maintained. The final predicted solids content in Figure 54 is about 45 %, in agreement with experimental data.

The profiles of residual monomer concentrations are depicted in Figure 55. All the residual monomer concentrations increased from startup to 30-50 minutes, since polymerization was limited due to the small amounts of accumulated initiator and monomers in the semi-batch reactor. As observed in Figure 56, the initial polymer composition of HEMA was higher than BMA, such that Sty > HEMA > BMA, and the HEMA composition remained higher than BMA over the entire conversion. The reason for the higher polymer composition of HEMA than BMA is the greater amount of HEMA monomer in the reactor. The molar inflow rate of HEMA monomer was obviously higher than that of BMA, as shown in Figure 52.

The overall composition drift in Figure 56 was not severe due to the semi-batch operation/recipe. The polymer composition of Sty showed a decreasing trend but the others gradually increased, meaning that Sty was incorporated into the polymer more so than any other monomer at the early stages of polymerization, whereas the other monomers tended to participate more in the reaction later. In addition, the similarly increasing patterns of *ter*-polymer compositions of BMA and HEMA in Figure 56 indicate that the reactivities of these monomers are similar to each other.

In Figures 57 to 59 one can see in detail how the monomers are being incorporated in the polymer chains over conversion. The cumulative number-average sequence length of Sty decreased while the sequence lengths of BMA and HEMA increased in Figure 57, showing the same trends as polymer composition of Figure 56. In the cumulative triad fraction plots of Figures 58 and 59, the Sty-rich fractions such as A_{111}, $A_{112}+A_{211}$, $A_{113}+A_{311}$ (Sty-centered), A_{121} (BMA-centered; not shown for the sake of brevity), and A_{131} (HEMA-centered) decreased, whereas the other fractions increased over conversion. These "hidden" variables (not easily measured) and available via the mathematical model not only corroborate previous trends in *ter*-polymer composition but also offer additional insights, which would be largely non-existent and not so easily apparent without a mathematical model.

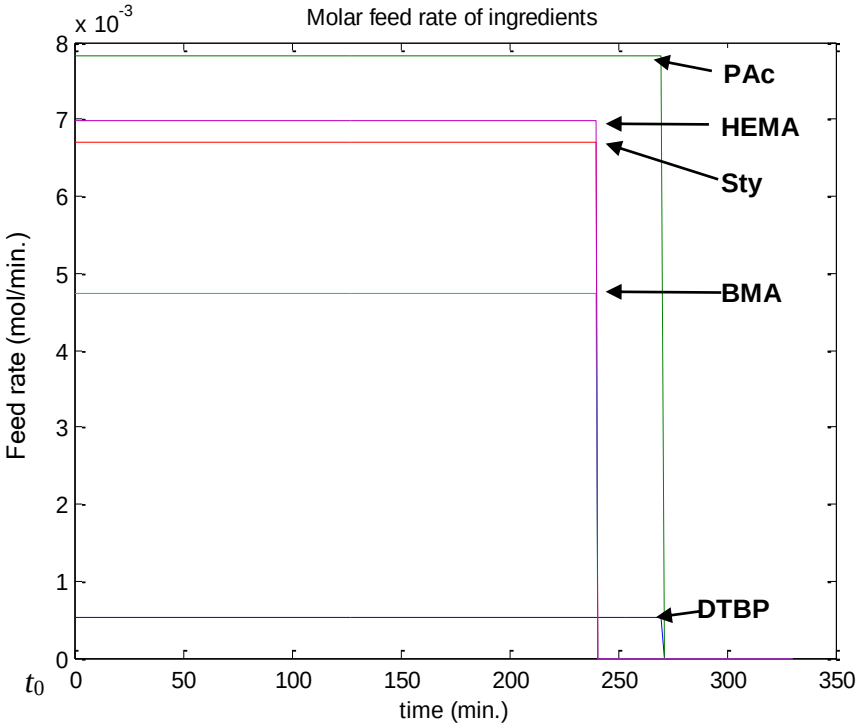

Figure 52. Molar feed rates of monomers, solvent, and initiator

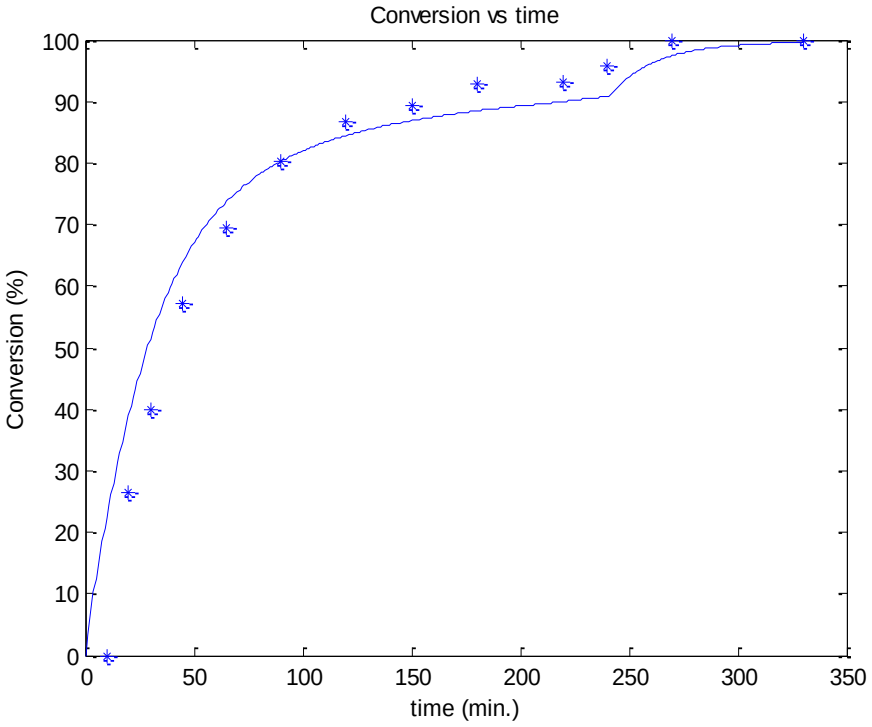

Figure 53. Conversion plot for Sty/BMA/HEMA *ter*-polymerization

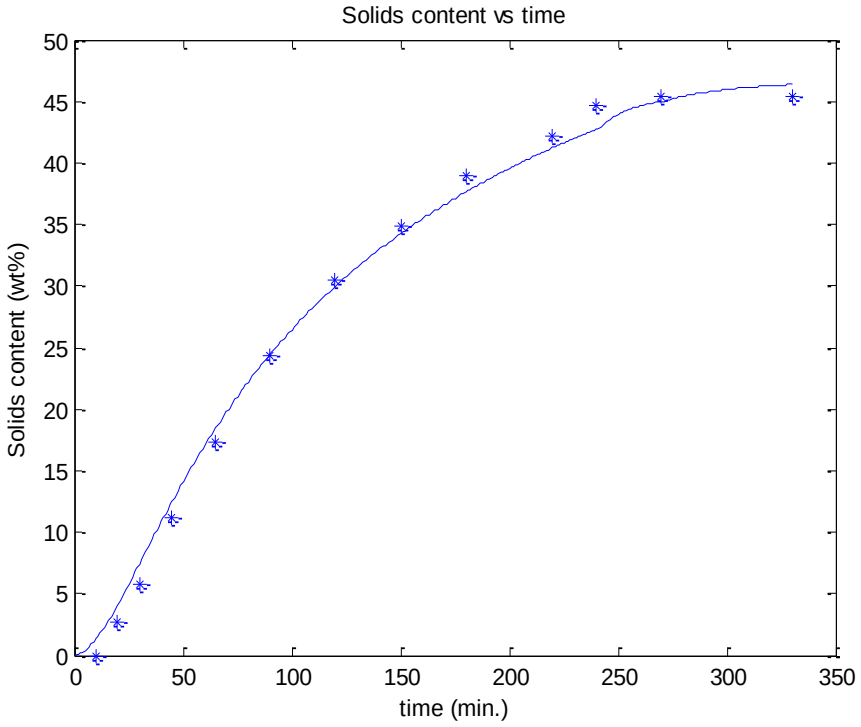

Figure 54. Solids content plot for Sty/BMA/HEMA *ter*-polymerization

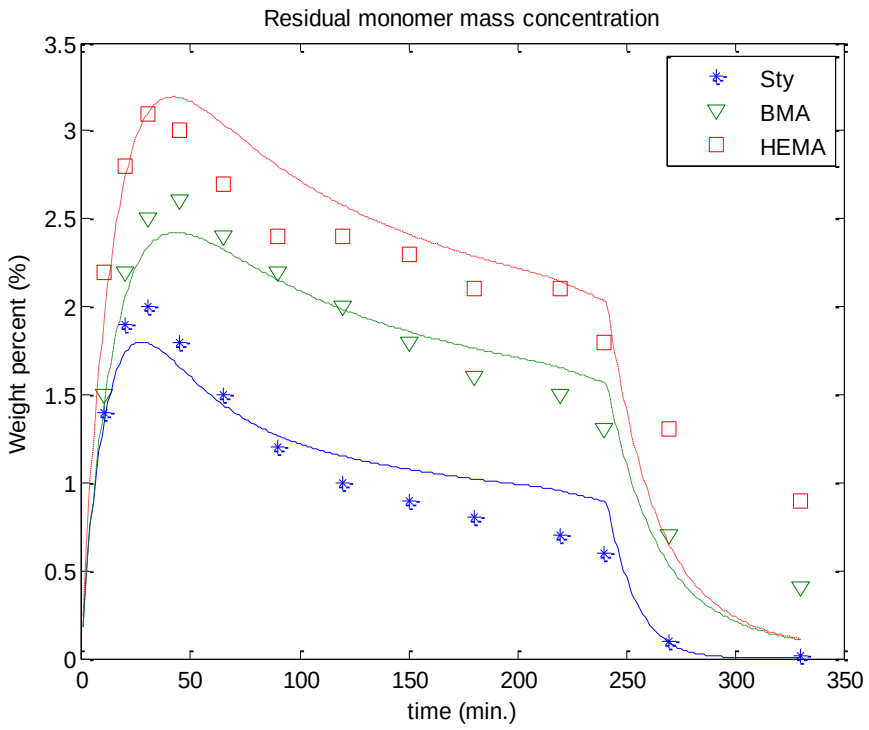

Figure 55. Residual monomer mass concentration plot for Sty/BMA/HEMA *ter*-polymerization

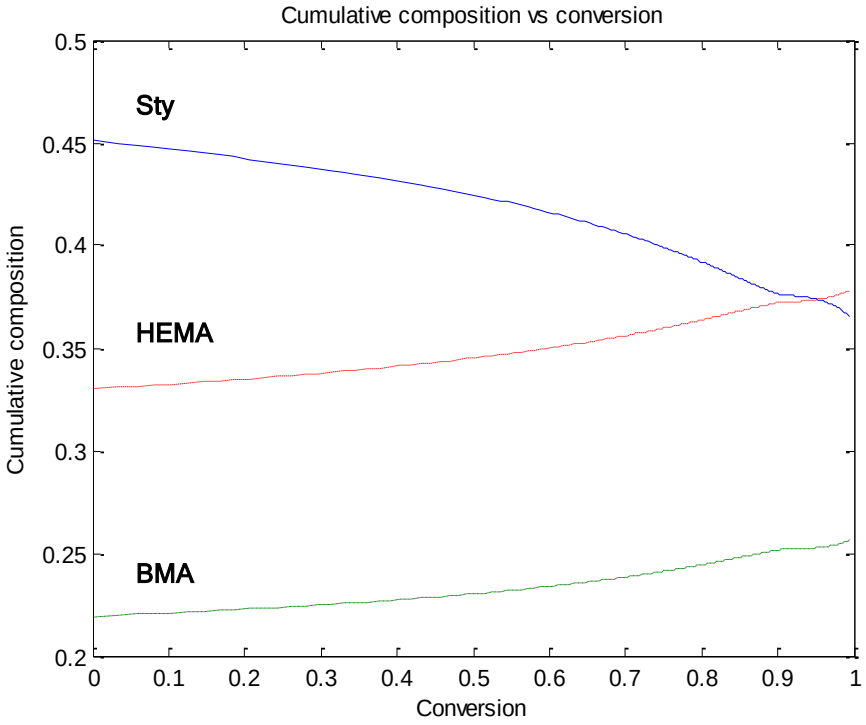

Figure 56. Cumulative polymer composition plot for Sty/BMA/HEMA *ter*-polymerization

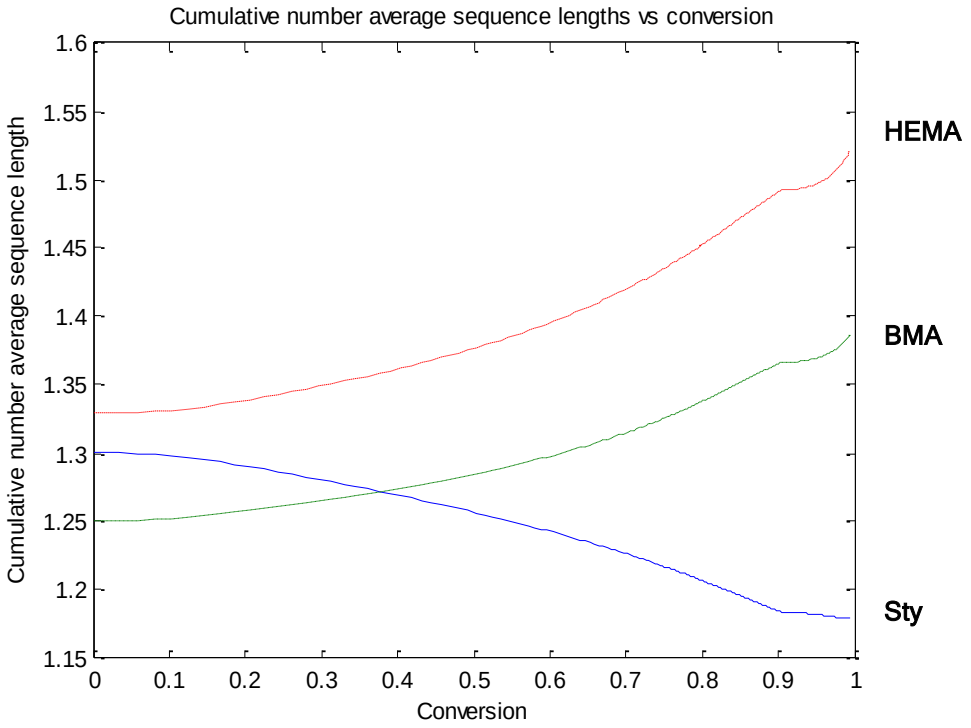

Figure 57. Cumulative number-average sequence lengths for Sty/BMA/HEMA *ter*-polymerization

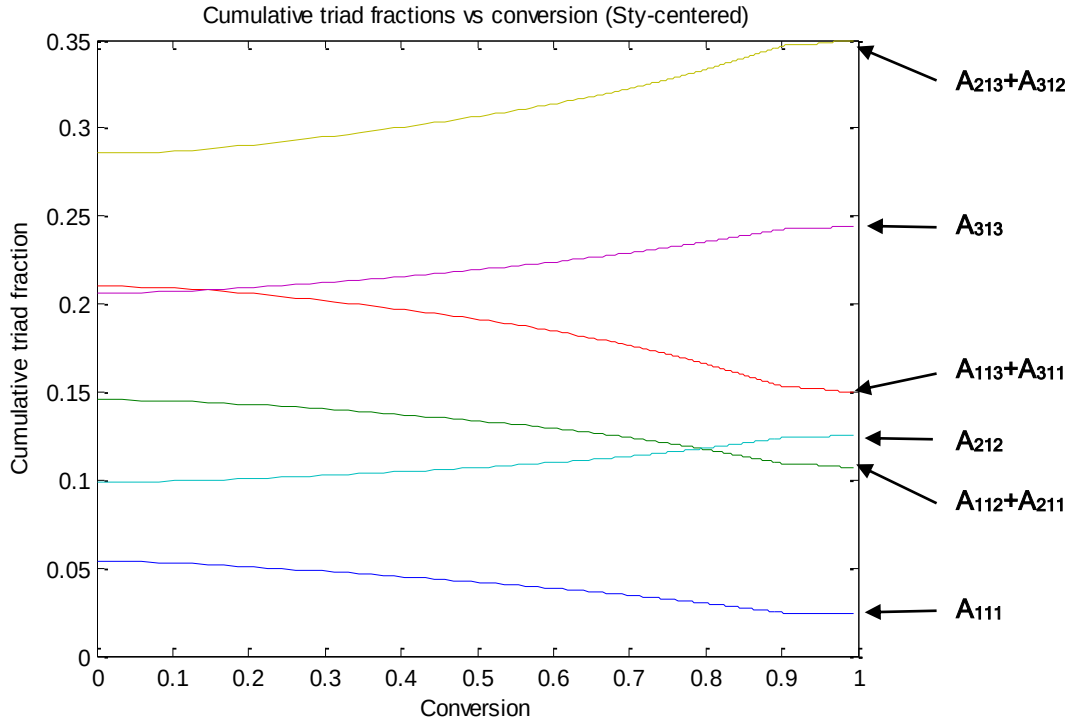

Figure 58. Cumulative (Sty-centered) triad fractions in Sty/BMA/HEMA *ter*-polymerization (1 = Sty, 2 = BMA, 3 = HEMA)

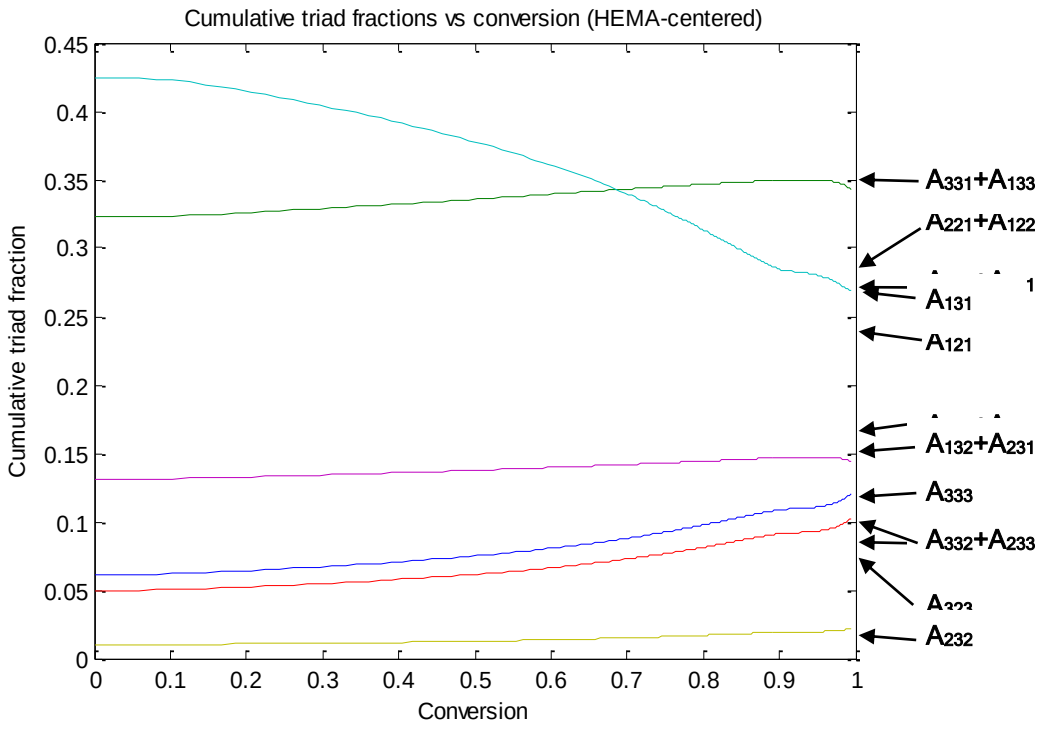

Figure 59. Cumulative (HEMA-centered) triad fractions in Sty/BMA/HEMA *ter*-polymerization (1 = Sty, 2 = BMA, 3 = HEMA)

BMA/BA Semi-batch *Co*-polymerization at Elevated Temperatures

From recent studies on BA solution *homo*-polymerization at elevated temperatures, BA is known to exhibit a more complicated reaction mechanism, which cannot be explained by classical radical polymerization models. It has been found that observed polymerization rates are significantly slower than expected from the chain-end propagation rate coefficient measured by PLP-SEC. This is because intramolecular transfer to polymer (backbiting) generates a tertiary (mid-chain) radical by abstraction of a hydrogen atom from an acrylate unit on its own backbone of the (regular) secondary (chain-end) radical, thus resulting in the formation of a six-membered ring. The more stable tertiary radical propagates with a slower rate. This eventually leads to short chain branching (SCB) formation. Moreover, at elevated reaction temperature levels around 140℃ and above (54), this tertiary radical can also undergo subsequent β-fragmentation (scission) reaction, which lowers the molecular weight averages of the polymer. Following work in (20), (23) and (54), the data from (20) were simulated next, for BMA/BA semi-batch *co*-polymerizations at elevated temperatures, thus testing the model capabilities not only for capturing the high-temperature BA polymerization backbiting features but also the BMA depropagating behaviour. The overall picture obtained, given in Figures 60 to 64, is quite satisfactory for such a complex behaviour. TBPA in the figures stands for *tert*-butyl peroxyacetate initiator.

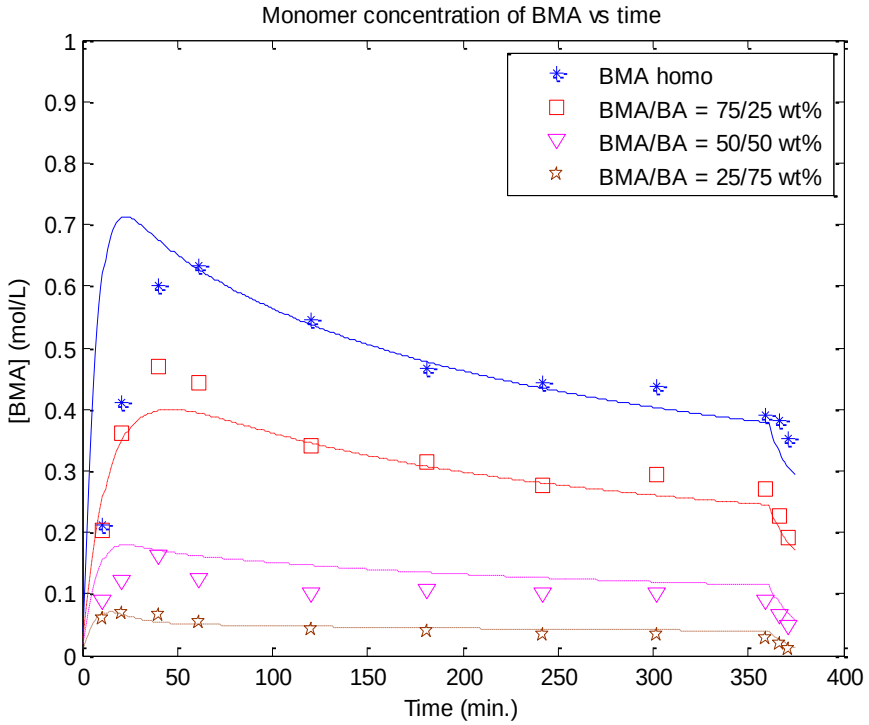

Figure 60. BMA residual monomer concentration in BMA/BA semi-batch solution *co*-polymerization, T = 138℃, TBPA = 1.7 wt% and xylene = 30 wt% of total reaction mixture

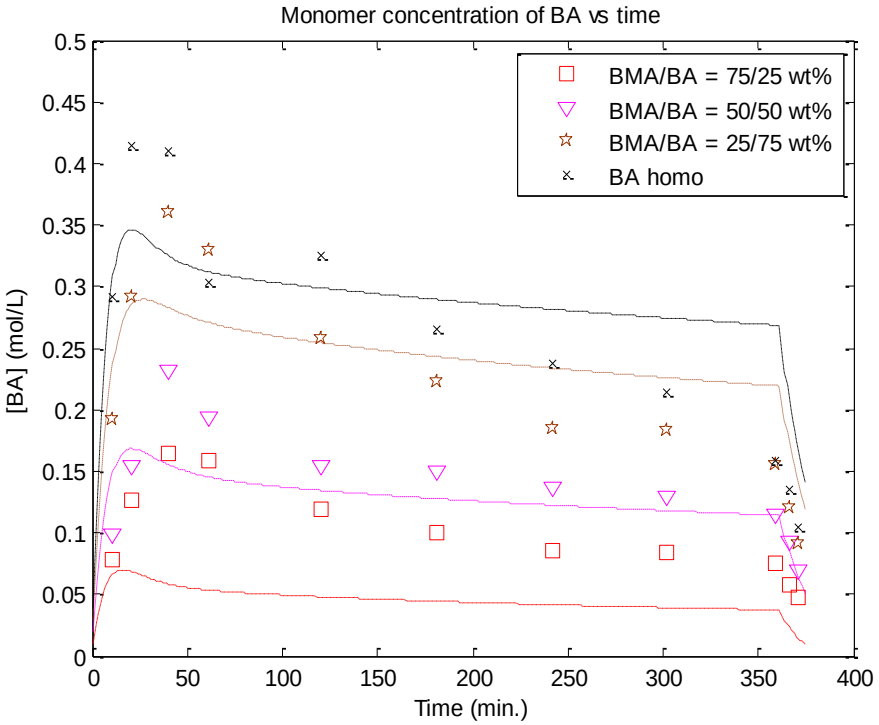

Figure 61. BA residual monomer concentration in BMA/BA semi-batch solution *co*-polymerization, T = 138℃, TBPA = 1.7 wt% and xylene = 30 wt% of total reaction mixture

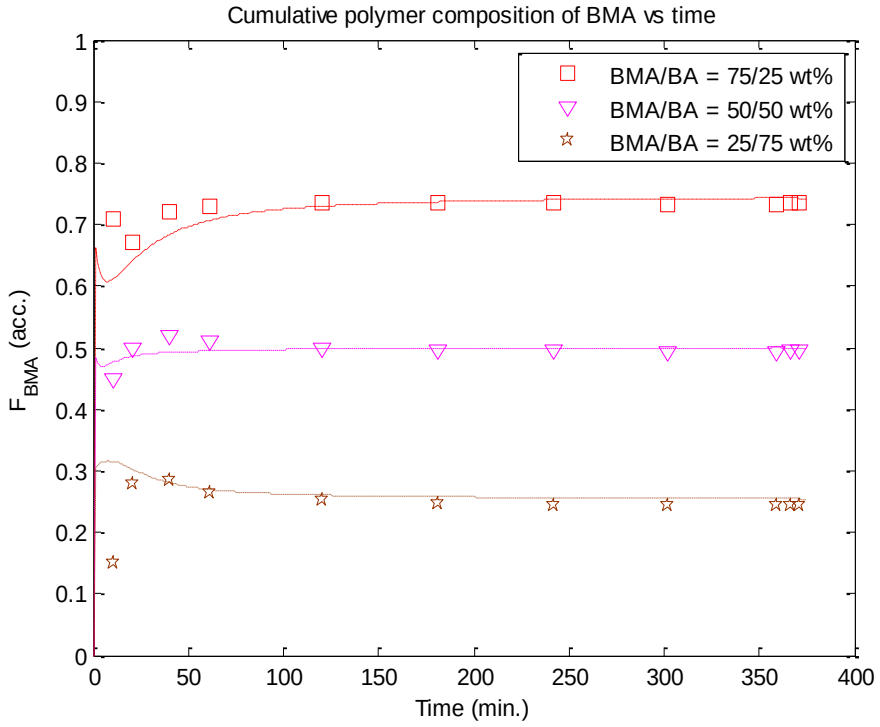

Figure 62. Polymer composition of BMA in BMA/BA semi-batch solution *co*-polymerization T = 138℃, TBPA = 1.7 wt% and xylene = 30 wt% of total reaction mixture

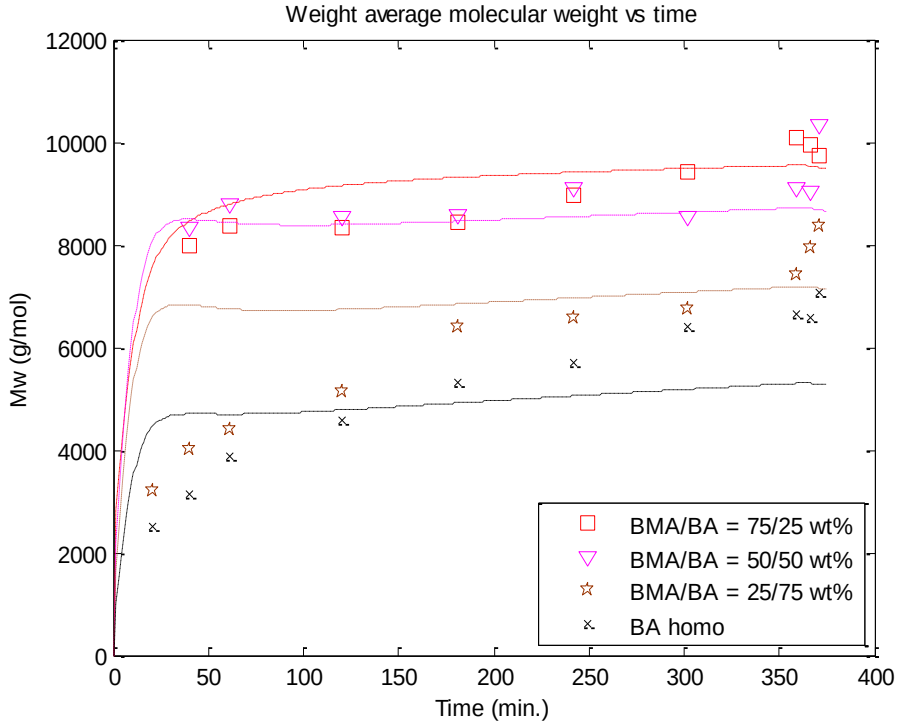

Figure 63. Weight-average molecular weight in BMA/BA semi-batch solution *co*-polymerization, T = 138℃, TBPA = 1.7 wt% and xylene = 30 wt% of total reaction mixture

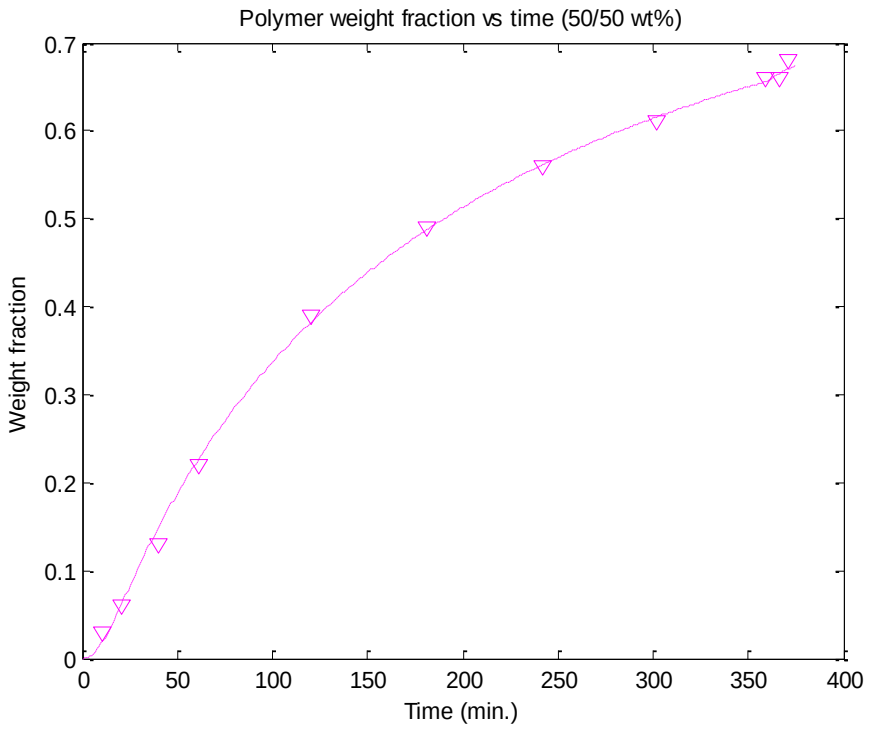

Figure 64. Weight fraction of polymer in solution for BMA/BA = 50/50 wt% T = 138℃, TBPA = 1.7 wt% and xylene = 30 wt% of total reaction mixture

Multi-component Polymer Composition Control

In multi-component polymerization, more than two monomers participate in chain growth. These multi-component polymer products do not have the same composition as the monomer mixture because most monomers have different reactivity ratios. For instance, in batch *co*-polymerization of styrene (Sty) and acrylonitrile (AN), with the exception of the azeotropic case in Figure 65, the initial monomer feed composition (f_{Sty0}) and the corresponding initial polymer composition (F_{Sty0}) are always different. Moreover, the monomer feed composition (f_{Sty}) either increases or decreases as one of the two monomers is preferentially incorporated into the polymer, and the polymer composition (F_{Sty}) also changes accordingly ('composition drift'). The residual mole fraction vs. time trends for Sty/AN *co*-polymerization were shown earlier in Figure 17. The residual mole fraction of Sty in the y-axis of Figure 17 corresponds to f_{Sty}. From Figures 65 and 17, one can see that the azeotropic point ($f_{azeo.}$) of this system exists between 0.5 and 0.6, after which the decreasing trend of residual monomer starts to reverse in Figure 17. This is an important point indicating which monomer is preferentially incorporated into the polymer, determined by reactivity ratios. AN has basically about five times a faster *homo*-propagation rate constant than Sty, and the *cross*-propagation rate of AN radical with Sty monomer is about twenty times more favored than the opposite *cross*-propagation. In this system, Sty monomer is more readily incorporated into polymer than AN monomer when f_{Sty0} is 0.5, a fraction slightly lower than $f_{azeo.}$, and the opposite phenomenon happens at mole fractions higher than $f_{azeo.}$. Therefore, it can be concluded that the *co*-polymer produced at the beginning of the process is richer in the more reactive monomer, while the polymer becomes richer in the less reactive monomer at the end of the batch. This composition drift causes the production of heterogeneous polymer mixtures, which may be deleterious for the performance of the final polymeric material. Most *co*-polymerization systems exhibit composition drift in a batch reactor and more complicated behavior as the number of monomer species increases in the system. Polymer composition is one of the most important factors closely related to the physical/chemical properties of a multi-component polymer. For this reason, the polymer composition should be controlled during the entire reaction if our primary target is producing homogeneous polymer materials.

One of the practical solutions to avoid polymer composition drift is semi-batch polymerization which manipulates monomer feed flow rates. Monomer(s) can be fed to the reactor in a semi-batch (semi-continuous) mode in order to keep monomer composition in the reactor constant (or almost constant) during polymerization. Of course, one can also avoid composition drift with steady-state continuous operation. In the remainder of this subsection, we are going to examine several semi-batch feed policies and implement polymer composition control utilizing our previously developed multi-component polymerization model.

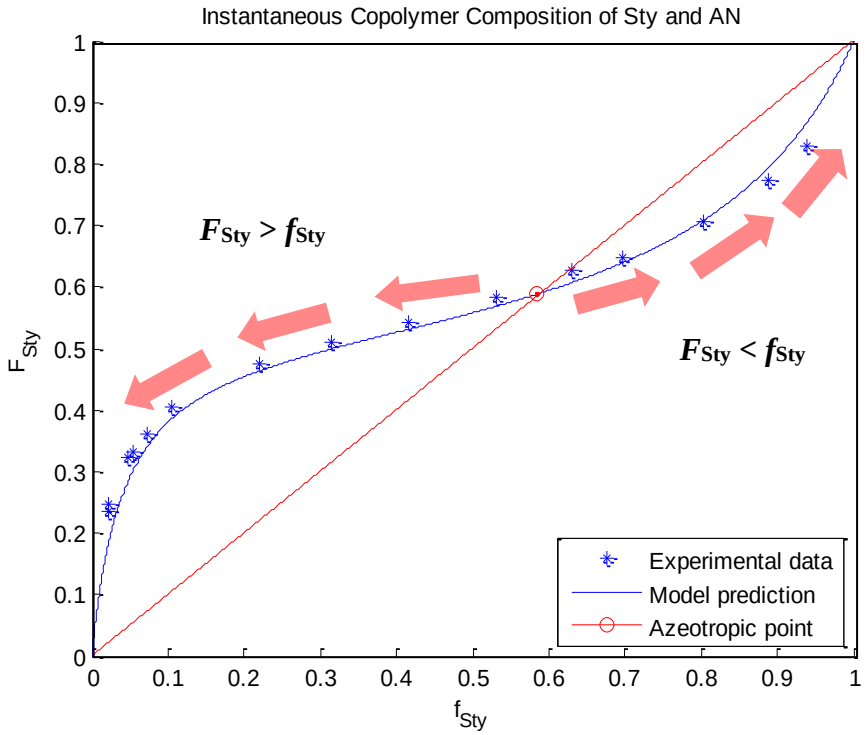

Figure 65. Instantaneous polymer composition vs. monomer feed composition of Sty in Sty/AN bulk *co*-polymerization in a batch reactor at T = 60℃, (r_{Sty}, r_{AN}) = (0.36, 0.078)

Semi-batch feed policies and model development

The extent of composition drift can be mathematically expressed via the polymer composition equation, which is a function of monomer reactivity ratios, monomer feed composition, and conversion. The main idea is to feed fresh monomer(s) via a semi-batch

mode in order to compensate for monomer consumption and hence maintain constant monomer feed composition leading to homogeneous polymer composition during the reaction. In principle, there are many (rather arbitrary, "trial-and-error"-derived) kinds of monomer feed policies possible. Among them, three general, representative policies and their modeling approaches (basic model equations and other details) have been described in Fujisawa and Penlidis (8).

Since the three policies exhibit different monomer concentration profiles from one another in the reactor, their outputs other than polymer composition, such as conversion profile, molecular weight averages, branching/crosslinking levels etc., will differ from policy to policy. In the model testing examples in this subsection, policy 3 has been chosen as an example for polymer composition control due to its popularity and intuitive sense. Another advantage of policy 3 over the other policies is that it is not necessary to choose the faster monomer. The choice of the 'faster monomer' becomes complicated when moving away from binary co-polymerization, as the number of monomers increases in the system.

Following (8), policy 3 can easily be extended to a multi-component polymerization, with the following equations:

$$\frac{dN_1}{dt} = 0\,,\ \frac{dN_2}{dt} = 0\,,\ \frac{dN_3}{dt} = 0\,,\ \frac{dN_4}{dt} = 0\,,\ ... \tag{103}$$

$$F_{1,in} = R_{P1}V\,,\ F_{2,in} = R_{P2}V\,,\ F_{3,in} = R_{P3}V\,,\ F_{4,in} = R_{P4}V\,,\ \ldots \tag{104}$$

In the above equations, N_i denotes moles of monomer i, $F_{i,in}$ molar inflow rate, V is the volume of the polymerizing mixture, and R_{pi} refers to the rate of consumption (polymerization) for monomer i. A *co*-polymer composition control routine with policy 3 can be implemented utilizing our previously developed batch and semi-batch polymerization models (see Figure 66).

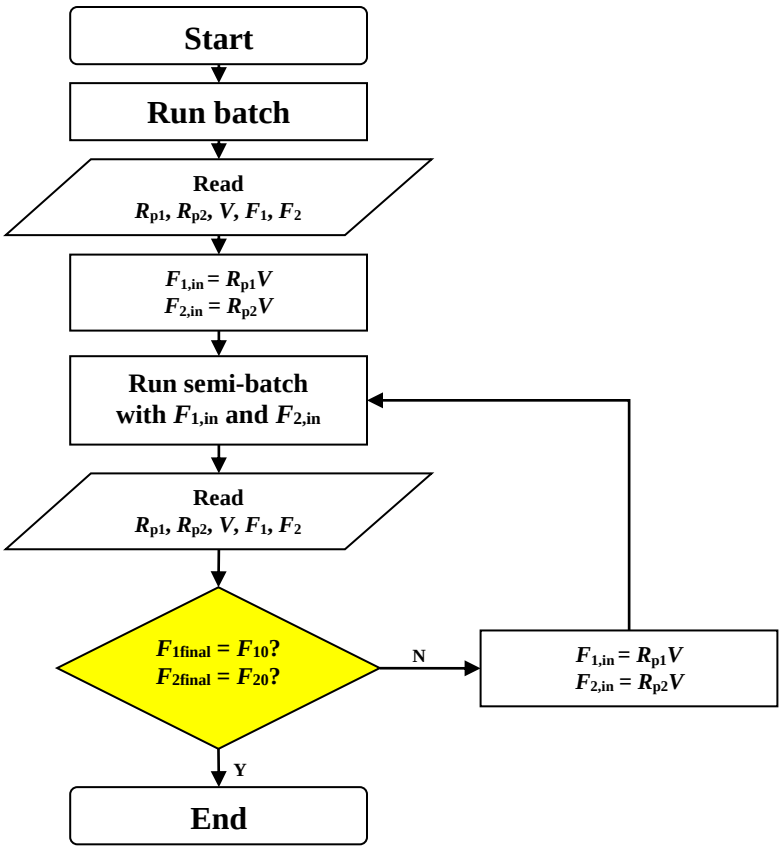

Figure 66. Flowchart of *co*-polymer composition control (based on policy 3)

As mentioned earlier, polymer composition control policy 3 has been chosen as an example and implemented in Sty/BA bulk *co*-polymerization (Figures 67 and 68) and extended to Sty/BA/BMA *ter*-polymerization (Figures 69 and 70) at regular temperature levels. Figure 67 shows the sequence of iterations needed over molar inflow rates of fresh monomer feeds to yield constant *co*-polymer composition (desirable targets are F_{Sty} = F_{Sty0} = 0.466 and F_{BA} = F_{BA0} = 0.534). The corresponding *co*-polymer composition trends (per iteration) are depicted in Figure 69. After the batch simulation where F_{Sty} at final conversion ($F_{Sty(final)}$) drops (drifts) down to 0.263, the first feeds to compensate for monomer consumption are determined based on policy 3 (see Figure 66), and these flow rates are used in the semi-batch model. As a result of the first monomer feeds (iteration), reduced polymer composition drift is obtained (compare the trends of Sty/BA 1st in Figure 68 with "Sty batch"). However, $F_{Sty(final)}$ from the first iteration is 0.312 and still indicates deviation from the desirable F_{Sty0}, which means that monomer consumption is greater than the compensating feed and hence, composition drift is still in effect.

In order to reduce further and/or eliminate the remaining composition drift, the second (iteration) monomer feeds are calculated again to fill the gap from the first semi-batch simulation, and the resulting composition trends are quite satisfactory (see Sty/BA 2nd in Figures 67 and 68), since $F_{Sty(final)}$ from the second iteration is 0.427 and this is much closer to the desirable F_{Sty0} target than the one (0.312) from the first iteration. This "control routine" is conducted repeatedly until the difference between F_{Sty0} and $F_{Sty(final)}$ lies within a certain tolerance limit (note that diffusion control may influence the rate of polymerization (consumption) of each monomer at every iteration and therefore, feed compensation should be corrected accordingly). As the third, fourth, and possibly further monomer feeds are calculated, it is observed that $|F_{Sty0} - F_{Sty(final)}|$ becomes smaller and the polymer composition remains constant at the target value during the whole polymerization (at the fourth iteration in our example).

The *co*-polymer composition control policy 3 has been extended to Sty/BA/BMA *ter*-polymerization using Equations 103 and 104. In Figure 69, molar feed rates of Sty, BA, and BMA monomers are plotted for *ter*-polymer composition control to maintain $F_{Sty} = F_{Sty0} = 0.373$, $F_{BA} = F_{BA0} = 0.326$, and $F_{BMA} = F_{BMA0} = 0.301$ over the entire polymerization. The corresponding polymer composition trends are shown in Figure 70. In four iterations again, each polymer composition approaches its own target value and the results of policy 3 in *ter*-polymerization are quite satisfactory as well. Batch *ter*-polymerization results are also shown in Figure 70 for comparison purposes.

As mentioned above, it is very important to notice that the three policies (based on (8)) used for *co*- or multi-component polymer composition control produce different monomer concentrations in the reactor and hence they may have significantly different impacts on conversion, molecular weight averages, and branching/crosslinking levels of the polymeric material. Therefore, it is eventually required to choose the "optimal" policy which meets desired product specifications in addition to polymer composition. Furthermore, it is advisable to combine monomer semi-batch feed policies with other ingredients (initiator/solvent/CTA) semi-batch feed strategies or with non-isothermal

policies (temperature programming). Of course, it is also possible to consider these combinations for controlling both polymer composition and other product quality factors simultaneously. A general multi-component polymerization model can handle these features and can give a reliable solution to these combined optimization/control strategies as well.

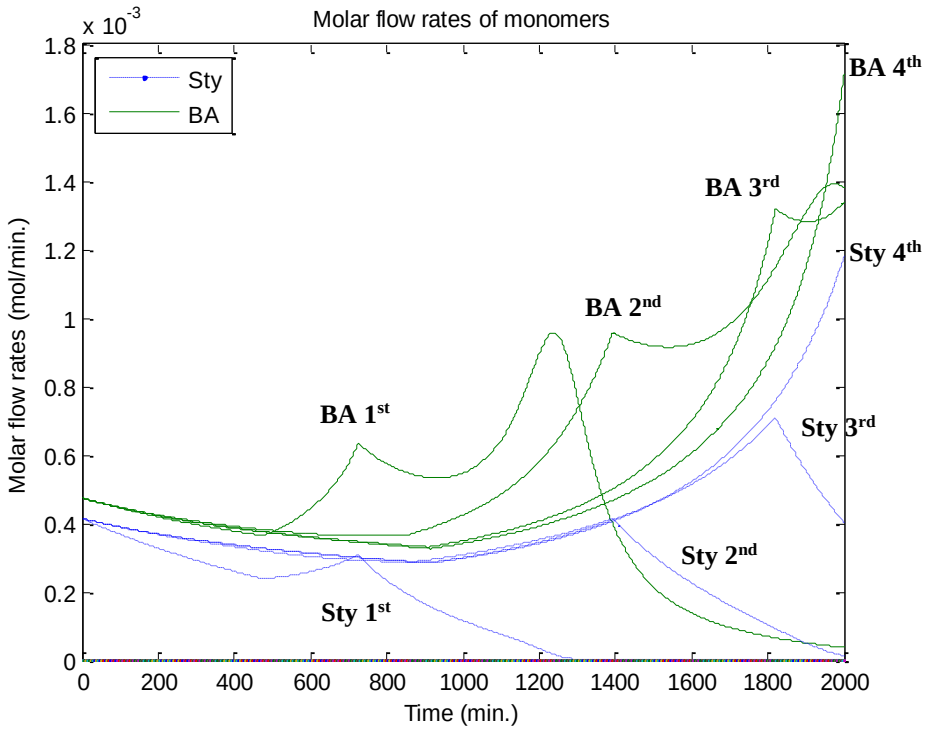

Figure 67. Iteration of molar flow rates of monomers in Sty/BA semi-batch bulk *co*-polymerization to maintain constant polymer composition (F_{Sty0} = 0.466) over the entire polymerization, T = 50℃, f_{Sty0} = 0.258, and $[AIBN]_0$ = 0.05 M

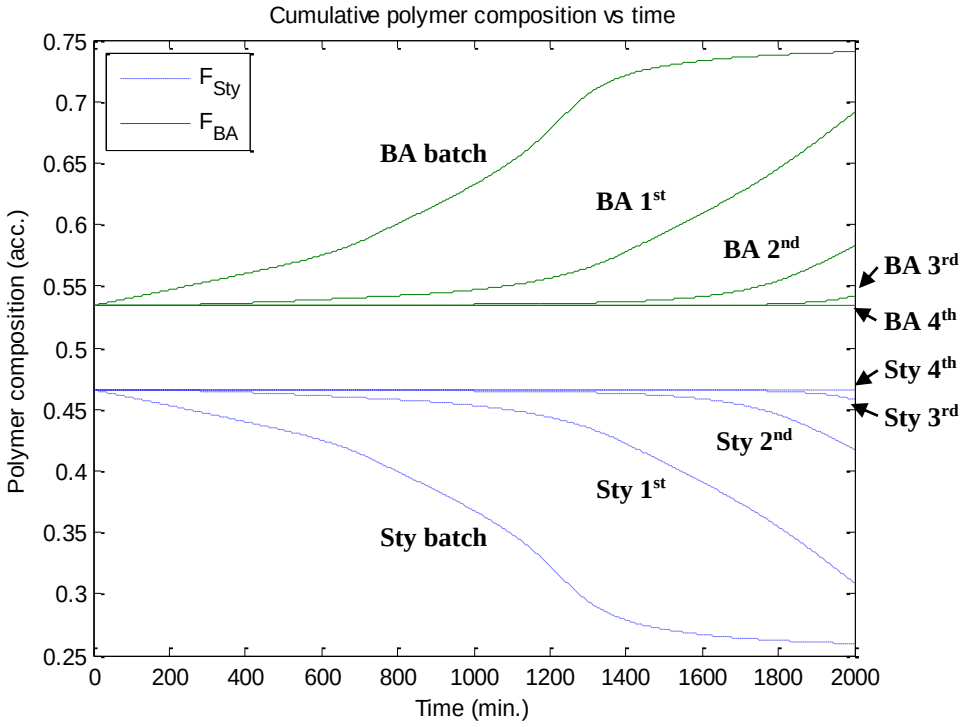

Figure 68. Cumulative polymer composition changes in Sty/BA semi-batch bulk *co*-polymerization corresponding to monomer feed policies in Figure 67 for polymer composition control, T = 50℃, f_{Sty0} = 0.258, and $[AIBN]_0$ = 0.05 M

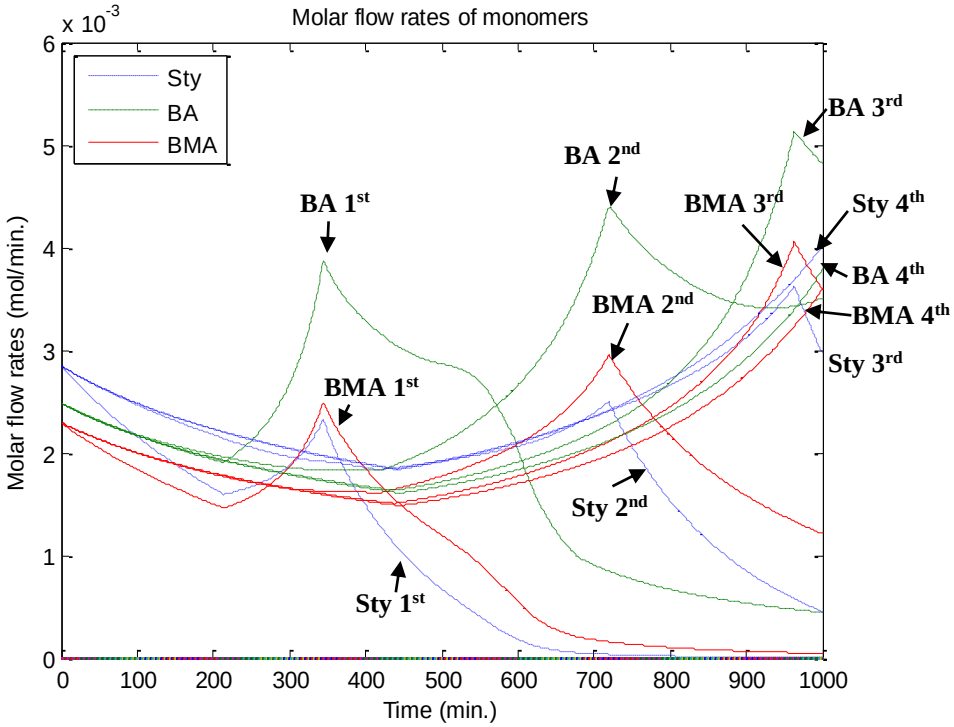

Figure 69. Iteration of monomer flow rates in Sty/BA/BMA semi-batch bulk *ter*-polymerization to maintain constant polymer composition (F_{Sty0} = 0.373, F_{BA0} = 0.326) over the entire polymerization, T = 60℃, f_{Sty0} = 0.22, f_{BA0} = 0.54, and $[AIBN]_0$ = 0.02 M

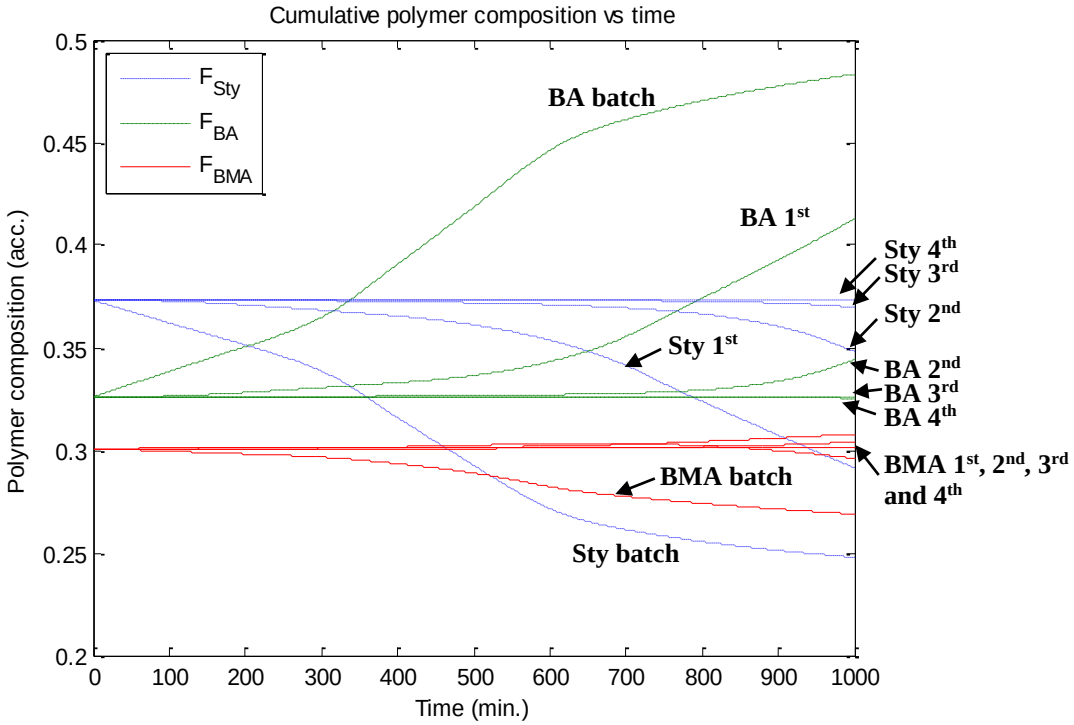

Figure 70. Cumulative polymer composition changes in Sty/BA/BMA semi-batch bulk *ter*-polymerization corresponding to monomer feed policies in Figure 69 for polymer composition control, T = 60℃, f_{Sty0} = 0.22, f_{BA0} = 0.54, and $[AIBN]_0$ = 0.02 M

4 Conclusions

A general, flexible multi-component free-radical polymerization model has been tested over a wide range of recipes and operating conditions in order to check its reliability. Due to the increasing complexity when the number of monomers in the system becomes larger than two or three, literature sources on multi-component cases of more than three monomers are very limited. Notwithstanding this, our model has shown good prediction results wherever possible and proved to be useful for better understanding of the complicated multi-component polymerization process. Developing a multi-component polymerization model is challenging and requires a constant effort and update of model features, representing essentially a long-term multidisciplinary commitment, including properly designed experimental studies (for rigorous parameter estimation), model development, continuous testing with troubleshooting scenarios, and optimization applications with verifications. It is certain that this flexible simulator package described and tested herein (in part 1 of this series) is another milestone in the right direction and, therefore, it will be a helpful tool for industrial, academic, and educational purposes. Part 2 of the series will describe more complicated situations with depropagation and composition control policies, all relying solely on a unique monomer/polymer database of physico-chemical properties and other characteristics, with no further parameter adjustment. These database items will also be cited in tables in part 2 of the series.

Acknowledgements

The authors wish to acknowledge financial support from the Natural Sciences and Engineering Research Council (NSERC) of Canada, and the Canada Research Chair (CRC) program. Also, many thanks go to BASF, Germany, and especially Dr. Klaus-Dieter Hungenberg for lively discussions.

References

1. M. E. Kuindersma, **On the modeling of free-radical polymerization reactions: *Homo*-polymerization**, *MASc thesis, Department of Chemical Engineering, Univ. of Waterloo* (1992)
2. J. Gao, A. Penlidis, **A comprehensive simulator/database package for reviewing free-radical *homo*-polymerizations**, *Journal of Macromolecular Sciences - Revs. Macromolecular Chemistry and Physics*, **C36(2)**, 199-404 (1996)
3. J. Gao, A. Penlidis, **A comprehensive simulator/database package for bulk/solution free-radical *co*-polymerizations**, *Journal of Macromolecular Sciences - Revs. Macromolecular Chemistry and Physics*, **C38(4)**, 651-780 (1998)
4. J. Gao, A. Penlidis, **A comprehensive simulator/database package for bulk/solution free-radical *ter*-polymerizations**, *Macromolecular Chemistry Physics*, **201**, 1176-1184 (2000)
5. W. Jung, **Mathematical modeling of free-radical six-component bulk and solution polymerization**, *MASc thesis, Department of Chemical Engineering, Univ. of Waterloo* (2008)
6. R. Dhib, J. Gao, A. Penlidis, **Simulation of free-radical bulk/solution *homo*-polymerization using mono- and bi-functional initiators**, *Polymer Reaction Engineering J.*, **8(4)**, 299-464 (2000)
7. J. Gao, K. D. Hungenberg, A. Penlidis, **Process modeling and optimization of styrene polymerization**, *Macromolecular Symposia*, **206**, 509-522 (2004)
8. T. Fujisawa, A. Penlidis, ***Co*-polymer composition control policies: Characteristics and Applications**, *Journal of Macromolecular Science, Part A: Pure and Applied Chemistry*, **45**, 115-132 (2008)
9. H. W. McCormick, **Ceiling temperature of alpha-methyl styrene**, *Journal of Polymer Science*, **25(111)**, 488-490 (1957)
10. G. G. Lowry, **The effect of depropagation on *co*-polymer composition, I. General theory for one depropagating monomer**, *Journal of Polymer Science*, **42**, 463-477 (1960)

11. P. Wittmer, ***Co*-polymerization in the presence of depolymerization reactions**, *Advances in Chemistry Series*, **99**, 140-174 (1971)
12. F. R. Mayo, F. M. Lewis, **A basis for comparing the behaviour of monomers in *co*-polymerization; The *co*-polymerization of styrene and methyl methacrylate**, *Journal of American Chemical Society*, **66**, 1594-1601 (1944)
13. H. Krüger, J. Bauer, J. Rübner, **Ein Modell zur Beschreibung reversibler *Co*-polymerisationen**, *Makromolekulare Chemie*, **188**, 2163-2175 (1987)
14. D. E. Palmer, N. T. McManus, A. Penlidis, ***Co*-polymerization with depropagation: A study of AMS/MMA in bulk at elevated temperatures**, *Journal of Polymer Science: Part A: Polymer Chemistry*, **38**, 1981-1990 (2000)
15. D. E. Palmer, N. T. McManus, A. Penlidis, ***Co*-polymerization with depropagation: A study of AMS/MMA in solution at elevated temperatures**, *Journal of Polymer Science: Part A: Polymer Chemistry*, **39**, 1753-1763 (2001)
16. S. I. Cheong, A. Penlidis, **Modeling of the *co*-polymerization, with depropagation, of AMS/MMA at an elevated temperature**, *Journal of Applied Polymer Science*, **93**, 261-270 (2004)
17. M. J. Leamen, N. T. McManus, A. Penlidis, **Binary *co*-polymerization with full depropagation: A study of MMA/AMS *co*-polymerization**, *Journal of Polymer Science: Part A: Polymer Chemistry*, **43**, 3868-3877 (2005)
18. M. J. Leamen, N. T. McManus, A. Penlidis, ***Ter*-polymerization with depropagation: Modeling the *co*-polymer composition of the MMA/AMS/BA system**, *Chemical Engineering Science*, **61**, 7774-7785 (2006)
19. M. C. Grady, W. J. Simonsick Jr., R. A. Hutchinson, **Studies of higher temperature polymerization of BMA and BA**, *Macromolecular Symposia*, **182**, 149-168 (2002)
20. D. Li, M. C. Grady, R. A. Hutchinson, **High-temperature semi-batch free radical *co*-polymerization of BMA and BA**, *Industrial & Engineering Chemistry Research*, **44**, 2506-2517 (2005)
21. D. Li, N. Li, R. A. Hutchinson, **High temperature free-radical *co*-polymerization of styrene and BMA with depropagation and penultimate kinetic effects**, *Macromolecules*, **39**, 4366-4373 (2006)

22. W. Wang, R. A. Hutchinson, **High temperature semi-batch free-radical *co*-polymerization of styrene/DMA**, *Macromolecular Symposia*, **261**, 64-73 (2008)
23. F. S. Rantow, M. Soroush, M. C. Grady, G. A. Kalfas, **Spontaneous polymerization and chain microstructure evolution in high-temperature solution polymerization of *n*-butyl acrylate**, *Polymer*, 47, 1423-1435 (2006)
24. A. W. Hui, A. E. Hamielec, **Thermal polymerization of styrene at high conversions and temperatures: An experimental study**, *Journal of Applied Polymer Science*, **16**, 749-769 (1972)
25. T. Alfrey, G. Goldfinger, ***Co*-polymerization of systems containing three components**, *Journal of Chemical Physics*, **14**, 115-116 (1946)
26. C. Walling, E. R. Briggs, ***Co*-polymerization. III Systems containing more than two monomers**, *Journal of the American Chemical Society*, **67**, 1774-1778 (1945)
27. A. Valvassori, G. Sartori, **Present status of multi-component *co*-polymerization theory**, *Advances in Polymer Science*, **5(1)**, 28-58 (1967)
28. M. B. Hocking, K. A. Klimchuk, **A refinement of the *ter*-polymer equation and its simple extension to two- and four-component systems**, *Journal of Polymer Science: Part A: Polymer Chemistry*, **34**, 2481-2497 (1996)
29. J. L. Koenig, **Chemical Microstructure of Polymer Chains, Chap. 3**, *John Wiley & Sons* (1980)
30. H. Ray, R. Laurence, **Chemical Reactor Theory; A review, Chap. 9**, *Prentice-Hall* (1977)
31. A. E. Hamielec, J. F. MacGregor, A. Penlidis, **Comprehensive Polymer Science Encyclopedia, Chap. 2**, *Pergamon Press*, **3**, 17-31 (1987)
32. A. E. Hamielec, J. F. MacGregor, A. Penlidis, **Multi-component free-radical polymerization in batch, semi-batch and continuous reactors - modelling and control of chain composition, microstructure, molecular weight distribution, long chain branching and crosslinking in solution and emulsion polymerization**, *Makromolekulare Chemie, Macromolecular Symposia*, **10-11**, 521-570 (1987)
33. T. Y. Xie, A. E. Hamielec, **Modeling free-radical *co*-polymerization kinetics – evaluation of the pseudo-kinetic rate constant method, 2 Molecular weight**

calculations for *co*-polymers with long chain branching, *Makromolekulare Chemie, Theory and Simulations*, **2(3)**, 455-483 (1993)

34. F. L. Marten, A. E. Hamielec, **High-conversion diffusion-controlled polymerization of Sty I**, *Journal of Applied Polymer Science*, **27**, 489-505 (1982)
35. M. Stickler, D. Panke, A. E. Hamielec, **Polymerization of MMA up to high degrees of conversion: Experimental investigation of the diffusion-controlled polymerization**, *Journal of Polymer Science: Polymer Chemistry Edition*, **22**, 2243-2253 (1984)
36. M. Stickler, **Free-radical polymerization kinetics of MMA at very high conversions**, *Makromolekulare Chemie*, **184**, 2563-2579 (1983)
37. K. Arai, S. Saito, **Simulation model for the rate of bulk polymerization over the complete course of reaction**, *Journal of Chemical Engineering of Japan*, **9(4)**, 302-313 (1976)
38. V. R. Kumar, S. K. Gupta, **Optimal parameter estimation for MMA polymerization**, *Polymer*, **32(17)**, 3233-3243 (1991)
39. J. D. Kim, **A kinetic study of Sty/HEA *co*-polymerization**, *MASc thesis, Department of Chemical Engineering, Univ. of Waterloo* (1994)
40. E. Vargün, A. Usanmaz, **Polymerization of HEA in bulk and solution by chemical initiator and by ATRP method**, *Journal of Polymer Science: Part A: Polymer Chemistry*, **43**, 3957-3965 (2005)
41. M.A. Dubé + AP 1991 (BA paper)
42. A. S. Nair, M. S. Muthana, **Studies on the polymerization of methacrylic esters Part I. Polymerization of *n*-BMA and *iso*-BMA**, *Makromolekulare Chemie*, **47**, 114-127 (1961)
43. M. A. Dubé, A. Penlidis, **A systematic approach to the study of multi-component polymerization kinetics: BA/MMA/VAc example, 1. Bulk *co*-polymerization**, *Polymer*, **36(3)**, 587-598 (1995)
44. A. M. Alb, P. Enohnyaket, M. F. Drenski, A. Head, A. W. Reed, W. F. Reed, **Online monitoring of *co*-polymerization involving *co*-monomers of similar spectral characteristics**, *Macromolecules*, **39**, 5705-5713 (2006)

45. V. E. Meyer, G. G. Lowry, **Integral and differential binary *co*-polymerization equations**, *Journal of Polymer Science: Part A: General Papers*, **3(8)**, 2843-2851 (1965)
46. L. H. Garcia-Rubio, M. G. Lord, J. F. MacGregor, A. E. Hamielec, **Bulk *co*-polymerization of Sty and AN: Experimental kinetics and mathematical modeling**, *Polymer*, **26**, 2001-2013 (1985)
47. N. T. McManus, J. D. Kim, A. Penlidis, **Observations on Sty/HEA and Sty/HEA/EA polymerizations**, *Polymer Bulletin*, 41, 661-668 (1998)
48. M. A. Dubé, A. Penlidis, K. F. O'Driscoll, **Mathematical modelling of Sty/BA *co*-polymerization**, *Chemical Engineering Science*, **45(8)**, 2785-2792 (1990)
49. S. Bywater, **Photosensitized polymerization of MMA in dilute solution above 100℃**, *Transactions of the Faraday Society*, **51**, 1267-1273 (1955)
50. F. Martinet, J. Guillot, ***Co*-polymerization with depropagation: Prediction of kinetics and properties of AMS-MMA *co*-polymers. II. Bulk *co*-polymerization**, *Journal of Applied Polymer Science*, **72**, 1611-1625 (1999)
51. M. A. Dubé, A. Penlidis, **A systematic approach to the study of multi-component polymerization kinetics: BA/MMA/VAc example, 2. Bulk (and solution) *ter*-polymerization**, *Macromolecular Chemistry and Physics*, **196**, 1102-1112 (1995)
52. N. A. Sahloul, **A Study of multi-component polymerization of Sty/EA/HEA/MAA**, *PhD thesis, Department of Chemical Engineering, University of Waterloo* (2004)
53. N. T. McManus, G. Hsieh, A. Penlidis, **Free-radical *ter*-polymerization of BA/MMA/AMS at high temperature**, *Polymer*, **45**, 5837-5845 (2004)
54. A. N. F. Peck, R. A. Hutchinson, **Secondary reactions in the high-temperature free radical polymerization of BA**, *Macromolecules*, **37**, 5944-5951 (2004)